MSc Thesis

Advancements in VIC-TSA with Radial Basis Functions

Student:
Martino Pinto (5613795)

Supervisors:
Prof. Fulvio Scarano
Dr. Lourenço Tercio Lima Pereira

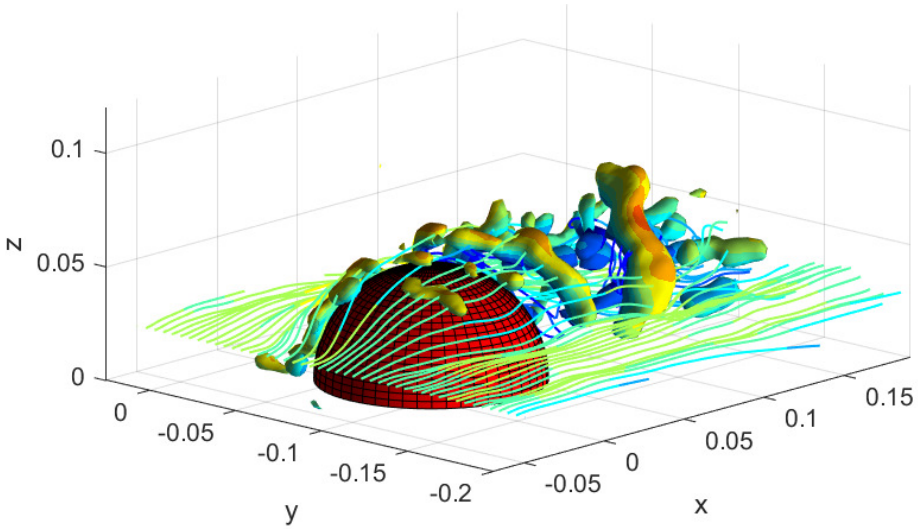

TU Delft
February 16, 2024

Abstract

Particle Tracking Velocimetry (PTV) is an effective and non-intrusive flow measurement technique that is able to provide quantitative information of the full velocity field at a certain instant in time, by tracking each particle individually with high-speed cameras. This permits to have a very high precision in measuring the flow evolutions. The abundant time information can then be leveraged by reconstruction algorithms not only to bring the information into a Cartesian format, but also to increase the space resolution of the original measurements. This thesis aims to explore the enhancement of the Navier-Stokes based reconstruction method called VIC-TSA (Vortex-in-Cell with Time-Segment-Assimilation) through the implementation of Radial Basis Functions (RBF). Moreover, it investigates whether the incorporation of RBFs can enable VIC TSA to match or exceed the accuracy of the VIC+ method. The improvements are evaluated numerically with a synthetic flow field (Taylor-Green sine wave vortex lattice) and experimentally (flow over a bluff body) with a real Lagrangian Particle Tracking (LPT) experiment in the TU Delft W-Tunnel.

Contents

List of Figures **vi**

List of Tables **vii**

Acronyms **vii**

1 Introduction **1**
1.1 Background 1
1.2 Problem statement 1
1.3 Research objectives 2
1.4 Structure of the thesis 3
1.5 Overview of PIV and PTV 4
1.5.1 Particle Image Velocimetry (PIV) 4
1.5.2 Particle Tracking Velocimetry (PTV) 5

2 Data assimilation techniques **6**
2.1 Introduction 6
2.2 Time-super sampling 7
2.3 Space super-resolution 9
2.4 Other types of reconstruction methods 13
2.5 Lagrangian particle tracking 15
2.6 Challenges of PIV 16
2.7 Conclusions and research questions 19

3 The VIC-TSA framework **21**
3.1 Working principle 22
3.2 The algorithm 23
3.3 Adjoint method for gradient evaluation 27
3.3.1 Mathematical formulation of the optimization problem 27
3.3.2 Calculation of the gradient 28
3.3.3 Adjoint equations for VIC-TSA 29

4 Radial Basis Functions **32**
4.1 Implementation in VIC-TSA . . . 32
4.2 Gaussian Radial Basis Functions . . . 33
4.2.1 Computing derivatives . . . 35
4.3 From RBF coefficients to vorticity values . . . 35
4.3.1 Test case description . . . 37
4.4 RBF evaluation with FFT . . . 39
4.5 Modification to the adjoint procedure . . . 41

5 Numerical Assessment **43**
5.1 Assessment of reconstruction methods . . . 43
5.1.1 Taylor-Green vortex lattice . . . 44
5.1.2 Tracer tracking . . . 46
5.1.3 Metrics and comparisons . . . 50
5.2 Results . . . 53
5.2.1 Amplitude modulation . . . 53
5.2.2 On the importance of t^* and track regimes . . . 56
5.3 Robustness and convergence . . . 59
5.3.1 Mesh convergence for interpolations . . . 60
5.3.2 Robustness (noise over Taylor-Green) . . . 63

6 Experimental assessment **68**
6.1 Experiment description . . . 68
6.1.1 Objective . . . 68
6.1.2 Experimental setup for flow over hemisphere . . . 69
6.1.3 Data Analysis . . . 72
6.1.4 Limitations . . . 72
6.2 Results . . . 73
6.2.1 Streamlines . . . 73
6.2.2 Vortex structures . . . 74
6.2.3 Boundary treatment . . . 77

7 Conclusion and future work **80**

A Radial Basis Functions use in the code **87**

List of Figures

1.2 Figure 2: Schematic of PIV process. 4
1.1 Particles around an airfoil at $\alpha = -15^{\circ}$. 4
1.3 Processed velocity field with streamlines and velocity magnitude. 4
1.4 Lagrangian particle tracks (Schneiders and Scarano [2016]). 5
1.5 Iso-surfaces of the Q-criterion (Schneiders and Scarano [2016]). 5

2.1 Time-super sampling at Super Sampling Factor (SSF=24), which refers to the ratio between the time step of the high-resolution super-sampled data and the time step of the original data. The graph shows the velocity evolution of a point close to the trailing edge. 8
2.2 Transport of a fluid streamline by advection. 8
2.3 VIC time-supersampling principle, which can increase the time resolution of PIV data by leveraging spatial information. 9
2.4 Spatial super-resolution principle illustrated, where the VIC+ algorithm is used to increase spatial resolution starting from sparse, time-resolved PTV data. 10
2.5 VIC-TSA principle visualized. 10
2.6 Optimization problem for VIC-TSA (Scarano et al. [2022]). 10
2.7 Track regimes, depending on the length of the assimilated time segment. . 11
2.8 Amplitude modulation u^* vs seeding concentration (Scarano et al. [2022]). 12
2.9 Padding volume (Wang et al. [2022]). 13
2.10 Visual abstract of Jeon et al. [2022]. 13
2.11 Visual comparison of different reconstruction methods. 14
2.12 Visual abstract of Cakir et al. [2022]. 17
2.13 PIV performance in reconstructing turbulence quantities (Schneiders et al. [2017]). 18

3.1 Particle tracks and regimes. The figure depicts the trajectory of tracer particles, highlighting the effective distances $\bar{r}$ and $\tilde{r}$ that govern the spatial resolution in VIC-TSA. 22

3.2 Schematic of the VIC-TSA reconstruction framework. Velocity and vorticity are initialized (black arrow) from tracks data at the center of the time-segment (t0) by interpolating tracks data from the measurements. Time marching by vortex-in-cell (blue arrows) along the chosen time-segment. The cost function J is evaluated from the differences between the computed velocity and the tracks data. The cost function is minimized iteratively (grey line arrow) yielding the optimized velocity field at t0.(Scarano et al. [2022]). . . . 23
3.3 Flowchart of VIC-TSA . . . 26
3.4 Forward and backward problem for adjoint method (Giering and Kaminski [1999]). . . . 28

4.1 Simplified scheme of VIC-TSA with RBF. . . . 33
4.2 Gaussian radial basis function and its derivative. . . . 36
4.3 Grid spacing and lexicographic ordering of the unknowns. . . . 37
4.4 A matrix, with explicit RBF value for all the distances between the points. 37
4.5 Testcase of RBF interpolation and derivative computation. Ground thruth above and reconstruction with interpolation error below. . . . 40

5.1 Taylor Green vortex lattice. . . . 45
5.2 Tracer particles leaving the domain of interest, reducing the seeding density in the highlighted area. On the background: $v(x, y)$ velocity component. . 47
5.3 RK45 vs Euler time tracking method. . . . 47
5.4 Generated tracers . . . 48
5.5 Material derivative. . . . 49
5.6 Artificial tracers, slice of the $u(x, y)$ component . . . 49
5.7 Example of $u^* - r^*$ plot. . . . 52
5.8 Ground thruth flow, with a grid point covering each peak. . . . 52
5.9 Amplitude modulation. . . . 54
5.10 Amplitude modulation, global comparison. . . . 55
5.11 $v(x, y)$ velocity component, reconstruction with VIC-TSA without radial basis functions. . . . 57
5.12 $v(x, y)$ velocity component, reconstruction with VIC-TSA with radial basis functions. . . . 58
5.13 Particle tracks characterized by the same t^*, but different dt^*. . . . 59
5.14 Interpolation for different functions with the same number of sample points. 61
5.15 Interpolation errors for the different functions. . . . 61
5.16 Errors for different interpolation methods across the three functions. . . . 62
5.17 Mesh convergence analysis for VIC-TSA and LI on Taylor-Green flow. . . . 63

5.18 Amplitude modulation for flow with added noise reconstructed with VIC-TSA at different N_t and RBF configurations. The results are plotted vs. the SNR and the standard deviation of the noise. 65

6.1 DNS data at $Re = 2750$ with iso-surfaces of the Q-criterion colored by the streamwise velocity (Wang et al. [2022]). 69
6.2 Schematic of the experimental setup. Top view (top) and front view (bottom). The measurement volume is in red. 70
6.3 Experimental setup. A flat plate with the hemisphere is mounted inside the open section of the wind tunnel. 71
6.4 Shake-The-Box tracks colored by velocity magnitude. 73
6.5 Iso-surfaces of the $\lambda 2$ criterion colored by the streamwise velocity u. 75
6.6 Streamlines for side view (left) and top view (right), at a height $z = 23\,\mathrm{mm}$. 76
6.7 Uniform structured mesh with the immersed boundary surface for VIC+ and ImVIC+ (left) and curvilinear boundary fitted mesh on the hill surface for ALE-VIC+ (right), (Cakir et al. [2022]). 77

7.1 Alternative RBF kernel. 81

List of Tables

5.1 DaVis Particle Track Data Sample 50
5.2 t^* values obtained in this work. 56
5.3 t^* values by Scarano et al. [2022]. 56
5.4 t^* values. 56
5.5 Parameters of the analysis 63

6.1 Experiment parameters 71

Acronyms

ALE Arbitrary Lagrangian-Eulerian. 17, 77

DNS Direct Numerical Simulaition. 44

DoFs degrees of freedom. 31

FFT Fast Fourier Transform. 39

GRBF Gaussian Radial Basis Functions. 33

HFSB Helium-Filled Soap Bubbles. 4, 5, 68

IW interrogation window. 51

LPT Lagrangian particle tracking. 1, 5, 21

PINN Physics-Informed Neural Network. 2, 7, 68, 69

PIV Particle Image Velocimetry. 1, 3, 6

PTV Particle Tracking Velocimetry. 3, 6, 21, 58

RBF Radial Basis Functions. iii, 3, 11, 19, 27, 31, 32, 87

STB Shake-The-Box. vi, 5, 14, 15, 43, 45, 50, 53, 72, 73

TSA Time-Segment-Assimilation. 2, 10

VIC Vortex-in-Cell. 2, 6, 8, 21

VIC-TSA Vortex-in-Cell with Time-Segment-Assimilation. 21

Chapter 1

Introduction

1.1 Background

Fluid dynamics plays a crucial role in a wide range of scientific and engineering applications, ranging from aerospace engineering to environmental studies. Accurate experimental analysis of fluid flows is essential for advancements in these fields. However, capturing the intricate details of fluid motion poses significant challenges. Particle Image Velocimetry (PIV) has established itself as an effective and non-intrusive flow measurement technique that can provide quantitative information on the entire velocity field at a certain time. It works by filling the flowfield with tracer particles, illuminating them with a powerful light pulse, and tracing their position with high-speed cameras. Further details are provided in Section 1.5. Recent advancements in Lagrangian particle tracking algorithms (Schanz et al. [2016]) made it possible to track each particle individually, providing a high degree of resolution.

1.2 Problem statement

With Lagrangian particle tracking, it is possible to determine the velocity and acceleration of each particle at each time snapshot. Each particle acquired in multiple time snapshots identifies a *particle track*. The problem with this is that the measured data will be sparse, because the Lagrangian particle tracking will calculate velocity and acceleration at each particle location. Even if the dynamics of the flow gets captured very well, it is not in a very useful format for post-processing visualization or computation of quantities like the gradient of the velocity field, which usually requires the data to be in a Cartesian format. Reconstruction methods for PIV here come into play, which basically reconstruct the velocity field on a Cartesian grid. One might wonder why not to use linear interpolation (LI) or other similar methods, and the answer is that this would not ensure that the new Cartesian flowfield obeys the physical constraints; reconstruction methods often integrate

physical laws (like the Navier-Stokes equations) into their algorithms. This ensures that the reconstructed velocity fields are physically consistent, which might not be the case with simpler methods like LI.

Moreover, even if one the velocity field is reconstructed correctly, what about all the available time information that is contained in the acceleration data or in the other time snapshots? It can be leveraged by reconstruction algorithms not only to bring the information into Cartesian format, but also to **increase the space resolution** of the original measurements, by reconstructing on a Cartesian grid that has a grid spacing smaller than the average interparticle distance of the tracers. This process was named by Schneiders and Scarano [2016] as *pouring time into space*, and it actually allows one to go beyond the limits of the experimental setup. The opposite also holds: space information can be used to leverage time information (Schneiders et al. [2014]), and extract time evolutions of the flow that are way below the Nyquist cryterion.

Different reconstruction methods mainly differ for the way they impose the physical constraints: Navier-Stokes equations (Schneiders et al. [2014], Schneiders and Scarano [2016], Scarano et al. [2022]), Physics-Informed Neural Network (PINN) (Wang et al. [2022]), splines with incompressibility constraints (Gesemann et al. [2016]).

1.3 Research objectives

This thesis will focus on space-resolution reconstruction methods that make use of the Navier-Stokes equations based on the vorticity field, also referred to as the Vortex-in-Cell (VIC) approach. An example is the VIC+ method (Schneiders and Scarano [2016]), which leverages the time information of the acceleration (material derivative of the velocity) and the governing laws, to produce a Cartesian velocity field that fits best with the experimental data.

An evolution of this method was proposed by Scarano et al. [2022] with the VIC-TSA method. Time-Segment-Assimilation (TSA) stands for the way this method assimilates the time information: it includes other time snapshots in the minimization problem, instead of the acceleration. However, this method has not exceeded VIC+ in specific scenarios that will be explained better later.

This thesis aims to explore the enhancement of VIC-TSA's accuracy through the implementation of Radial Basis Functions (RBF). It investigates how the incorporation of RBFs can improve VIC-TSA and how well it compares with other metrics and methods, by providing a numerical investigation on a synthetic flowfield and an experimental assessment of the flow over a bluff body.

1.4 Structure of the thesis

This thesis is organized in the following way:

1. General notions about Particle Image Velocimetry and Particle Tracking Velocimetry are given.

2. Then, the state-of-the-art and relevant literature is reported, with focus on the key concepts that will be part of this work.

3. The VIC-TSA framework is then introduced with its theoretical foundations and numerical implementation, to provide background information to the reader and describe the areas object of modifications.

4. The implementation of the Radial Basis Functions into VIC-TSA is then detailed, from the mathematical details to the implementation into the code.

5. Subsequently, the numerical assessment procedure for evaluating the new implementations is described, with the reconstruction of the Taylor-Green vortex test case. The results of the synthetic flow reconstruction for different cases are then shown, comparing different methods and the effect of the RBFs; particular relevance is given in testing convergence and robustness to noise.

6. Finally, an experimental assessment with the flow over a wall-mounted hemisphere is presented, to demonstrate the effect of the improvements on a real-case scenario.

1.5 Overview of PIV and PTV

Aerodynamics research extensively uses Particle Image Velocimetry (PIV) and Particle Tracking Velocimetry (PTV) as experimental techniques to visualize and analyze the flowfield. These experimental methods introduce tracer particles into the fluid and track their movement to infer the flow properties. The choice of technique depends on the specific characteristics of the flow under investigation and the desired spatial and temporal resolution.

1.5.1 Particle Image Velocimetry (PIV)

PIV is employed in a controlled environment where the flow is seeded with small particles that are assumed to follow the flow dynamics faithfully. These are typically micron-size fog droplets and produced with a generator installed in a wind tunnel. More recently, larger tracers have been introduced to achieve a larger measurement domain in wind tunnels. Such tracers are sub-millimetre Helium-Filled Soap Bubbles (HFSB, Caridi [2018]). A typical PIV setup includes a laser to illuminate the particles and high-speed cameras to capture a quick pair of sequences close in time, so that the movement of the particles can be inferred. The imaging area is divided into numerous *interrogation windows* in 2D or *interrogation volumes* in 3D. Then, the *cross-correlation* between image pairs is applied, where the most probable displacement of particles within each window is identified. This displacement yields the velocity field by relating it to the time interval between frames.

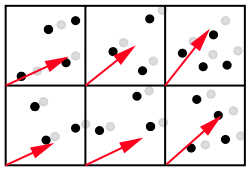

Figure 1.2: Figure 2: Schematic of PIV process.

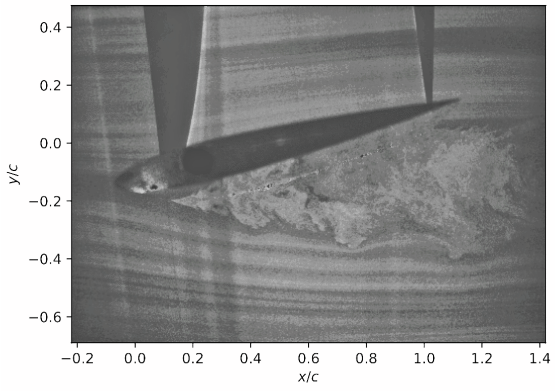

Figure 1.1: Particles around an airfoil at $\alpha = -15^{\circ}$.

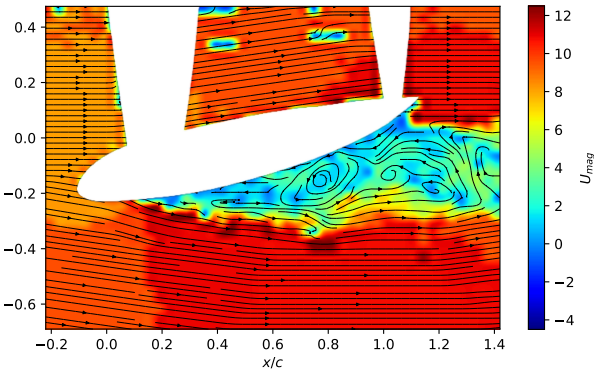

Figure 1.3: Processed velocity field with streamlines and velocity magnitude.

The resultant velocity field serves as a vector map that provides instantaneous spatial flow characteristics. Researchers can derive additional dynamic properties from this field, such as vorticity, to gain deeper insights into flow behavior, especially in turbulent regimes.

1.5.2 Particle Tracking Velocimetry (PTV)

PTV, meanwhile, is an experimental technique that offers a Lagrangian perspective by tracking the paths of individual particles over time. A PTV experimental setup often involves equipment similar to PIV but is optimized for tracking individual particles across a series of images, by using cameras that can record at a high acquisition frequency continuously, rather than only for an image pair. By using Lagrangian particle tracking algorithms like Shake-The-Box (Schanz et al. [2016]), this method allows the reconstruction of particle trajectories in three dimensions, providing time-resolved flow information. Recently, Helium-Filled Soap Bubbles (HFSB) have been successfully used in PTV because of their increased dimension, while maintaining a relatively low weight, which helps them scatter more light.

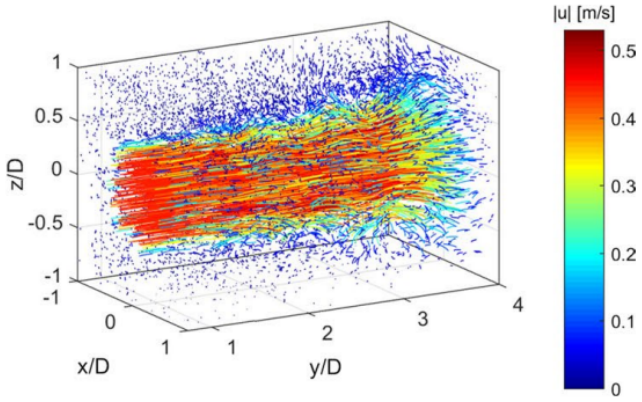

Figure 1.4: Lagrangian particle tracks (Schneiders and Scarano [2016]).

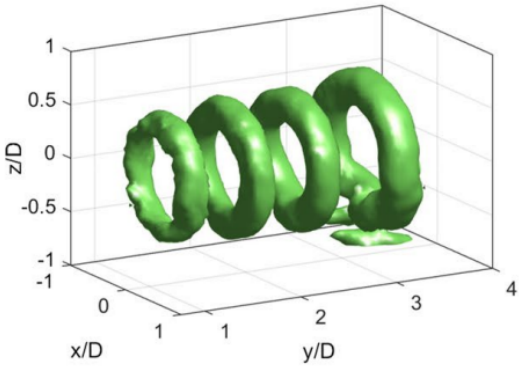

Figure 1.5: Iso-surfaces of the Q-criterion (Schneiders and Scarano [2016]).

Trough PTV, it is possible to observe and analyze the temporal evolution of flow structures within the flow, but the Lagrangian particle tracking allows for greater resolution. For example, in PIV with cross-correlation Figure 1.2, the movement of multiple particles is averaged to find a single velocity vector for each interrogation window, while with PTV each particle is tracked individually.

Chapter 2

Data assimilation techniques

2.1 Introduction

In the following, the state of the art of data assimilation methods is presented. T the topic of reconstruction methods for Particle Image Velocimetry (PIV) will be explored, focusing more on the Navier Stokes-based approach like the Vortex-in-Cell (VIC) method (Schneiders et al. [2014]) and its evolutions, which have been studied with particular attention here at TU Delft. The papers presented emphasize the development of the technique in terms of accuracy and fields of applications, highlighting the differences between existing reconstruction methods and identifying potential areas for advancement.

Reconstruction methods in fluid dynamics refer to a range of computational techniques to extract additional information from Particle Image Velocimetry (PIV) data. These methods are designed to enhance the understanding of fluid flow by improving the quality and detail of the data obtained from PIV experiments. Some applications of reconstruction methods include:

- enhancing the temporal resolution of PIV experiments, where the cross-correlation is applied to interrogation windows to obtain the average velocity vector in that window. This is given as input for time-super sampling reconstruction algorithms like VIC, which will be utilized to extrapolate the velocity field both forward and backward in time. This provides a higher temporal resolution than the one imposed by the limits of the measurement setup.

- reconstruct the velocity field on a Cartesian grid in experiments where Particle Tracking Velocimetry (PTV) is employed. Such experiments yield the velocity and acceleration of every single particle, thanks to the tracking algorithm, but only at the sparse location of the tracer particles. This is not ideal for performing operations like the gradient or for flow post-processing, hence space-super resolution algorithms (like VIC+, Schneiders and Scarano [2016]) can be applied to reconstruct the velocity field on a Cartesian grid.

Other types of reconstruction methods are available and some of them will be discussed more deeply, like the Physics-Informed Neural Network (PINN).

The report is organized as follows: it progresses through an exploration of reconstruction methods in aerodynamics, highlighting advancements in both temporal and spatial resolution enhancements. Developments in particle tracking and alternative reconstruction techniques are discussed. Challenges specific to PIV, including pressure reconstruction and turbulence measurement, are examined. The chapter concludes with a summary and the formulation of key research questions.

2.2 Time-super sampling

This section describes the algorithm for time-super sampling of PIV data. It starts with the simple advection equation and introduces the VIC

Advection model The idea of increasing the temporal resolution of 3D PIV data traces back to 2012, when it was first introduced by Scarano and Moore [2012]. The first approach used was the simple advection equation to advance the flowfield in time (or travel back), creating intermediate snapshots in between the measurement frames. For a generic property ν:

$$\nu(\mathbf{X} + \mathbf{V}_{\text{conv}} \cdot \mathrm{d}t, t + \mathrm{d}t) = \nu(\mathbf{X}, t). \tag{2.1}$$

Compared to linear interpolation between two samples, the advection equation performs better because it takes into account the local movement of the flowfield, rather than just averaging between two snapshots. If Taylor's hypothesis of frozen turbulence holds, which yields that velocity fluctuations are transported passively by the bulk motion of the flow, then the advection equation works well at reconstructing the time evolution of turbulent fluctuations. An example is given by the experimental assessment of the flow past the trailing edge of a NACA0012 airfoil, where the hypothesis holds reasonably well (Figure 2.1).
This approach works because the missing temporal information is contained in space, at least for the advection-dominated flows. The principle is visualized in Figure 2.2, where the measured frequency in an Eulerian frame for a single point would be $1/2\Delta t$. But if one imagines slowly *sliding* the blue spatial distribution from t to $t + \Delta t$, all the fluctuations will be captured at that point. This is addressed by the authors as *pouring space into time*.

The second experimental assessment is a jet flow, where Taylor's hypothesis does not hold due to the dynamics of the shear layers. The method is still able to provide an improvement in temporal resolution by a factor of two.

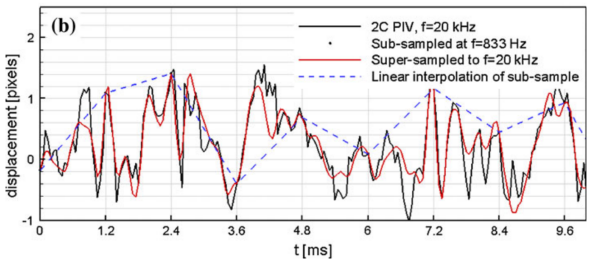

Figure 2.1: Time-super sampling at Super Sampling Factor (SSF=24), which refers to the ratio between the time step of the high-resolution super-sampled data and the time step of the original data. The graph shows the velocity evolution of a point close to the trailing edge.

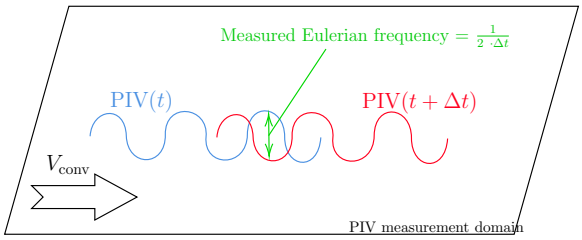

Figure 2.2: Transport of a fluid streamline by advection.

VIC The Vortex-in-Cell (VIC) method is a numerical method for solving different flow problems. It follows the trajectories of discrete particles and computes the potential vorticity as they move over an underlying Eulerian grid (Cottet and Koumoutsakos [2000]). In reconstruction methods for PIV, VIC describes the class of Navier-Stokes-based reconstruction methods that this thesis belongs to, which makes use of the Vortex-in-Cell formulation. As an evolution of the advection model, the VIC time-super sampling for PIV was introduced by Schneiders et al. [2014] to increase the temporal resolution of time-resolved PIV data for general flows. It is based on the method developed by Christiansen [1973], under the hypothesis of incompressible and inviscid flow[1], which can be applied to 3D data obtained from PIV, as already introduced. The principle of time-supersampling with VIC is schematically illustrated in Figure 2.3.
In a nutshell, the algorithm uses the Navier-Stokes equations based on the vorticity field. This is necessary to eliminate the pressure gradient from the momentum equation, because PIV cannot yield pressure measurements (see also Section 2.6):

$$\frac{D\boldsymbol{\omega}}{Dt} = (\boldsymbol{\omega} \cdot \nabla)\mathbf{u} + \nu\nabla^2\boldsymbol{\omega}. \tag{2.2}$$

So, taking as inputs the velocity vectors from the interrogation voxels (obtained, for instance, with the cross-correlation technique [2] for PIV experiments), and the (Cartesian) grid coordinates, the algorithm computes the vorticity $\omega = \nabla \times u$ and the material

[1]Which is also necessary to *travel back* in time, otherwise viscosity would introduce dissipation.

[2]The cross-correlation technique consists in dividing the measurement domain into small volumes, usually on a Cartesian grid, and then applying the cross-correlation from signal processing to find the average movement of the particles inside the volume between successive time frames.

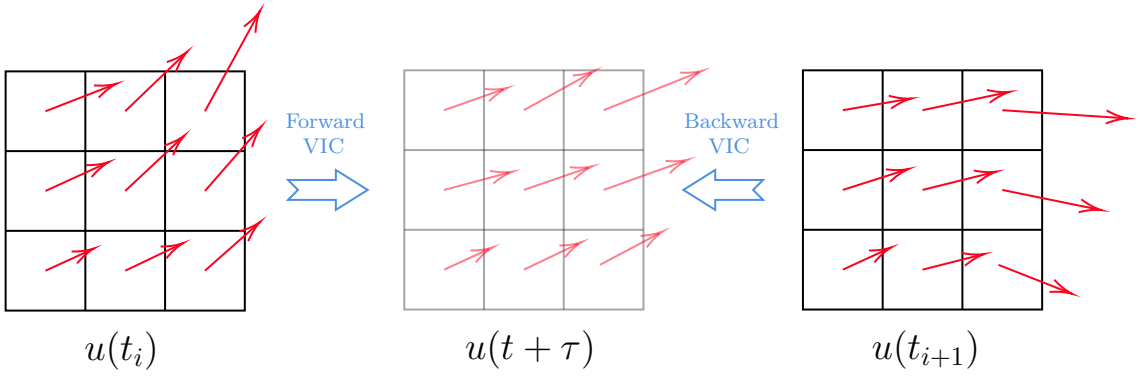

Figure 2.3: VIC time-supersampling principle, which can increase the time resolution of PIV data by leveraging spatial information.

derivative of it, used to update the velocity field at a next time frame:

$$\omega_{t+\tau} = \omega_t + \left.\frac{d\omega}{dt}\right|_t \cdot \tau. \tag{2.3}$$

The accuracy of this time-supersampling method is studied for two experimental datasets obtained from time-resolved 3D-PIV measurements: the turbulent wake of a NACA 0012 airfoil (Schneiders et al. [2014]) and a circular jet. The results are compared to linear interpolation, advection-based supersampling, and measurement data at a high sampling rate. While for the turbulent wake, both the advection-based method and the VIC produce good reconstructions, VIC was proven to be better for the circular jet, due to the strong non-linearities of the phenomenon. In both flows, the authors demonstrate the ability to reconstruct detailed temporal dynamics using data subsampled at a rate far below the Nyquist frequency.

2.3 Space super-resolution

VIC+ Reconstruction methods can be also used to deal with sparse data from a PTV experiment. Typically, modern PTV cameras can capture images at a frequency of up to several kilohertz and can be used in a tomographic setup to record the trajectory of the tracer particles. A precise Lagrangian particle tracking is ensured by the recently introduced Shake-the-Box algorithm (Schanz et al. [2016]). This yields the instantaneous velocity and its material derivative (acceleration), but only at the location of the sparse tracers, which is not very convenient for post-processing and data analysis. The VIC+ method (Schneiders and Scarano [2016]) is then used to both increase the spatial resolution and bring the information on a Cartesian grid (Figure 2.4).
The resulting mathematical problem is ill-posed, since the number of degrees of freedom, which are the unknown values of the velocity on the Cartesian grid, is higher than the

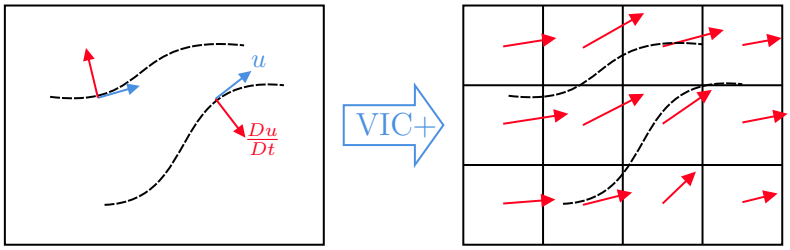

Figure 2.4: Spatial super-resolution principle illustrated, where the VIC+ algorithm is used to increase spatial resolution starting from sparse, time-resolved PTV data.

number of equations. Hence, a minimization problem is formulated, where the flow field produced by the Navier-Stokes algorithm must minimize a cost function. The additional spatial information is obtained by leveraging the temporal information available in the measurements through the velocity material derivative. Both numerical and experimental assessments here in TU Delft have shown that VIC+ performs better than traditional methods in situations where seeding concentration is limited, such as in large-scale experiments with high flow speeds and volumes. Moreover, VIC+ has been shown to offer less spatial averaging of turbulent fluctuations than the cross-correlation approach used in traditional tomographic PIV.

VIC-TSA If VIC+ works well in reconstructing the velocity field, a legitimate question might be about why not using the available information of an entire time segment $(t_i - \tau, t_i + \tau)$ rather than a single snapshot t_i. This is the idea behind the method proposed by Scarano et al. [2022]. The principle of VIC-TSA (Time-Segment-Assimilation) is to involve all the snapshots of the time segment in the minimization problem, adding them as additional constraints (Figure 2.5).

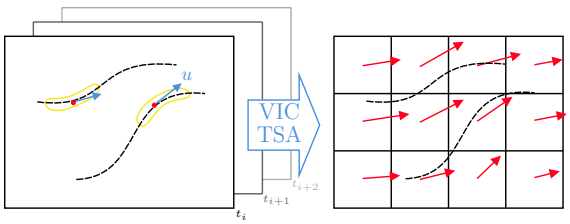

Figure 2.5: VIC-TSA principle visualized.

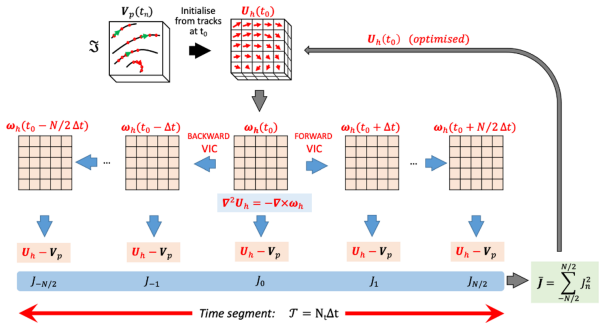

Figure 2.6: Optimization problem for VIC-TSA (Scarano et al. [2022]).

A quantitative way to describe how VIC-TSA increases the spatial resolution even further is the following: consider the particle tracks in Figure 2.7. The concept entails that the

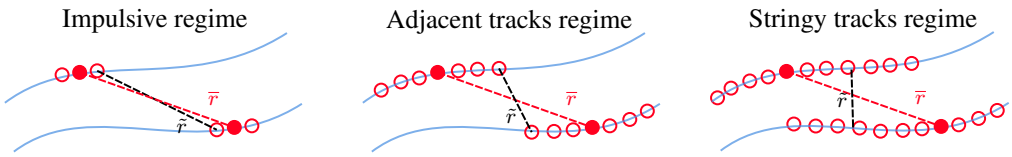

Figure 2.7: Track regimes, depending on the length of the assimilated time segment.

dependency of spatial resolution is shifted from the particles' distance, hereby referred to as $\overline{r}$, to the tracks' distance, $\tilde{r}$, which will be shorter as the time segment is increased. As a result, the increase in spatial resolution is expected to be proportional to $\tilde{r}/\overline{r}$. As it will be better explained in the dedicated chapter 3, the adjacent track regime is a potential optimum since increasing the time segment even further will not decrease $\tilde{r}$ furtherly.

Scarano et al. [2022] compared to VIC+ and linear interpolation in evaluating a synthetic vortex flowfield, particularly focusing on the modulation of the reconstructed amplitude values with respect to the analytical expression.
Figure 2.8 shows that the linear interpolator proved to be the worst at reconstructing the velocity field, as expected for this baseline case that does not actually extrapolate additional space information. The VIC+ method showed a visibly flatter behavior that was outclassed only by VIC-TSA with 21 assimilated snapshots.

This was unexpected, as VIC-TSA at a low time assimilation setting was expected to give similar results to VIC+, as the additional time information yielded by the instant material derivative in VIC+ can be roughly be assimilated to VIC-TSA in the impulsive regime (Figure 2.7). This is ascribed by the authors to a more accurate optimization in the VIC+ algorithm due to the use of Radial Basis Functions (RBF), not implemented in the VIC-TSA algorithm for computational affordability. RBFs are interpolants that have unique properties of global support and smoothness requirements, which can improve and stabilize the convergence of the optimization loop in VIC-TSA, yielding to a more accurate flow fitting.**The study of the effect of RBF in the VIC-TSA algorithm** is the main objective of this thesis project, in order to further increase its performances.

In the study, the VIC-TSA method's effectiveness is demonstrated experimentally using a large-scale Particle Image Velocimetry (PIV) setup conducted in a Karman wake behind a circular cylinder, with a Reynolds number of 27000. These experiments, carried out in a low-speed wind tunnel at TU Delft, utilized sub-millimeter helium-filled soap bubbles as flow tracers. The measurements covered a domain encompassing the near wake of the cylinder, and the data processing involved Shake-the-Box analysis for tracer motion evaluation. The results from these experiments showed that increasing the time segment length for the TSA method led to a more consistent resolution of spatial scales, particularly in capturing both primary vortex structures and interconnecting ribs in the complex flow field. The analysis indicated that a time-segment length corresponding to τ^* = 2 offers an optimal balance, yielding an approximate 30 % increase in the amplitude of

vorticity fluctuations compared to shorter time segments

VIC# This method was proposed by Jeon et al. [2022] by LaVision and it is basically a complement to VIC+. It improves certain aspects of the latter, in terms of computational efficiency and boundary treatment, where the method was known to show some small artifacts. The reason for this is that the distribution of tracer particles is usually lower at the extremes of the domain, which is a problem for imposing the boundary conditions. In order to get the velocity from the vorticity field, VIC+ has to solve the Poisson equation:

$$\nabla^2 u = -\nabla \times \omega. \tag{2.4}$$

This requires a set of boundary conditions to be imposed; some of them are known, like the no-slip condition at the walls, and freestream values when possible depending on the flow case (Schneiders and Scarano [2016]). The other boundary conditions are unknown and need to be updated from the optimization procedure. That is why a lower seeding concentration at the boundaries causes a poor update of these boundary conditions. To account for this, a *padding volume* (Figure 2.9) was added to stabilize the convergence, acting like a "buffer" region, at the cost of increasing the computational cost considerably.

With VIC#, the author proposes to use only a very small amount of padding volume, and at the same time add the physical constraints of incompressibility and the Navier-Stokes equations in the cost function, similarly to what happens in the other data assimilation methods (FlowFit, Gesemann et al. [2016], see in 2.4). The procedure is assessed experimentally with the jet flow test case and synthetic DNS data and shows significant improvement at the boundaries (Figure 2.10). Here, it becomes evident that the added constraints effectively impose the freedom of divergence at these peripheral regions.

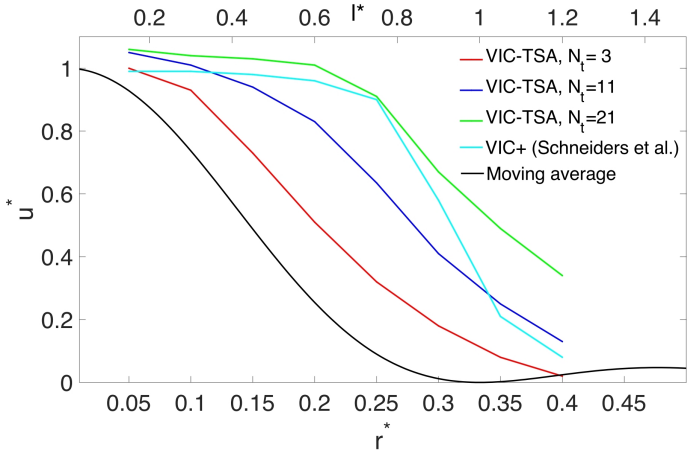

Figure 2.8: Amplitude modulation u^* vs seeding concentration (Scarano et al. [2022]).

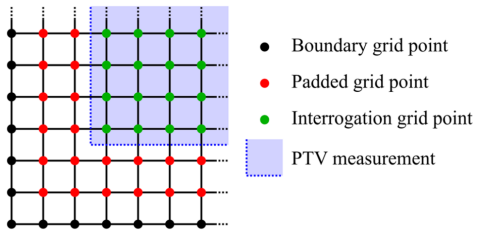

Figure 2.9: Padding volume (Wang et al. [2022]).

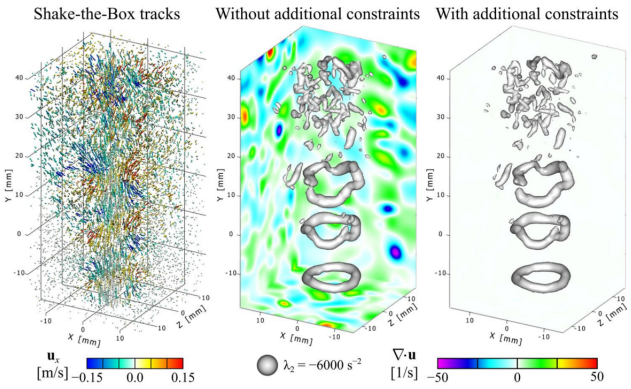

Figure 2.10: Visual abstract of Jeon et al. [2022].

2.4 Other types of reconstruction methods

PINNs Wang et al. [2022] discusses the use of a physics-informed neural network (PINN) to reconstruct dense velocity fields from sparse experimental data obtained through particle image velocimetry (PIV) and particle tracking velocimetry (PTV). The authors propose a PINN-based data assimilation method that approximates both velocity and pressure by means of a neural network that takes as inputs the position of the particles and time. The hidden layers (that act as the solver) output the velocity components and the pressure, and some differentiation operators are employed to enforce the Navier-Stokes equations on these outputs. In this way, the Neural Network can be trained with a physics-based loss function. This allows the PINN to improve velocity resolution and also to predict the pressure field with a 10% error.

The performance of the PINN is investigated using Taylor's decaying vortices and turbulent channel flow with and without measurement noise. The authors assess various parameters of the proposed method, including activation functions, optimization algorithms, and data parameters. They also explore the ability of the PINN to reconstruct wall-bounded turbulence.

Finally, the PINN is applied to reconstruct dense velocity fields from experimental tomographic PIV (Tomo-PIV) velocity in the three-dimensional wake flow of a hemisphere (Figure 2.11). The results indicate that the proposed PINN has great potential for extending the capabilities of PIV/PTV, even though the experimental setup proposed by the authors is limited and there are no comparisons with more advanced reconstruction methods like VIC+.

FlowFit This method was developed by Gesemann et al. [2016] initially out of necessity, in order to participate in the 2014 PIV challenge with what became the Shake-the-Box (Schanz et al. [2016]) particle tracking algorithm, the first key step that enabled the

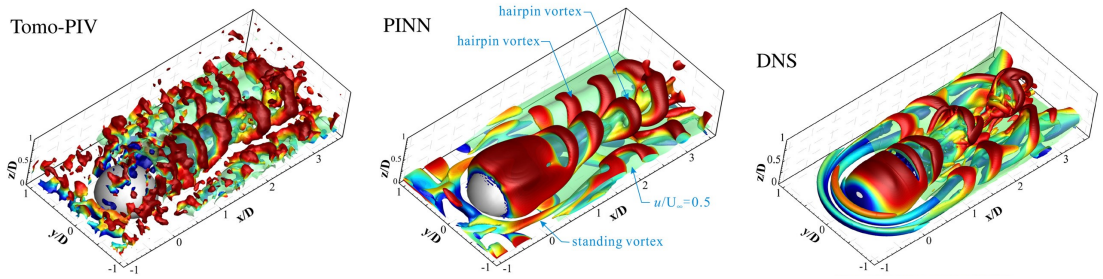

Figure 2.11: Visual comparison of different reconstruction methods.

development of more precise measurement methods that do not suffer from low-pass filtering (like it happens for all the window averaging techniques like the cross-correlation analysis). In its simplest form, it consists essentially of a spline-based interpolation of the velocity field, with the possibility of adding penalizations in order to enforce freedom of divergence or incompressibility. The proposed approach can be split into two parts:

1. *TrackFit* is used to create a spline for the particle track itself. It takes the (noisy) particle tracks and applies a technique similar to Kalman filtering in order to reduce the noise and allow for the computation of the first and second derivatives. These are essential to obtain the velocity and the acceleration, and, in some sense, this step can still be considered part of the STB algorithm.

2. *FlowFit* takes as inputs the velocity, acceleration, and position of the particles and computes 3D B-splines for velocity, acceleration, and also pressure.

The difference between FlowFit and VIC methods is that in the latter the interpolation is carried out with the Navier-Stokes equations, while FlowFit is a data assimilation method that can enforce some physical constraints in the cost function. Nonetheless, it is still difficult to prove which methods perform best, regardless of the accuracy of the model, and VIC methods suffer from additional computational complexity. Here is an example of how splines are used to represent the 3D velocity field:

$$\vec{v}(\mathbf{x}) = \sum_i \sum_j \sum_k c_{i,j,k} \cdot \beta_{3\mathrm{D}} \left(\mathbf{x} - x_{l,j,k} \right), \tag{2.5}$$

where $\mathbf{x}$ is the generic location in a 3D space and i, j, k the indexes of a Cartesian grid point, which are the points around which the splines $\beta_{3\mathrm{D}}$ and their coefficients $c_{i,j,k}$ are built, as result of a least squares approach. This separate reconstruction of velocity and acceleration is rather simple and computationally efficient. However, this does not allow us to enforce all the constraints that should be satisfied according to the flow physics: for instance, while the divergence of the velocity is zero, we know that the divergence of its

time derivative should also be zero:

$$\nabla \cdot \vec{u} = 0 \implies \nabla \cdot \frac{\partial u}{\partial t} = 0. \tag{2.6}$$

The second generation of FlowFit allows to perform such operations and combine the two optimization problems using a non-linear optimization algorithm. This guarantees the addition of a second physical constraint to the optimization.

One interesting thing to point out is that FlowFit introduced the effect of viscosity for the first time in a data assimilation procedure for PIV. This had a particular effect on the synthetic test case "Forced Isotropic Turbulence", where neglecting viscosity led to noticeably worse reconstructions. The assumptions made and the reason why viscosity terms are neglected in VIC will be described later in the present work.

2.5 Lagrangian particle tracking

Since its introduction by Elsinga et al. [2006], TOMO-PIV has been used extensively thanks to the possibility of reconstructing 3D velocity fields and its reliability. This technique, though, has some important limitations:

- it uses the cross-correlation approach on interrogation volumes (voxels) to find the average displacement of the particles inside it, which is then used to find the velocity. This acts as a spatial low-pass filter, since the smallest flow structures will be inevitably lost due to the averaging effect;
- the computational cost is relatively high, considering that an iterative approach has to be applied to reduce the reconstruction error. Moreover, the algorithm starts from scratch for every new time snapshot, without any possibility of using the already existing information to partially predict the next time frame;
- ghost particles have a significant influence on the reconstructed velocity.

These limitations showed that it was desirable to gain direct knowledge of particle positions in space. Here is where Lagrangian particle tracking and the Shake-The-Box (Schanz et al. [2016]) method come into place. Knowing the particle track, this algorithm can drastically reduce computational time by extrapolating the particle position at the next time step. The following iterative procedures to match the prediction with the observed data ('shaking') will then be pretty short, because the solution is similar to the previous one. The process can be divided into two parts:

1. *Initialization:* even if the method is able to extrapolate the particle location pretty accurately, there is no information about any track or particles at the beginning of the operations. For this reason, a more 'traditional' particle detection method has to

be used to detect the location of each particle in the measurement domain. This is done for the first n_{init} time steps, in order to successively extract coherent trajectories from the particle distribution. This is done with a search radius algorithm. All the particles that do not belong to a track are potential ghost particles.

2. *Convergence and shaking:* the algorithm is now ready to extrapolate the particle location from the track and correct the prediction with the actual image at the next time frame. Here the concept of *shaking* the particles comes into play: each detected particle is moved slightly around its location, until it minimizes the error with the recorded image. The error is quantified with the residual intensity, defined as:

$$I_{\text{res}} = I_{\text{measured}} - I_{\text{predicted}}. \tag{2.7}$$

Ghost particles will be detected and eliminated easily, since they do not converge. The process is then repeated for the next time frame and it is self-stabilizing.

In order for STB to work properly, the extrapolation of the particle's position from its track should be fairly precise, which means that an accurate calibration is required. For all the other aspects, STB has proven to be extremely convincing and permitted the development of more advanced reconstruction methods and measurements.

2.6 Challenges of PIV

Pressure reconstruction PIV is known to provide velocity measurements, with no information about the instantaneous pressure field. The idea of getting pressure measurements with PIV is very appealing, because of the non-intrusive nature of the method. Reconstruction methods can be also used to compute the pressure field from an instantaneous velocity field (Van Oudheusden [2013], Schneiders et al. [2016]), obtained for instance with tomographic PIV and cross-correlation analysis, even if with some important limitations. The VIC framework is still used to compute the material derivative of the velocity, used then to obtain the pressure gradient:

$$\nabla^2 p = -\rho \nabla \cdot \frac{Du}{Dt}, \tag{2.8}$$

with mixed boundary conditions. There are some important limitations, though, imposed by theoretical limits:

- by applying Helmholtz decomposition, the velocity field can be decomposed into a curl-free (potential) and divergence-free part:

$$u = u^{\phi} + u^{\psi} = -\nabla\phi + \nabla \times \psi. \tag{2.9}$$

the first can only be estimated from the boundary points, which are in a smaller number. This makes it particularly sensitive to errors and makes the procedure difficult to apply in flows dominated by potential velocity fields;

- the Poisson equation used to get the velocity derivatives can be split into two components: a homogeneous Poisson equation with non-homogeneous boundary conditions and a non-homogeneous Poisson equation with homogeneous boundary conditions. Since the PIV system does not measure the boundary conditions of $\frac{\partial u}{\partial t}$, the latter is difficult to solve.

Boundary treatment Cakir et al. [2022] tackle the challenge of accurately interpolating Lagrangian Particle Tracking (LPT) data in areas close to solid boundaries by proposing two computational fluid-structure interaction frameworks, ALE-VIC+ and ImVIC+. The first introduces the Arbitrary Lagrangian-Eulerian (ALE) approach to VIC+ and the other uses the immersed boundary method. These are designed to effectively handle boundary-induced phenomena within LPT data, which is often sparse near obstructions due to shadowing effects or measurement limitations.

This paper first discusses the inherent limitations in the spatial resolution of LPT measurements and recent attempts to enhance it near solid boundaries using data assimilation methods. Then, it validates the methods introduced against high-fidelity numerical

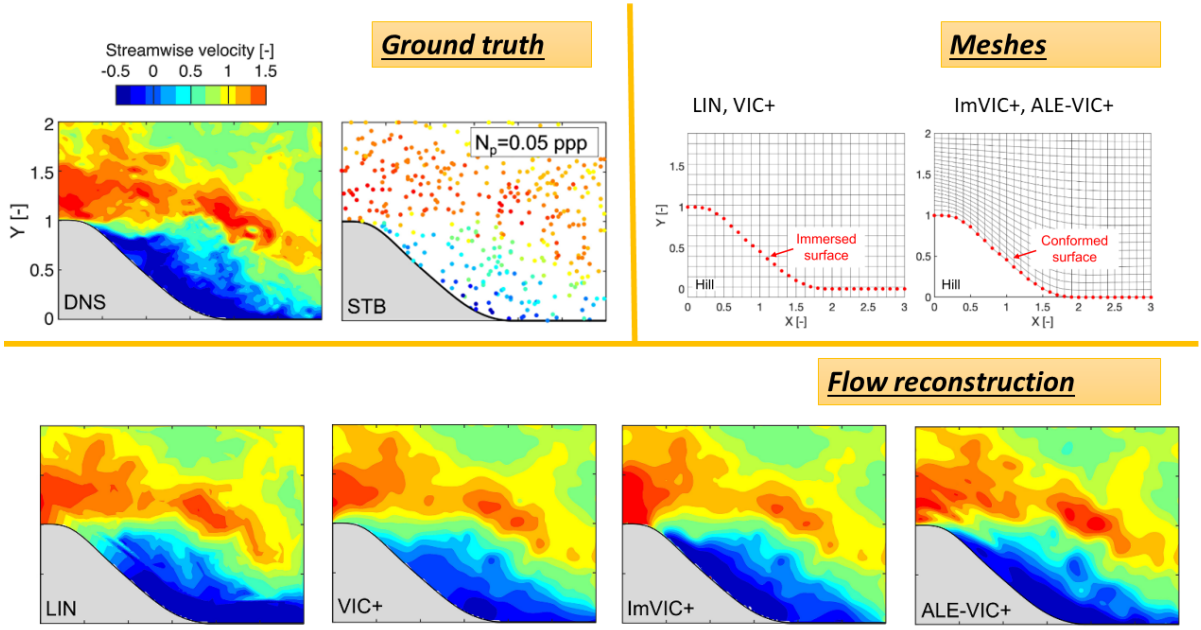

Figure 2.12: Visual abstract of Cakir et al. [2022].

simulations of flow over periodic hills, demonstrating their superiority in reconstructing flow fields near the interaction surfaces (Figure 2.12). A uniform structured mesh with the immersed boundary surface is used for VIC+ and ImVIC+, and a curvilinear boundary fitted mesh on the hill surface for ALE-VIC+. The experimental application calculates the pressure distribution over an unsteadily moving elastic membrane, revealing the interaction between the flow structures and the membrane deformations.

The study highlights the benefits of ALE-VIC+ and ImVIC+ in estimating the velocity profiles and pressure gradients near solid boundaries. It contrasts these with traditional approaches like AGW (Adaptive Gaussian Windowing) and linear interpolation, emphasizing the improvements in accuracy and the capability to capture complex flow details without increasing computational costs, typically associated with higher accuracy or more detailed simulations.

Turbulent dissipation and vorticity Quantities like vorticity and turbulent dissipation rate are quite challenging to measure with PIV, since they depend, respectively, on the velocity gradient and the velocity gradient squared. For this reason, they are very sensitive to spatial resolution, and tomographic PIV has always struggled to provide good agreement with DNS data near the wall.

Schneiders et al. [2017] presents a study on improving the spatial resolution of turbulent flow measurements using tomographic particle tracking velocimetry (PTV) and the vortex-in-cell-plus (VIC+) technique. The researchers reprocessed existing time-resolved tomographic particle image velocimetry (PIV) measurements in a turbulent boundary layer to compare the small-scale flow properties, specifically vorticity and turbulence dissipation. The tomographic PTV particle track measurements were interpolated using VIC+ to a dense grid, incorporating information on particle velocity and Lagrangian acceleration.

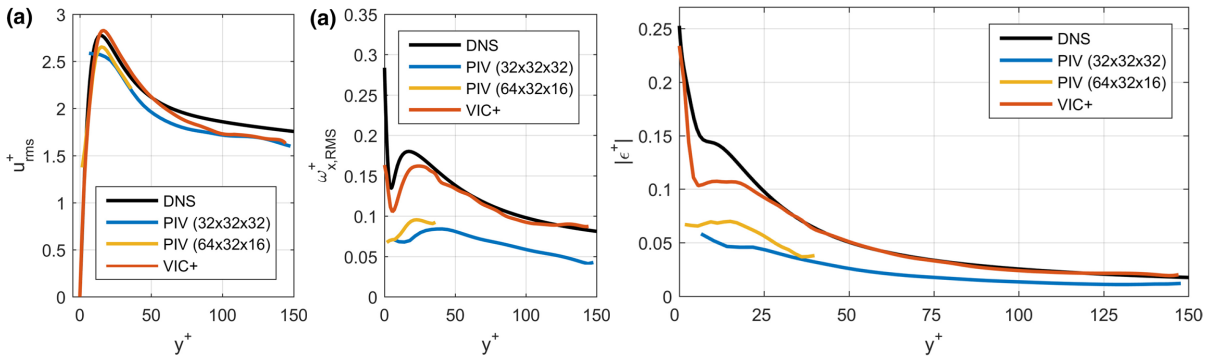

(a) Velocity fluctuations. (b) Vorticity (RMS). (c) Dissipation rate.

Figure 2.13: PIV performance in reconstructing turbulence quantities (Schneiders et al. [2017]).

The study compared the vortical structures obtained through visualization of isosurfaces of vorticity magnitude and found that both methods produced similar coherent vortical structures. However, VIC+ demonstrated increased strength in terms of vorticity magnitude, suggesting an improved spatial resolution.
Statistical evaluation revealed that tomographic PIV underestimated the root mean square (RMS) of vorticity fluctuations by approximately 40% compared to a reference profile from a DNS simulation. In contrast, the VIC+ technique returned RMS vorticity fluctuations within 10% of the reference, indicating its efficacy in capturing vortical dynamics more accurately. The study also highlighted the novel aspect of directly measuring dissipation through volumetric experiments, contrasting with other approaches that rely on 2D measurements combined with isotropic turbulence assumptions or corrections based on sub-grid scale turbulence modeling. VIC+ proved to estimate the dissipation statistics with a 5% error, versus a 50% error yielded by tomo-PIV analysis (see Figure 2.13).

The study has demonstrated the potential of the VIC+ technique in improving the spatial resolution and accuracy of near-wall turbulent flow measurements, specifically in capturing vorticity and dissipation characteristics in a turbulent boundary layer. It highlights the limitations of traditional tomographic PIV and emphasizes the importance of innovative techniques for more reliable flow analysis.

2.7 Conclusions and research questions

As highlighted in this state of the art, the Vortex-in-Cell Time-Segment Assimilation (VIC-TSA) method holds promise for achieving superior spatial super-resolution accuracy. However, its performance did not significantly exceed that of the VIC+ method, particularly at low time segment assimilation settings, where it showed even less precision. This limitation has been attributed to the absence of Radial Basis Functions (RBF) implementation in the VIC-TSA framework, as discussed in Scarano et al. [2022].

This leads towards the primary research question of this thesis, which focuses on exploring the role of Radial Basis Function (RBF) in enhancing VIC-TSA's accuracy. The question arises from the observation that the absence of Radial Basis Functions (RBF) in VIC-TSA may be a contributing factor to its performance issues, as suggested in Scarano et al. [2022]:

"***How can the integration of RBF improve the VIC-TSA method's accuracy?***"

Additionally, considering the foundational aspects of VIC-TSA and its relationship with VIC+, it becomes pertinent to examine the potential of VIC-TSA when enhanced with RBF. This inquiry is especially relevant in understanding the accuracy levels of VIC-TSA (especially in the impulsive regime) compared to VIC+:

"*How does the VIC-TSA, with a robust RBF implementation, compares with VIC+?*"

The insights gained from this implementation are expected to contribute to further improving the performance of VIC-TSA, which is the state-of-the-art Navier-Stokes reconstruction method.

Chapter 3

The VIC-TSA framework

The Vortex-in-Cell with Time-Segment-Assimilation (VIC-TSA) framework is a physics-based data assimilation method for Particle Tracking Velocimetry (PTV), based on the Navier-Stokes equations. It is used to increase the space resolution of an experiment with Lagrangian particle tracking (LPT) by leveraging the available time information, which is provided by all the other frames captured with the high-speed cameras. This method was introduced by Scarano et al. [2022], and it uses the formulation of the Navier Stokes based on the vorticity field, following the Vortex-in-Cell (VIC) framework (Christiansen [1973]). For this reason, it is defined as a *space-super resolution* method.

In doing this, the sparse information of the velocity field is reconstructed on a Cartesian grid, which is also beneficial for visualization, post-processing, and evaluation of differential quantities.

In a nutshell, the algorithm is formulated as a minimization problem that tries to fit the best possible field on the Cartesian grid that minimizes the disparity with the measurement data. The assimilation of an entire time segment enforces the solution to satisfy the governing equations for a finite amount of time. A simplified schematic is provided in Figure 2.6.

Definitions Some basic definitions and notation used to explain the VIC-TSA method will be hereby defined. Suppose that an experimental PTV campaign with Lagrangian particle tracking yields the particle data, which includes position, velocity and acceleration of the tracers at each time step. Each particle is tracked individually, which enables to identify the particle tracks. We define:

- $\overline{r}$: distance between the tracer particles;
- $\tilde{r}$: distance between the particle tracks (see also Figure 3.1);
- u_p: velocity of the particles, as recorded by the experimental setup with STB processing;

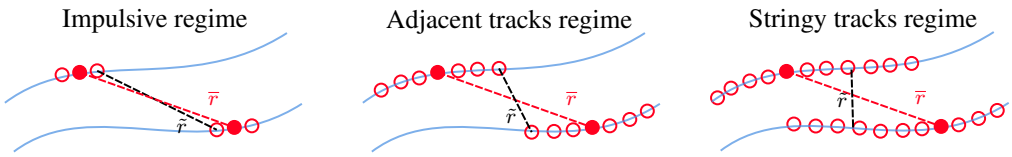

Figure 3.1: Particle tracks and regimes. The figure depicts the trajectory of tracer particles, highlighting the effective distances $\overline{r}$ and $\tilde{r}$ that govern the spatial resolution in VIC-TSA.

- u_g: velocity on the Cartesian grid;
- $u_{g,p}$: velocity on the Cartesian grid linearly interpolated to the location of the particles.

3.1 Working principle

The VIC-TSA method is founded on the premise of utilizing a finite time-resolved segment of tracer particles' positions and velocities for reconstructing the velocity field on a Cartesian grid, enhancing its space resolution. This method extends the VIC principle by assimilating the temporal evolution of particle tracks into the velocity field estimation, and it is schematically represented in Figure 3.2.

Track regimes and effective distance The fundamental principle of VIC-TSA lies in enhancing spatial resolution by assimilating time-resolved data across a defined temporal window. As visualized in Figure 3.1, this assimilation involves considering the collective path traversed by particles within this window. The effective spatial resolution, in this case, is influenced not only by the instantaneous particle separation $\overline{r}$ but also by the average track separation $\tilde{r}$ over the time segment. These distances are visible in Figure 3.1, where $\overline{r}$ represents the average distance between the particles at a given time instant, and $\tilde{r}$ symbolizes the minimum separation between the evolving particle tracks.

Time-segment length The VIC-TSA's optimization of spatial resolution is achieved by extending the assimilated time-segment $\mathcal{T}$, thus reducing $\tilde{r}$ relative to $\overline{r}$. There exists an optimal regime, identified as the *adjacent tracks regime*, where the temporal window is sufficiently large to improve spatial resolution significantly but not excessively long to impose diminishing returns on the reconstruction accuracy or to raise computational costs, since increasing the track further will not reduce $\tilde{r}$.
The selection criterion for the time segment length that identifies the adjacent tracks regime is:

$$\tau^* = \frac{\mathcal{T} U_{\text{ref}}}{\overline{r}} \approx 1,$$

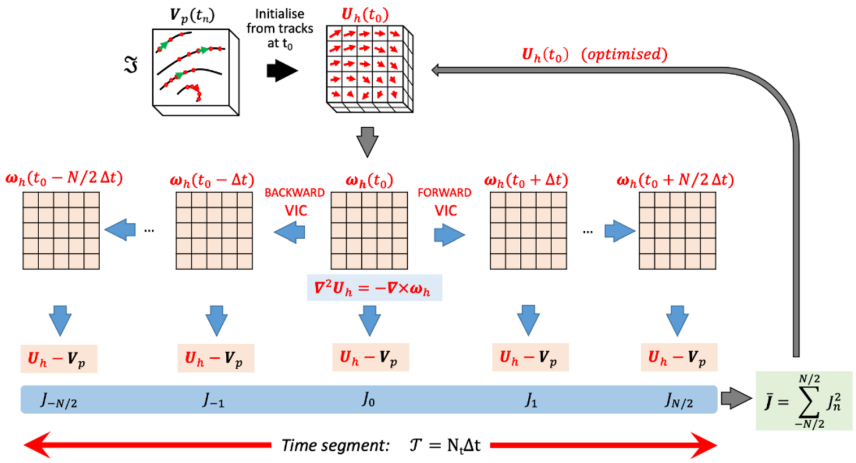

Figure 3.2: Schematic of the VIC-TSA reconstruction framework. Velocity and vorticity are initialized (black arrow) from tracks data at the center of the time-segment (t0) by interpolating tracks data from the measurements. Time marching by vortex-in-cell (blue arrows) along the chosen time-segment. The cost function J is evaluated from the differences between the computed velocity and the tracks data. The cost function is minimized iteratively (grey line arrow) yielding the optimized velocity field at t0.(Scarano et al. [2022]).

Here, U_{ref} denotes a reference velocity characteristic of the flow, $\mathcal{T}$ represents the duration of the time segment under consideration. This nondimensional parameter τ^* essentially acts as an indicator of the spatial relationship between the length of the particle tracks and their separation.

Consequences of regime selection The selection of the time segment length and the subsequent regime has implications on the analysis of the PTV data. The 'impulsive regime', characterized by a short time segment length, yields little improvement over traditional instantaneous reconstruction techniques. Conversely, the 'stringy regime', where the time segment is excessively extended, does not yield a substantial decrease in $\tilde{r}$, suggesting that an intermediate length, as exhibited by the 'adjacent tracks regime,' potentially offers an optimal balance. The concept of track regimes introduced here will be further elaborated in the algorithm section, where the mathematical and computational framework of VIC-TSA will be detailed.

3.2 The algorithm

The objective of the VIC-TSA technique is to enhance the spatial resolution of the velocity field within a specific temporal segment, ensuring that it closely aligns with the particle

velocity measurements derived from experimental data. The procedure originates from the integration of time-resolved 3D particle tracks data, which are typically acquired from techniques like tomographic Particle Tracking Velocimetry (PTV) with Shake-the-Box (STB) processing (Schanz et al. [2016]). The ensemble of particle tracks consists of spatially scattered data points capturing the particles' positions $\mathbf{x}_p$ and velocities u_p across N_t instances within a uniform time interval Δt_s.

Flow solver The VIC-TSA algorithm is initiated by interpolating the particle velocity data u_p onto a Cartesian grid, resulting in the gridded velocity u_g at the starting time t_0. Following the VIC framework (Christiansen [1973]), the VIC-TSA method uses the incompressible and inviscid vorticity transport equation, which is used to travel the flow field in time under appropriate boundary conditions. The vorticity $\omega = \nabla \times u$ is used instead of the velocity in the flow equations of VIC-TSA. This is because it cancels out the pressure gradient from the Navier-Stokes equations, which cannot be obtained with PIV (see also Section 2.6). Starting with the Navier-Stokes equation for an inviscid flow, given by:

$$\rho\left(\frac{\partial u}{\partial t} + u \cdot \nabla u\right) = -\nabla p + \mathbf{f} \tag{3.1}$$

where ρ is the fluid density, u is the velocity field, p is the pressure, and $\mathbf{f}$ represents body forces. Taking the curl of the Navier-Stokes equation and applying the property that the curl of a gradient is zero, we get:

$$\nabla \times \left(\rho\left(\frac{\partial u}{\partial t} + u \cdot \nabla u\right)\right) = \nabla \times \mathbf{f} \tag{3.2}$$

Expanding the left-hand side using the properties of the curl operator and the definition of vorticity, we obtain:

$$\rho\left(\frac{\partial \omega}{\partial t} + \nabla \times (u \times \omega)\right) = \nabla \times \mathbf{f} \tag{3.3}$$

Assuming that the body forces are irrotational ($\nabla \times \mathbf{f} = 0$), the final form of the vorticity transport equation is:

$$\frac{\partial \omega}{\partial t} = (\omega \cdot \nabla)u - (u \cdot \nabla)\omega. \tag{3.4}$$

In case of VIC-TSA, the boundary conditions are:

$$\omega(x,t) = \omega(x,t_0), \quad \forall x \in \partial\Omega, \quad \forall t \in [t_0, t_1] \tag{3.5}$$

This means that the boundary conditions are computed with linear interpolation for the central time frame only and considered constant throughout the time segment, which is an approximation The vorticity transport equation can be discretized in different ways for time marching. An example with Forward Euler:

$$\boldsymbol{\omega}_{t+1} = \boldsymbol{\omega}_t + \Delta t\left(-\mathbf{u}_t \cdot \nabla \boldsymbol{\omega}_t + \boldsymbol{\omega}_t \cdot \nabla \mathbf{u}_t\right). \tag{3.6}$$

In the code (Scarano et al. [2022]), a Runge-Kutta 4 method is used.

Velocity computation The desired velocity field can be obtained from the vorticity by solving a Poisson equation:

$$\nabla^2 u = -\nabla \times \omega. \tag{3.7}$$

Due to the boundary conditions on the vorticity, this step introduces an error. Another approach by Schneiders and Scarano [2016] involved the inclusion of the boundary conditions as degrees of freedom in the optimization loop.

Optimization loop The VIC-TSA's analytical process repeats in a series of iterative steps in order to minimize a cost function J, which quantifies the disparity between the measured particle velocities and the computed velocity field across the considered time-segment T. Considering he cost function is expressed as:

$$J(T) = \sqrt{\sum_{p,n} J_{p,n}^2}, \tag{3.8}$$

where $J_{p,n}$ is the error at the n-th timestep between the particle velocity u_p and the reconstructed gridded velocity $u_{g,h}$ linearly interpolated to the particle's location:

$$J_{p,n} = u_p(\mathbf{x}_p, t_n) - u_{g,h}(\mathbf{x}_p, t_n). \tag{3.9}$$

The optimization problem is then defined as finding the initial vorticity field that minimizes the cost function:

$$\text{argmin}_\omega \; J(\omega(t_0), u_p). \tag{3.10}$$

The optimization employs the limited-memory Broyden–Fletcher–Goldfarb–Shanno method (L-BFGS), which is a quasi-Newton technique suited for large-scale problems with limited computational memory resources.

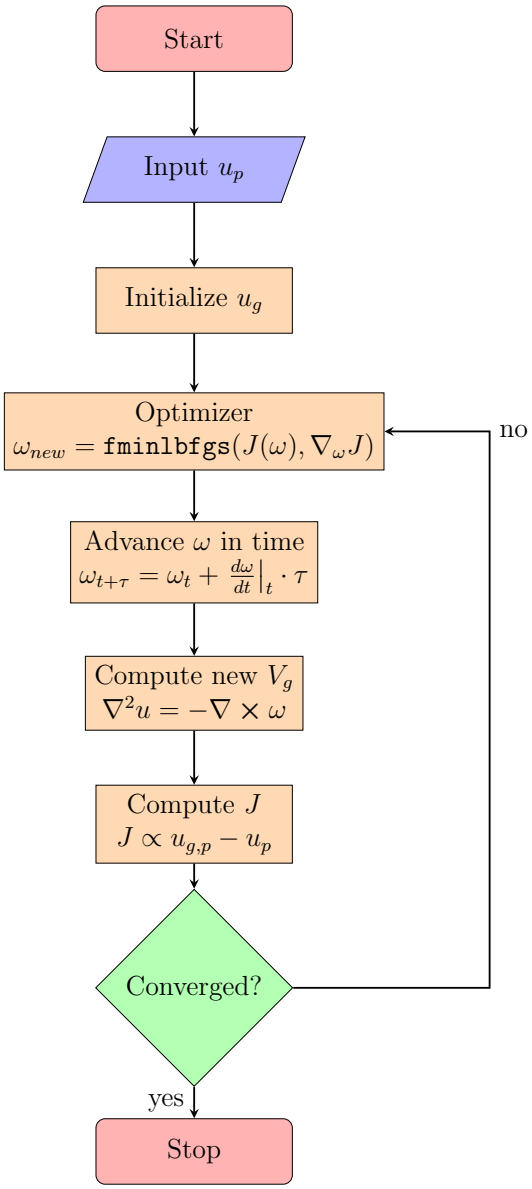

Figure 3.3: Flowchart of VIC-TSA

3.3 Adjoint method for gradient evaluation

A key aspect of the optimization procedure is the evaluation of the gradient of the cost function J with respect with the control variables α_i, indicated as $\nabla_\alpha J$. In this problem, the number of degrees of freedom corresponds to the number of grid points N^3_{edge}, where the RBF coefficients are placed. The adjoint method is instead is able to compute $\nabla_\alpha J$ fast and exactly, solving one additional equation only. In this section, the mathematical foundations of the method will be introduced, following to the application to the VIC-TSA method.

3.3.1 Mathematical formulation of the optimization problem

In mathermatics, the concept of *adjoint* can be understood as a way of 'reversing' the effect of an operator with respect to an inner product space. The notation for it is δ^*, which can be thought as a variation that represents how changes in the output of a system are related back to changes in the input.

The adjoint method revolves around the concept of backward differentiation, which is particularly efficient for functions with a large number of input variables and a single output. In essence, it calculates the gradient of an objective function by first running a forward simulation to compute the function value and then running a backward simulation to compute the gradient. The mathematical elegance of the adjoint method lies in its ability to reverse the chain of computations, tracing the influence of inputs on the output by reversing the flow of differential equations, which is computationally more efficient than traditional forward sensitivity analysis methods. As stated by Giering and Kaminski [1999]:

> *"Adjoint models are tools developed for inverse modeling of physical systems. Inverse modeling is used in various fields of sciences such as geophysics and molecular physics. Among the applications of adjoint models in oceanography and meteorology are* ***data assimilation****, model tuning, sensitivity analysis, and determination of singular vectors (Giering and Kaminski [1999]).*"

In order to fully understand the method and apply it to the VIC-TSA framework, it is useful to describe our minimization problem in mathematical terms:

$$Y = F \cdot X, \tag{3.11}$$

where:

- X represents the control variables, which are the Cartesian values of velocity (or vorticity);
- F is the flow solver plus the linear interpolation;

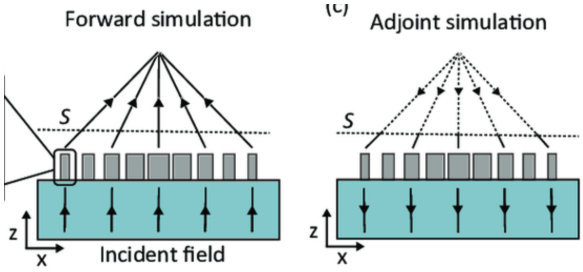

Figure 3.4: Forward and backward problem for adjoint method (Giering and Kaminski [1999]).

- Y is the predicted velocity at the data points.

It is then true that if n is the size of X and m is the size of Y:

$$F : R^n \rightarrow R^m. \tag{3.12}$$

A cost function J can be defined as follows:

$$J = \frac{1}{2} f(Y - D, Y - D), \tag{3.13}$$

that quantifies the reconstruction error comparing with data points. The cost function is defined with the inner product, which yields the squared sum of the reconstruction error at the particle's location. This will also come handy for the following steps. It is then true that:

$$J : R^n \rightarrow R, \tag{3.14}$$

since the cost function yields a scalar.

3.3.2 Calculation of the gradient

Following Giering and Kaminski [1999], the problem is to determine the set of control variables X that minimizes J. Effective minimization algorithms require the gradient $\nabla_X J(X_0)$ of J with respect to the control variables at a given point X_0. For the gradient of the cost function:

$$\nabla_X J : R \rightarrow R^n. \tag{3.15}$$

First, we write the Taylor expansion of J:

$$J(X) = J(X_0) + (\nabla_X J(X_0), X - X_0) + o(|X - X_0|) \tag{3.16}$$

or, in short terms,

$$\delta J = (\nabla_X J(X_0), \delta X). \tag{3.17}$$

In the following, this shorthand notation will be used whenever linear approximations are involved. Suppose F is sufficiently regular; then, for each parameter vector X_0, a variation of Y can be approximated to first order by

$$\delta Y = A(X_0)\delta X, \tag{3.18}$$

where $A(X_0)$ denotes the Jacobian of F at X_0. This is basically a linearization of the model around a state X_0, and is called *tangent-linear* of the model.

Due to the symmetry of the inner product and the product rule, the differentiation of the cost function yields:

$$\delta J = \frac{1}{2}\left(A(X_0)\delta X, F(X_0) - D\right) + \frac{1}{2}\left(F(X_0) - D, A(X_0)\delta X\right) \tag{3.19}$$

$$= \left(F(X_0) - D, A(X_0)\delta X\right). \tag{3.20}$$

Using the definition of the adjoint operator A^*:

$$(v, Aw) = (A^* v, w), \tag{3.21}$$

it is possible to obtain:

$$\delta J = \left(A^*(X_0)(F(X_0) - D), \delta X\right). \tag{3.22}$$

Therefore, according to the definition of the gradient (5), the gradient of the cost function with respect to the control variables is

$$\nabla_X J(X_0) = A^*(X_0)(F(X_0) - D). \tag{3.23}$$

If A represents the *tangent-linear* model, A^* represents the *adjoint* model, which follows the reverse order of differentiation to trace back the influence of the inputs on the outputs. It basically measures the sensitivity of the cost function to changes in Y. The term $F(X_0) - D$ can be seen in fact as a forcing term of the adjoint model. The derivation of the adjoint model for VIC-TSA is analytical, and it will be shown in the next section.

3.3.3 Adjoint equations for VIC-TSA

The adjoint model derived in the previous section can be obtained analytically due to the nature of the VIC-TSA algorithm. In general, if an algorithm has k steps, then the gradient of the cost function can be derived as:

$$\nabla_X J = \sum_{k=1}^{K} \delta_k^* \tag{3.24}$$

This means that each step need to be traced back to derive its adjoint, and then at the end all the adjoint contributions needs to be summed. The process of traveling backward

starts from the generation of the vorticity field, and the time marching and ends with the predicted velocity $u_{g,h}$ through linear interpolation[1].

According to (3.23), in order to evaluate the adjoint model, we travel backwards the steps of the algorithm described in Section 3, formalized as function F of (3.11). The adjoint of each step is denoted as δ^*. We want to calculate the gradient of the cost function with respect to the control variables; this process starts with the *adjoint counterpart of the cost function* : $\delta^* u_{g,p} = 2(u_{g,p} - u_p)$. This first derivation is needed because we are interested in the *sensitivity* of the control variables on J. Then:

1. LI: The gridded velocity $u_{g,p}$ was obtained from u_g with LI, which can be written in matrix form as $u_{g,p} = \mathbf{L}u_g$. The adjoint of LI is just the transpose of the LI matrix, hence $\delta^* u_g = \mathbf{L}^T u_{g,p}$;

2. Velocity was obtained from vorticity with Poisson equation: $\nabla^2 \delta^* u_g = -\tilde{\nabla} \times \delta^* \omega_g$. The Laplacian is self-adjoint, so the existing solver can be used to evaluate the left hand. The adjoint nabla is $\tilde{\nabla} = \left[\frac{\tilde{\partial}}{\partial x}, \frac{\tilde{\partial}}{\partial y}, \frac{\tilde{\partial}}{\partial z}\right]$. Since finite differences were used, the adjoint operator is simply the inverse of these matrices. The final result is $\delta^* \omega_1 = \delta^* \omega_g$.

3. Vorticity was also used in the vorticity transport equation $\frac{D\omega_g}{Dt} = (\omega_g \cdot \tilde{\nabla}) u_g$, so the sensitivity contribution of that step needs to be computed too. The adjoint counterpart of the temporal derivative of the vorticity is:

$$\delta^* \omega_{i,2} = \frac{\partial u_j}{\partial x_i} \delta^* \frac{\partial \omega_j}{\partial t} - \tilde{\delta}\left(u_j^* \delta^* \frac{\partial \omega_i}{\partial t}\right), \tag{3.25}$$

   Which results is $\delta^* \omega_2$.

The gradient of the cost function is then:

$$\frac{\partial J}{\partial \omega_g} = \delta^* \omega_1 + \delta^* \omega_2 \tag{3.26}$$

One might ask why the adjoint of LI is not summed but rather applied to the adjoint variables. The reason is that in the optimization process, the adjoints of differential equations directly contribute to the gradient of the objective function by reflecting the sensitivity of J to changes in the solution variables, summed to capture their collective influence. In contrast, the adjoint of operations like LI (or RBF interpolation) is applied to modify these sensitivities, ensuring that the transformation's impact on the objective function's gradient is accurately represented, rather than being directly summed with the other adjoints.

[1]The modifications needed to include the RBF will be discussed later in this work.

One has to keep in mind that the DoFs are the three components of vorticity, which is a vector field with three components. Hence, the gradient of the vector field is an array of dimensions $(3, N_p)$. The adjoint takes 3-4 times more than the evaluation of the cost function (Giering and Kaminski [1999]), versus the $N_p + 1$ evaluations requested with forward sensitivity methods. In Section 4.5, the addition of the adjoint of the Radial Basis Functions operations will be discussed.

Chapter 4

Radial Basis Functions

This chapter describes the implementation of Radial Basis Functions (RBF) in the VIC-TSA algorithm. As described in the Introduction and the research question, the VIC-TSA method does not perform as well as its predecessor, VIC+, for sequences up to a certain NT, and this is attributed to the use of radial basis functions in the VIC+ algorithm. The validity of this affirmation is further discussed in Section 5.2.2. This chapter discusses the application of RBF, specifically focusing on the enhancements they provide. It establishes the mathematical foundations and delineates the process of their incorporation into the code. The relationship and transition between degrees of freedom and physical values are explained. Lastly, the integration of radial basis functions into the adjoint method is addressed.

4.1 Implementation in VIC-TSA

In Section 3, it was shown how the optimization loop works to fit the best possible velocity field to increase the space resolution of the measurements. The opmizer *fminlbfgs* guesses a vorticity field ω_g, which is time-travelled with the analytical equations and the discrepancy between $u_{g,p}$ and u_p is computed.

The idea behind the use of Radial Basis Functions in the VIC-TSA method is to expand the vorticity field with RBF and optimize the coefficients of this expansion, rather than ω directly (Figure 4.1). Each grid point now represents a point where a basis function with a Gaussian kernel is placed. The choice of the latter will be explained in the next section. More specifically:

1. **Expansion of vorticity field:** The vorticity field ω is expressed as a sum of radial basis functions $\phi_i(r)$, each weighted by a coefficient α_i. Mathematically, this is represented as:
$$\omega = \sum_i \alpha_i \phi_i(r), \quad \text{where} \quad \phi_i(r) = e^{-\frac{r^2}{2\sigma^2}}.$$

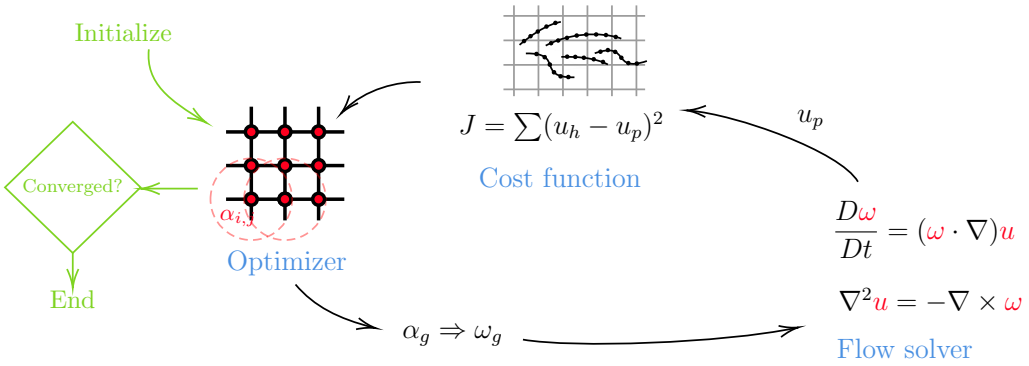

Figure 4.1: Simplified scheme of VIC-TSA with RBF.

Here, r is the radial distance and σ is the spread parameter of the Gaussian RBF.

2. **Optimization for coefficients α_i:** The next step involves optimizing these coefficients α_i so that the reconstructed vorticity field best fits the observed data.

3. **Computation of vorticity from expansion:** Finally, the optimized coefficients are used to compute the vorticity field from the RBF coefficients, which is then utilized in the flow solver.

The choice of using RBF, particularly Gaussian RBF, in this context is expected to offer several advantages:

- *Global support*: the value of the basis function at one point will also influence the surrounding grid points, effectively giving a higher order interpolation method.
- *Stabilization of convergence*: for the aforementioned reasons, the RBF are expected to give VIC-TSA improved robustness to noise, which can help in stabilizing the convergence.
- *Smoothness requirements*: Gaussian Radial Basis Functions (GRBF) are *infinitely smooth*, and their analytical formula can be derived to compute exact derivatives of the quantity represented. Even if the discretization error remains, RBF derivatives are free of truncation error, unlike Finite Differences methods. This property can be used, for instance, to compute the spatial derivatives of the vorticity in the Poisson equation (**??**).

4.2 Gaussian Radial Basis Functions

The RBF kernel chosen for this numerical evaluation is the Gaussian shape $e^{\frac{r^2}{2\sigma^2}}$. Such functions are typically used to construct smooth interpolations from scattered data points.

They are widely used in many other purposes in numerical analysis, like mesh motion algorithms (Lombardi et al. [2013]), FSI problems (Rendall and Allen [2008]), visualization methods in FEM (Xia et al. [2019]), modeling of moving boundary value problems (Vrankar et al. [2007]), and comparative studies with traditional FEM (Loeffler et al. [2018]).

Gaussian RBF are mathematically expressed by the formula:

$$\phi_i(\mathbf{r}) = e^{-\frac{\|\mathbf{r}\|^2}{2\sigma^2}}, \tag{4.1}$$

where $\mathbf{r} = \mathbf{x} - \mathbf{x}_i$ is the radial distance from the function's center $\mathbf{x}_i$, and σ is the spread parameter. They have the following properties:

- *Radial symmetry*: these functions are radially symmetric, meaning their value depends only on the distance from the center, not the direction from it.
- *Smoothness*: GRBF are infinitely differentiable, providing a high degree of smoothness. This property is particularly valuable in applications where continuous and smooth transitions are required.
- *Localization*: This property encapsulates the RBF influence being intensely concentrated around their centers (localization) and diminishing rapidly as one moves away (decay). The parameter σ, typically set to $\frac{1}{4}h$ in VIC-TSA and VIC+ (where h is the grid spacing), governs the scope and intensity of this localized effect, ensuring that each RBF impacts its immediate vicinity while fading rapidly beyond this region. This characteristic is critical for maintaining precise local influences without extensive overlap.
- *Adaptability*: The ability to adjust the centers and scale parameters allows these functions to be adapted to a wide range of data patterns and shapes.
- *Interpolation and approximation*: Gaussian RBF are versatile, capable of exact data fitting (interpolation) or creating a smoothed representation of data (approximation). Their smoothing effect will be one of the monitored behaviors in the numerical test case and especially the experimental assessment.

While Gaussian RBF are advantageous in many aspects, their global support makes them effectively a higher-order interpolation method. This will result in having an interpolation matrix with a larger bandwidth, which will make the computation more precise but slightly slower. The choice of σ can directly affect the computational stability and precision, since a value too large might induce smoothing.

4.2.1 Computing derivatives

Radial Basis Functions, particularly Gaussian RBF, are used not only to interpolate scattered data, but also to approximate derivatives of a vector field. The derivatives of the Gaussian RBF with respect to a spatial coordinate are used for the evaluation of the Poisson equation (**??**). Instead of using Finite Differences, the derivatives of ω can be computed with term-by-term differentiation by deriving the analytical expression of the kernel:

$$\omega = \sum_i \alpha_i \phi_i(r) = \sum_i \alpha_i \phi_i(\|\mathbf{x} - \mathbf{x}_i\|), \tag{4.2}$$

$$\frac{\partial \omega}{\partial x} = \frac{\partial}{dx} \sum_i \alpha_i \phi_i(r) = \sum_i \alpha_i \frac{\partial}{\partial x} \phi_i(x, y). \tag{4.3}$$

This eliminates the truncation error in computing derivatives, as happens with Finite Differences formulations. This makes them ideal for computing spatial derivatives, such as for the vorticity in the Poisson equation. For all the components, these kernel derivatives can be mathematically expressed as:

$$\frac{\partial}{dx}\phi_i(x, y, z) = -\frac{x - x_i}{\sigma^2} \cdot e^{-\frac{(x-x_i)^2+(y-y_i)^2+(z-z_i)^2}{2\sigma^2}}, \tag{4.4}$$

$$\frac{\partial}{dy}\phi_i(x, y, z) = -\frac{y - y_i}{\sigma^2} \cdot e^{-\frac{(x-x_i)^2+(y-y_i)^2+(z-z_i)^2}{2\sigma^2}}, \tag{4.5}$$

$$\frac{\partial}{dz}\phi_i(x, y, z) = -\frac{z - z_i}{\sigma^2} \cdot e^{-\frac{(x-x_i)^2+(y-y_i)^2+(z-z_i)^2}{2\sigma^2}}. \tag{4.6}$$

This derivative retains the Gaussian shape but is scaled and shifted according to the coordinate differences, providing a measure of the rate of change of the function at a point.

The implementation of RBF differentiation is expected to provide more accuracy in the representation of the derivative, because of the aforementioned absence of truncation error and for the global support properties.

4.3 From RBF coefficients to vorticity values

To evaluate a certain value of vorticity at a specific point, the influence of every basis function on that point needs to be evaluated:

$$\omega(\vec{x}_p) = \sum_i \alpha_i \phi_i(|\vec{x}_i - \vec{x}_p|).$$

Not all basis functions have the same influence on that point, because of the Gaussian shape of the kernel that decays with radius. The width of it can be specified with the shape

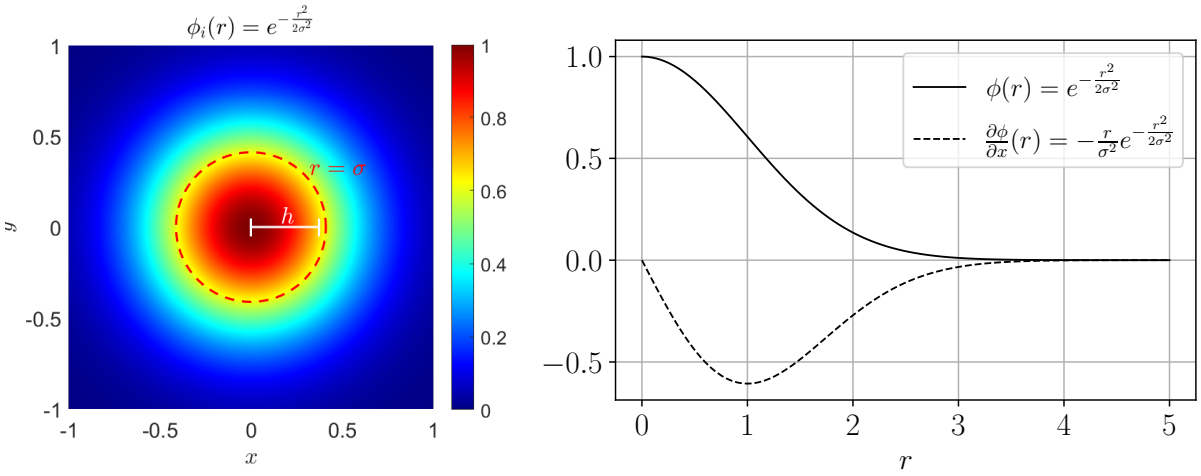

Figure 4.2: Gaussian radial basis function and its derivative.

parameter σ. In general, one would like to encapsulate all the cross distances between the points in a matrix (Euclidean distance matrix) and, for each value of the matrix, compute the RBF value with the kernel (4.5). Once this matrix is set up, it is possible to move from the RBF coefficients α to vorticity values with:

$$\omega = A\alpha. \tag{4.7}$$

The A matrix has dimensions $N \times N$ and can be computed with nested loops, for instance, in 2D:

```
A = sparse(n_interp, n_points);
for i = 1:n_points
    for j = 1:n_points
        dist = sqrt((X(j) - X(i))^2 + (Y(j) - (i))^2);
        A(i, j) = phi(dist);
```

A more efficient approach by leveraging vectorization is:

```
DX = X_interp(:) - X(:)';  DY = ...;  DZ = ...;
D = DX.^2 + DY.^2 + DZ.^2;
A = exp(-D / (2 * sigma^2));
```

and for the derivatives, by using the analytical expression for the kernel (4.4):

```
dA_dx = -(DX / sigma^2) .* exp(-D / (2 * sigma^2));
dA_dy = -(DY / sigma^2) .* exp(-D / (2 * sigma^2));
dA_dz = -(DZ / sigma^2) .* exp(-D / (2 * sigma^2));
```

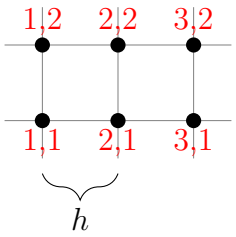

Figure 4.3: Grid spacing and lexicographic ordering of the unknowns.

Example in 2D For a support radius of 1.1 * `grid_h` and the following grid:

$$\begin{bmatrix} \omega_{1,1} \\ \omega_{2,1} \\ \omega_{3,1} \\ \omega_{1,2} \\ \omega_{2,2} \\ \omega_{3,2} \end{bmatrix} = \begin{bmatrix} \phi(0) & \phi(h) & \phi(2h) & \phi(h) & \phi(h\sqrt{2}) & \phi(h\sqrt{5}) \\ \phi(h) & \phi(0) & \phi(h) & \phi(h\sqrt{2}) & \phi(h) & \phi(h\sqrt{2}) \\ \phi(2h) & \phi(h) & \phi(0) & \phi(h\sqrt{5}) & \phi(h\sqrt{2}) & \phi(h) \\ \phi(h) & \phi(h\sqrt{2}) & \phi(h\sqrt{5}) & \phi(0) & \phi(h) & \phi(2h) \\ \phi(h\sqrt{2}) & \phi(h) & \phi(h\sqrt{2}) & \phi(h) & \phi(0) & \phi(h) \\ \phi(h\sqrt{5}) & \phi(h\sqrt{2}) & \phi(h) & \phi(2h) & \phi(h) & \phi(0) \end{bmatrix} \begin{bmatrix} \alpha_{1,1} \\ \alpha_{2,1} \\ \alpha_{3,1} \\ \alpha_{1,2} \\ \alpha_{2,2} \\ \alpha_{3,2} \end{bmatrix}, \tag{4.8}$$

where the red colored values are the ones within σ. Below, a color-coded plot shows that the points that are further away from the domain are indeed associated with a lower RBF value.

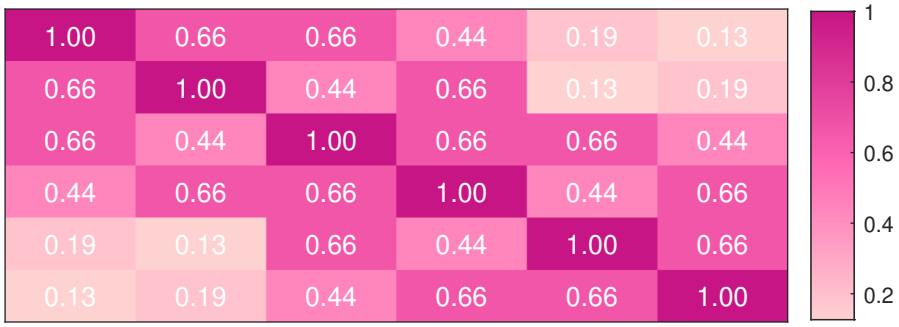

Figure 4.4: A matrix, with explicit RBF value for all the distances between the points.

4.3.1 Test case description

In this section, a simple test case is set up, which involves the implementation of Radial Basis Functions (RBF) for the approximation of a scalar field and its derivative. The test

case is structured to evaluate the performance of RBF in interpolating a known function and its spatial derivative.

Initialization and grid setup The test case is defined within a cubic domain with edge length 2π. The grid is uniformly spaced with a grid spacing of half the typical length scale ($0.5 \times 0.17 \times \pi$). The RBF spread parameter σ is set to 1.1 times the grid spacing to ensure adequate coverage of the domain by the basis functions; this follows the previous work of Schneiders and Scarano [2016] on the implementation of RBF in VIC+. The setup is defined in MATLAB as follows:

```
L = pi;
grid_h = 0.1 * L;
sigma = 1.1 * grid_h;

[X, Y, Z] = meshgrid(-L:grid_h:L, -L:grid_h:L, -L:grid_h:L);
n_points = numel(X);
```

Scalar field and its derivative The scalar field ω to be fitted is defined as $\omega = \cos(X) \cdot \cos(Y) \cdot \cos(Z)$. The derivative of this field with respect to x, denoted as $\frac{d\omega}{dx}$, is analytically given by $-\sin(X) \cdot \cos(Y) \cdot \cos(Z)$. The MATLAB implementation is:

```
w_to_fit = cos(X) .* cos(Y) .* cos(Z);
dw_to_fit = -sin(X) .* cos(Y) .* cos(Z);
```

RBF implementation and derivative computation The Euclidean distance matrix and its derivatives are computed to set up the RBF system. The MATLAB code snippet for this process is as follows:

```
DX = X(:) - X(:)';
DY = Y(:) - Y(:)';
DZ = Z(:) - Z(:)';
D = DX.^2 + DY.^2 + DZ.^2;

A = exp(-D / (2 * sigma^2));
dA_dx = -(DX / sigma^2) .* exp(-D / (2 * sigma^2));
```

Reconstruction of scalar field and its derivative Finally, the RBF coefficients are computed and used to reconstruct the scalar field ω and its derivative $\frac{d\omega}{dx}$. The reconstruction is carried out as follows:

```
RBF_coeffs = A \ w_to_fit(:);
w = A * RBF_coeffs;
```

```
dw_dx = dA_dx * RBF_coeffs;

w = reshape(w, size(X));
dw_dx = reshape(dw_dx, size(X));
```

This test case demonstrates the capability of RBF in approximating both a scalar field and its spatial derivative within a defined domain (Figure 4.5). All of these approaches exhibit a N^2 convergence, where N is the total number of points in the domain. The following section describes a faster method that makes use of the Fast Fourier Transform (FFT).

4.4 RBF evaluation with FFT

The method proposed in Abe and Iiguni [2006] is able to execute the same task, without differentiation for now, with $N \cdot \log(N)$ convergence, compared to the N^2 of the Euclidean distance matrix-based approach. The operation in FFT domain is:

$$\mathrm{DFT}[y_n[k]] = \frac{1}{d_k}\mathrm{DFT}[c_l^p][k] \tag{4.9}$$

$$c_l^p = \mathrm{IDFT}\left[\frac{1}{d_k}\mathrm{DFT}[y_n[k]][l]\right] \tag{4.10}$$

$$c = Tc_p \tag{4.11}$$

$$(T)_{ij} = \begin{cases} 0 & \text{if } |(G^{-1}G_p)_{ij}| \leq \rho, \\ (G^{-1}G_p)_{ij} & \text{otherwise} \end{cases} \tag{4.12}$$

For instance, in VIC+, a formula similar to (4.10) was used:

```
y = ifftn( TFFT .* fftn(RBFcoeff_padded) ),
```
(4.13)

$$y_n = \mathrm{IDFT}\left[d_k\mathrm{DFT}[c_p][k]\right] \tag{4.14}$$

The code with FFT runs about 30 times faster than the code with the Euclidean distance matrix approach.

The use of FFT in the context of RBF is a powerful technique due to the convolution theorem, which states that the Fourier transform of a convolution is the pointwise product of their Fourier transforms. In the spatial domain, we often deal with convolutions, especially when working with filters or any operation that involves the overlap of functions across a domain. The FFT method transforms the convolution operation into a multiplication in the frequency domain, which is significantly faster, particularly for large datasets. FFT-based methods maintain a high level of accuracy, and also with the Discrete-FTT the error in moving from α_i to ω_i is low (Abe and Iiguni [2006]).

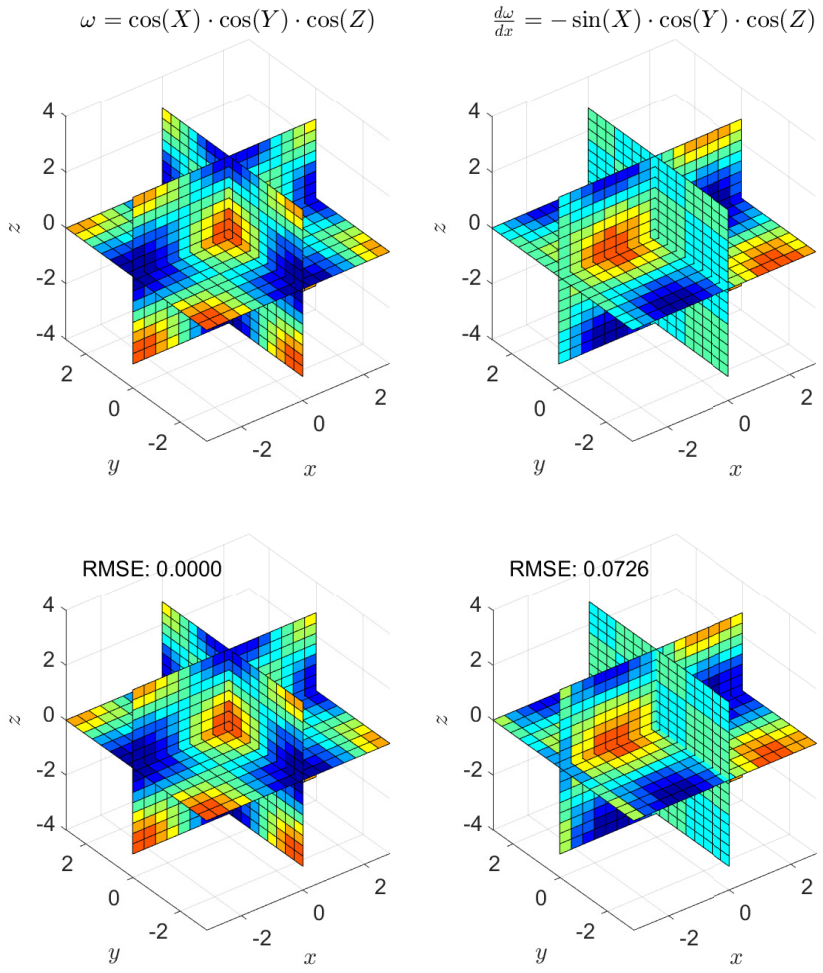

Figure 4.5: Testcase of RBF interpolation and derivative computation. Ground thruth above and reconstruction with interpolation error below.

Application of FFT to RBF in VIC-TSA The enhancement of spatial resolution in the VIC-TSA algorithm is achieved by leveraging the convolution of the RBF coefficients with the RBF kernel. This process is translated into the frequency domain to utilize the FFT for efficient computation.

An important aspect of the FFT approach in the VIC-TSA algorithm is the construction of the transformation matrix $TFFT$, which encapsulates the convolution operation of the RBF coefficients in the spatial domain.

```
function TFFT = calcTFFT_TSA(sig,X,Y,Z)
    [ny, nx, nz] = size(X);
    t = exp( - (1/2/sig^2) * ((X(:) - X(1)).^2 + (Y(:) - Y(1)) ...
    t = reshape(t, ny, nx, nz);
```

```
    T = zeros(2*ny+1, 2*nx+1, 2*nz+1);
    % ... (Rest of the code populating the T matrix)
    TFFT = fftn(T(1:end-1, 1:end-1, 1:end-1));
end
```

This function computes the FFT of the matrix T, which contains the spatial influence values of a single RBF (note the `X(1)`) over the entire domain. The calculation takes advantage of the symmetry and periodicity of RBF to construct $TFFT$ efficiently. To evaulate then the coefficients:

```
function w = calcUfromRBF_TSA(TFFT, RBF_coeffs)
    RBFcoeff_padded = % ... pad RBF coefficients
    wx = ifftn( TFFT .* fftn(RBFcoeff_padded) );
    % ... same for other 2 components
```

Velocity field reconstruction The velocity field is reconstructed by applying the transformation matrix $TFFT$ to the RBF coefficients. The process is outlined in the following code snippet:

```
% Compute omega with FFT
tic
TFFT = calcTFFT_TSA(support_radius, X, Y, Z);
RBF_coeffs = calcRBFcoeff_TSA(TFFT, w_to_fit);
w = calcUfromRBF_TSA(TFFT, RBF_coeffs);
wx = reshape(w(:,1), size(X));
toc
```

The velocity field w is obtained by reshaping the result to match the spatial dimensions. This method ensures that the spatial super-resolution of the velocity field is realized with computational efficiency, even though implementing the RBF differentiation is more challenging, for this reason, when the RBF derivatives are being used, the EDM method is applied. The FFT method becomes significantly preferable to the EDM approach when the grid is $\approx 40x40x40$. Future work might focus on refining the derivative computation and fully integrating the FFT-based RBF method into the VIC-TSA framework to enhance its applicability to a wider range of fluid dynamics situations, for instance experiments with a large number of grid points in the measurement volume.

4.5 Modification to the adjoint procedure

In 3.3, the adjoint procedure was introduced for a fast and exact calculation of $\nabla_X J$, the gradient of the cost function with respect to the control variables. This procedure follows the steps in reverse order from the final result of an optimization loop, the cost function

J, to the control variables ω_g. It was stated that if an algorithm has k analytical steps, the adjoint of each one needs to be computed:

1. (LI) to obtain $u_{g,p} = \mathbf{L}u_g$; $\delta^* u_g = \mathbf{L}^T u_{g,p}$.
2. Poisson equation: $\nabla^2 \delta^* u_g = -\tilde{\nabla} \times \delta^* \omega_g$. The adjoint gradient $\tilde{\nabla}$ leads to $\delta^* \omega_1 = \delta^* \omega_g$.
3. Vorticity transport equation gives: $\delta^* \omega_{i,2} = \frac{\partial u_j}{\partial x_i} \delta^* \frac{\partial \omega_j}{\partial t} - \tilde{\delta} \left(u_j^* \delta^* \frac{\partial \omega_i}{\partial t} \right)$, resulting in $\delta^* \omega_2$.

The radial basis function evaluation can be represented as a matrix multiplication, where the resulting vector ω is obtained by multiplying the matrix $\mathbf{\Phi}$ with the weight vector α. In this equation, $\mathbf{\Phi}$ contains the values of the radial basis function at each grid point, and $\mathbf{w}$ represents the weights. The adjoint equation corresponding to this calculation is expressed as:

$$\delta^* \omega_1 = \mathbf{\Phi}^T \delta^* \omega. \tag{4.15}$$

This computing method is applicable to both the Euclidean distance matrix approach and the FFT approach. In the first case, $\mathbf{\Phi}$ would be represented by matrix A, while in the second case by `TFFT`, as described earlier in this chapter. Furthermore, to make the code compatible with the introduction of RBF operations, such as the spatial derivatives of ω with RBF, the same adjoint code can be used by converting the DoFs, which are the RBF coefficients α, to their respective values ω. As a conceptual implementation:

```
function [J, gradJ] = VIC_TSA_optimization_func(DoF)

    if opts.rbf.userbf == 1
        xi_init = calc_vort_from_RBF(PHI_matrix, DoF);
    else
        xi_init = DoF;
    end

        [u_fw, OUT_fw] = VICforward(xi_init);  % travel forward
        [J_fw, OUT_fw] = calcJ(u_fw, OUT_fw);
        gradJ_fw       = gradJ_adjoint(OUT_fw);

        % same for backward (bw)

        J = J_fw + J_bw;

        gradJ = gradJ_fw + gradJ_bw;

    if opts.rbf.userbf == 1
        gradJ = calc_vort_from_RBF_TSA(PHI_matrix, gradJ);
    end
end
```

Chapter 5

Numerical Assessment

The numerical assessment of the reconstruction technique consists on the evaluation of the reconstruction of a synthetic vortex field, which is described by the Taylor-Green sine wave lattice Taylor and Green [1937]. The purpose of this artificial tracer generator is to provide the same output of the Shake-The-Box algorithm (Schanz et al. [2016]) to the VIC-TSA code. A random set of tracers is generated in a simulated measurement volume and are time-advanced using a Runge Kutta 4-5 method. This simulates the measurement data produced by a PTV experiment with variable seeding density. The assessment is done by comparing the reconstructed value of velocity magnitude with the ground thruth flow, provided by the analytical expressions. Particular attention is given to the modulation of the peak value of the sinusoidal waves.

Subsequent sections provide background on the complexities of reconstruction method assessments, including the analytical expression of the Taylor-Green vortex lattice and relevant concepts like amplitude modulation, time marching, and nondimensional parameters. The discussion highlights the importance of consistent tracer density for accurate simulation and outlines the criteria for comparing different reconstruction techniques. Additionally, it touches on mesh convergence and the robustness of the reconstruction method in the presence of noise, offering a concise overview of the technical and methodological foundations underlying the reconstruction analysis.

5.1 Assessment of reconstruction methods

The assessment of reconstruction methods for PIV is not an easy task, due to the lack of generality of a common ground test case. Such methods are very different in the way they apply the reconstruction and in their architecture, hence it is difficult to predict a well-established procedure that can assess all of them. It should also be mentioned that experimental assessments do not have a ground-thuth by definition, and numerical evaluations do not fully encapsulate the challenges encountered in experimental settings,

including uncertainties and errors.

Space-super resolution methods use the available time information to enhance space resolution, but, for instance, while VIC+ (Schneiders and Scarano [2016]) uses only a single time frame and the additional time information is provided by the material derivative, VIC-TSA leverages the information provided by the other time frames. This means that the tracers need to be generated and time-marched, which can introduce an additional truncation error. The situation becomes even more complicated if the object of assessment is the unsteady reconstruction capabilities: in the literature there are some assessments available like the turbulent boundary layer, which can be both experimental (Schneiders and Scarano [2016]) or from a Direct Numerical Simulaition (DNS) (Wang et al. [2022]) and jet flow (Schneiders and Scarano [2016], Schneiders et al. [2014]), but the quality of the reconstruction is usually evaluated visually or statistically, for instance, by reconstruction of the turbulence length scales. For instance, Wang et al. [2022] shows in the experimental assessment the flow over a hemisphere reconstructed from a PTV experiment, and compares it to a DNS simulation, to visually assess the general shape of the flowfield. In general, such test cases do not yield quantitative information like an analytical test case, and in literature there is still no such thing as a clear and common methodology.

Sine-wave reconstruction Sine-based velocity distributions have been widely used to test PIV reconstruction methods, both in 2D (Willert and Gharib [1991], Scarano and Riethmuller [2000]) and in 3D (Kähler et al. [2016], Scarano et al. [2022]). In this work, the reconstruction is fully tridimensional. The examination focuses on reconstructing the sinusoid, particularly considering the modulation of the peak value, as the seeding concentration is progressively reduced. This means that the quality of the reconstruction will deteriorate, but the performance at a lower seeding concentration is where the differences are most evident. An analytical test case allows controlling variables such as particle density and sampling time to validate and verify the reconstruction methods. At a lower seeding concentration, the influence of the governing equation (which provides additional time information and physical constraints) is expected to produce a more uniform and accurate reconstruction, especially at a lower seeding density.

5.1.1 Taylor-Green vortex lattice

In fluid dynamics, the Taylor–Green flow represents a decaying vortex, which is an unsteady flow pattern and has an explicit solution of the incompressible Navier–Stokes equations in Cartesian coordinates. It is named after the two mathematicians who have studied it for the first time (Taylor and Green [1937]). In this case, the steady version is used since the evaluation is steady. It is composed of three velocity components, which are described by

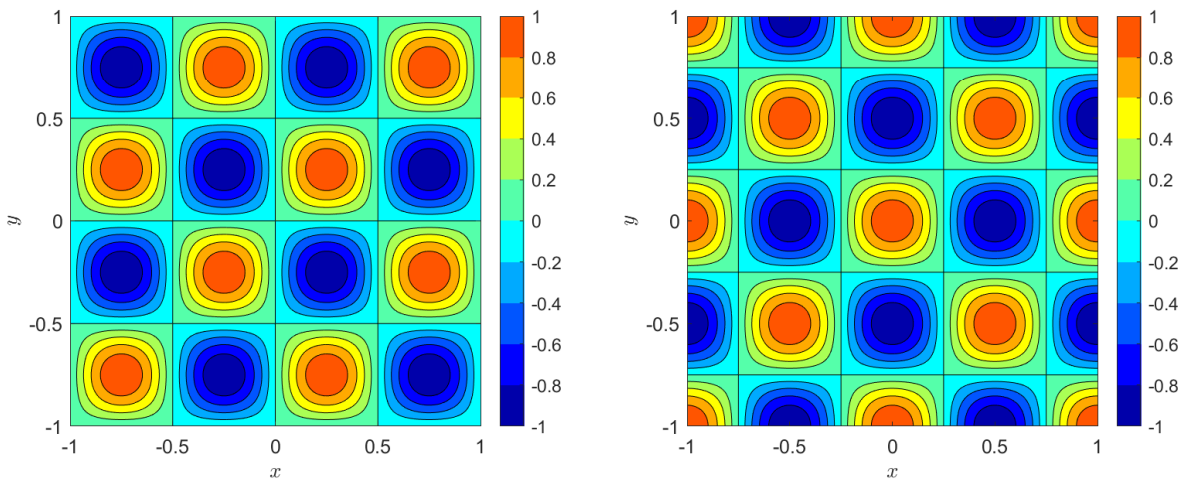

(a) $u(x, y)$ (b) $v(x, y)$

Figure 5.1: Taylor Green vortex lattice.

the following expressions:

$$\begin{cases} u(x,y) = A \sin\left(\dfrac{2\pi x}{\lambda}\right) \sin\left(\dfrac{2\pi y}{\lambda}\right) \\ v(x,y) = A \cos\left(\dfrac{2\pi x}{\lambda}\right) \cos\left(\dfrac{2\pi y}{\lambda}\right) \\ w = A \end{cases} \tag{5.1}$$

where A is the amplitude of the sine and cosine waves, and λ the wavelenght. In this work, these quantities are set to unity, for ease of implementation and intuition. In any case, non-dimensional coefficients will be used that link the seeding concentration to the wavelength and the amplitude. The flow field is independent of the vertical coordinate z, and the $z-$ velocity component is constant throughout the domain. This means that the flow rotates around the $z-$axis and travels in this direction with constant speed. The flow pattern produced is shown in Figure 5.1. The $u(x, y)$ and $v(x, y)$ alternate with a period dictated by the wavelenght λ, inducing a in-plane rotation on the $xy-$plane. This rotational motion is overimposed with the constant $z-$velocity, producing an array of parallel vortices.

To simulate the output of the Shake-The-Box algorithm, the velocity and material derivative of the velocity of each particle must be evaluated in multiple time acquisitions. The material derivative can be calculated analytically. The gradient of the vector field $\tilde{\mathbf{u}} = (u, v, w)$ is a matrix with all the first-order partial derivatives of the vector components.

The gradient of the velocity is given by:

$$\nabla \vec{u} = \begin{bmatrix} \frac{\partial u}{\partial x} & \frac{\partial u}{\partial y} & \frac{\partial u}{\partial z} \\ \frac{\partial v}{\partial x} & \frac{\partial v}{\partial y} & \frac{\partial v}{\partial z} \\ \frac{\partial w}{\partial x} & \frac{\partial w}{\partial y} & \frac{\partial w}{\partial z} \end{bmatrix} \tag{5.2}$$

Calculating these partial derivatives yields:

$$\nabla \vec{u} = \begin{bmatrix} A\cos\left(\frac{2\pi x}{\lambda}\right)\sin\left(\frac{2\pi y}{\lambda}\right)\cdot\frac{2\pi}{\lambda} & A\sin\left(\frac{2\pi x}{\lambda}\right)\cos\left(\frac{2\pi y}{\lambda}\right)\cdot\frac{2\pi}{\lambda} & 0 \\ -A\sin\left(\frac{2\pi x}{\lambda}\right)\cos\left(\frac{2\pi y}{\lambda}\right)\cdot\frac{2\pi}{\lambda} & -A\cos\left(\frac{2\pi x}{\lambda}\right)\sin\left(\frac{2\pi y}{\lambda}\right)\cdot\frac{2\pi}{\lambda} & 0 \\ 0 & 0 & 0 \end{bmatrix} \tag{5.3}$$

This matrix represents the rate of change of the vector field components in each direction. The material derivative can now be computed as:

$$\frac{D\vec{u}}{Dt} = \frac{\partial \vec{u}}{\partial t} + \vec{u}\cdot\nabla\vec{u} = \vec{u}\cdot\nabla\vec{u}, \tag{5.4}$$

since the flowfield is steady. Substituting the expression for the gradient yields:

$$\frac{D\vec{u}}{Dt} = \left[-\frac{A^2\pi}{\lambda}\cos\left(\frac{4\pi y}{\lambda}\right)\sin\left(\frac{4\pi x}{\lambda}\right),\ -\frac{A^2\pi}{\lambda}\cos\left(\frac{4\pi x}{\lambda}\right)\sin\left(\frac{4\pi y}{\lambda}\right),\ 0 \right] \tag{5.5}$$

5.1.2 Tracer tracking

Tracer generation Once the flow domain has been enstablished, a random set of particle is generated with Matlab's `rand` function, with a uniform distribution in the domain. It is good practice to include additional padding volume with respect to the flow domain that needs to be reconstructed, in order to avoid boundary effects. For example, Figure 5.2 shows that lack of padding may lead to regions with less seeding density, because some tracers in the highlighted region will leave the domain. Including a padding volume, instead, ensures that the seeding density is manteined constant thoughout the simulated measurement volume. The output of this operation are the coordinate arrays, X_p, Y_p and Z_p, of length N.

Time marching For time marching, an explicit fourth-order Runge-Kutta scheme has been used. After the particles have been generated, they can be time-marched on the domain according to the magnitude of the velocity components at the tracer's location.

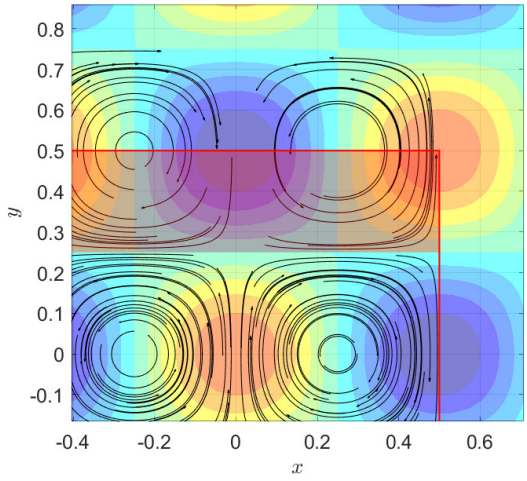

Figure 5.2: Tracer particles leaving the domain of interest, reducing the seeding density in the highlighted area. On the background: $v(x, y)$ velocity component.

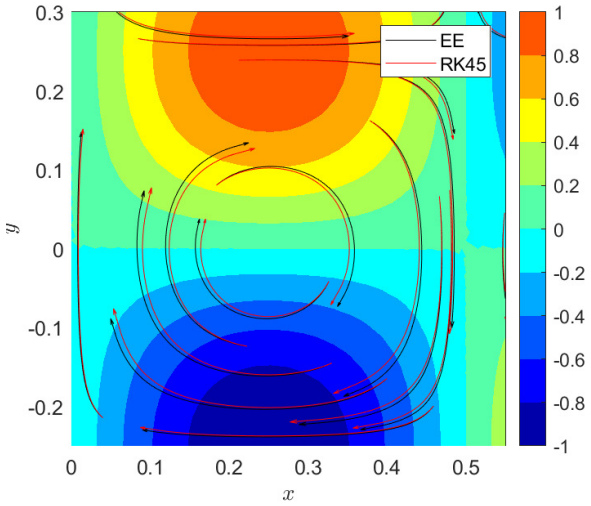

Figure 5.3: RK45 vs Euler time tracking method.

Integrating for the whole time segment $\mathcal{T}$ yields the particle track. The particle motions can be formulated by the following set of ODEs:

$$\frac{d\mathbf{x}}{dt} = \mathbf{U}(\mathbf{x}) \tag{5.6}$$

where $\mathbf{x} = (x, y, z)$ and $\mathbf{U}(\mathbf{x}) = (U(x, y), V(x, y), W)$. These can be discretized for time marching in a Forward Euler fashion as:

$$\mathbf{x}_{t+1} = \mathbf{x}_t + \Delta t \cdot \mathbf{U}(\mathbf{x}_t) \tag{5.7}$$

For the RK4 method, the update for each variable over a timestep Δt from t_n to t_{n+1} would be:

$$\mathbf{x}_{n+1} = \mathbf{x}_n + \frac{\Delta t}{6}(\mathbf{k}_1 + 2\mathbf{k}_2 + 2\mathbf{k}_3 + \mathbf{k}_4) \tag{5.8}$$

where each $\mathbf{k}_i$ for $i = 1, 2, 3, 4$ is a vector function representing the RK4 increments, calculated similarly to the single variable case, but using the functions $U(x, y), V(x, y)$, and W for the respective variables. RK45 is a combination of RK4 and RK5, allowing for adaptive step size control. It automatically adjusts the step size during integration to balance accuracy and computational efficiency. The implementation of the method in the `Matlab`'s function `ode45` allows for the user to specify the time step at which the solution needs to be returned, while the time integration is carried out with automatic selection by `ode45`, which ensures stabilty and accuracy. This permits to vary the simulated tracer sampling frequency without worrying about the time integration.

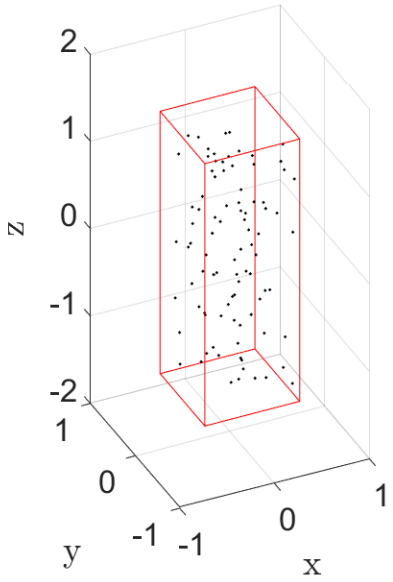

Figure 5.4: Generated tracers

During the time marching in the reconstruction process, some particles may move upward in the positive $z-$direction and eventually leave the domain. To maintain a consistent tracer density within the domain of interest, these particles are replaced by generating new particles within a padding volume. This approach ensures a continuous presence of particles in the domain, as shown in Figure 5.4, where the selected time segment allows the movement of the particles upward without leaving empty regions. The method of generating particles with a padding volume was chosen for its straightforward implementation with the `ode45` function, facilitating the management of particle positions during each iteration of the time integration procedure.

Numerical implementation The analytical formulas described in (5.1) and (5.5) can be efficiently implemented in Matlab using symbolic manipulation:

```
syms x y z
u = A * sin(2*pi*x/lambda) * sin(2*pi*y/lambda);
v = A * cos(2*pi*x/lambda) * cos(2*pi*y/lambda);
w = A;
U = [u,v,w];.
gradU = [[diff(u,x) diff(u,y) diff(u,z)]
         [diff(v,x) diff(v,y) diff(v,z)]
         [diff(w,x) diff(w,y) diff(w,z)]];
DuDt = U * gradU
```

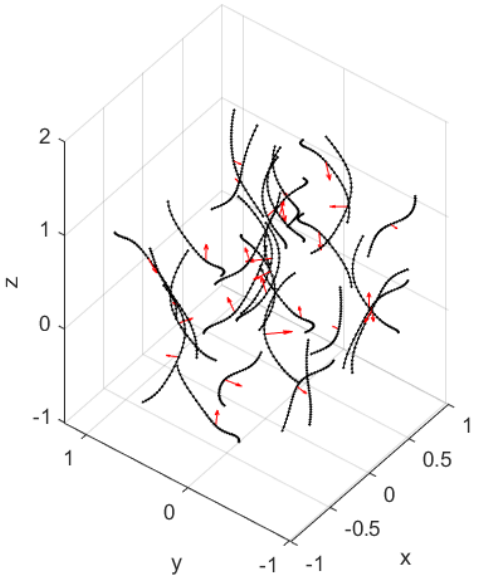

Figure 5.5: Material derivative.

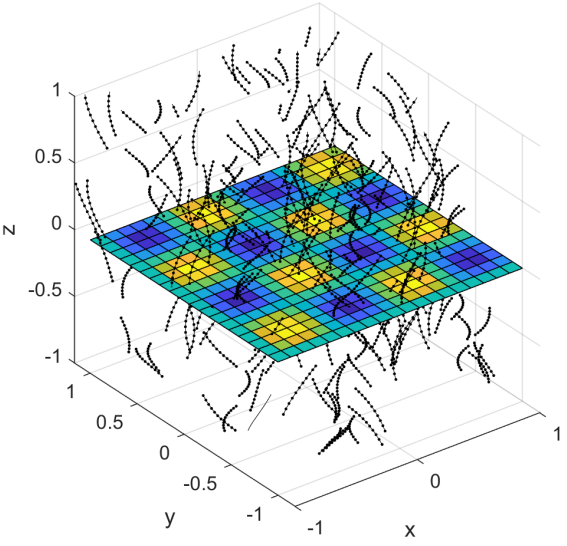

Figure 5.6: Artificial tracers, slice of the $u(x, y)$ component

The output is in Figure 5.5, where it is shown that the material derivative points correctly at the direction of the acceleration: The equations of motions are defined in the following way:

```
function dXdt = vel(t, X, u, v, w)
    dXdt = zeros(3,1);
    dXdt(1) = u(X(1),X(2));
    dXdt(2) = v(X(1),X(2));
    dXdt(3) = w;
end
```

which are then time integrated with the Runge-Kutta 4 method:

```
tspan = 0:dt:T;
for i = 1:numTracers
    X0_i = X0(i,:);   % vector of init. pos. of the tracer
    [t, X_out] = ode45(@(t,X) vel(t,X,u,v,w), tspan, X0_i);
end
```

At each time step, $\vec{u} = [u, v, w]$ and $\dfrac{D\vec{u}}{Dt} = \left[\dfrac{Du}{Dt}, \dfrac{Dv}{Dt}, \dfrac{Dw}{Dt}\right]$ can be computed at each particle location with the formulas described in Section 5.1.1. These quantities will only depend on the x and y coordinates as previously explained.

The purpose of the tracer generator is to provide an output file of the same type as the

output of Shake-The-Box, so that there are no differences between the reconstruction of synthetic or experimental data. The format is shown in Table 5.1 and is assembled after time marching.

5.1.3 Metrics and comparisons

This section explains the non-dimensional parameters considered for the numerical assessment of the VIC-TSA reconstruction method. The reconstruction applied to the simulated tracers is compared with the analytical velocity distribution (5.1). Particular attention is given to the modulation of the peak values of the sine waves, and either the u or v velocity components can be used for the evaluation. Hence, the parameters used for the evaluation are the amplitude of the reconstructed wave, the average interparticle distance and the time segment, made non-dimensional using:

- the convective velocity A, which is amplitude of the waves and velocity in $z-$direction;
- the wavelenght λ;
- the average interparticle distance r^* between the tracers, which is an indication of their concentration. For a uniform distribution in a 3D volume, it can be computed with Wigner–Seitz radius:

$$\overline{r} = \sqrt[3]{\frac{3}{4\pi C}} \ , \tag{5.9}$$

  with C being the seeding concentration expressed in $C = N_{\text{part}}/V$. There are also other ways to compute it, but this formulation is chosen in order to be consistent with Scarano et al. [2022].

All of these parameters have been set to unity for ease of interpretation. The nondimensionalization allows for comparison with Scarano et al. [2022] even if different values of U_{conv}, λ and $\mathcal{T}$ have been used by the authors. The metrics used for the evaluation are:

x (mm)	y (mm)	z (mm)	u (m/s)	v (m/s)	w (m/s)	$\lvert V \rvert$ (m/s)	I	Time Step	Track ID	ax (m/s²)	ay (m/s²)	az (m/s²)	$\lvert a \rvert$ (m/s²)
-0.424	0.300	0.105	-0.438	0.277	1.000	1.126	-	1	1	2.572	1.862	0.000	3.175
0.280	0.439	-0.549	0.367	0.173	1.000	1.079	-	1	2	-1.154	2.176	0.000	2.463
-0.062	-0.459	0.711	0.095	-0.896	1.000	1.346	-	1	3	-2.196	-1.536	0.000	2.679
0.223	0.376	-1.019	0.694	-0.118	1.000	1.223	-	1	4	1.028	3.141	0.000	3.304
⋮	⋮	⋮	⋮	⋮	⋮	⋮	⋮	⋮	⋮	⋮	⋮	⋮	⋮
-0.296	-0.002	0.924	0.011	-0.284	1.000	0.000	-	19	1	1.708	0.073	0.000	3.175
0.125	0.197	1.529	0.669	0.233	1.000	0.000	-	19	2	3.142	-1.956	0.000	2.463
0.457	0.457	0.501	0.071	0.929	1.000	0.000	-	19	3	-1.608	1.627	0.000	2.679
-0.361	0.571	-0.447	0.330	0.578	1.000	0.000	-	19	4	3.090	-2.440	0.000	3.555

Table 5.1: DaVis Particle Track Data Sample

- *Amplitude modulation* u^*. The amplitude modulation is defined as

$$u^* = \frac{u}{A}, \tag{5.10}$$

where u is the reconstructed value of the Taylor-Green vortex lattice at the peak of the wave; A is the amplitude of the waves. The value of u^* ranges from 0 to 1[1], which is an indication of the *quality of reconstruction*.

- *Average interparticle distance* r^*. This quantity is made nondimensional with the wavelenght:

$$r^* = \frac{\bar{r}}{\lambda} \tag{5.11}$$

- *Assimilated time segment* t^*. The nondimensional time is defined as:

$$t^* = \frac{U_{conv}\mathcal{T}}{\bar{r}} = \frac{A\mathcal{T}}{\bar{r}}, \tag{5.12}$$

as A is assumed as convective velocity of the entire flowfield. These metrics give an indication of the track regime, as explained in chapter 3. For instance, the adjacent tracks regime is characterized by $t^* = 1$.

- *Moving average*. One of the metrics used to compare the performance of the different algorithms is the moving average, which will be plotted as a baseline for the amplitude modulation analysis. From the theory of linear filters, the moving average is a filter that creates an average of values close to a specific location in a data set. This filter is often employed to smooth out a dataset by shifting the center value across the entire data sequence, hence the name *moving average*.

  In this case, the moving average is applied by centering a squared interrogation window on the peak values of the synthetic lattice vortex Figure 5.1, either the $u-$component or the $v-$component. This yields an average value of the velocity component in that interrogation window. The process is repeated while increasing the dimension of the window size, which is expected to smooth out the value of the peak and introduce amplitude modulation.

  The computation can be carried out analytically, since the expressions for u and v for the synthetic lattice vortex are known (5.1). The average value over the interrogation window (IW) can be computed as:

$$u_{\text{mean}} = \frac{\iint_{IW} v(x,y)\,dxdy}{\iint_{IW} dxdy} = \frac{\int_{-l/2}^{l/2}\int_{-l/2}^{l/2} v(x,y)\,dxdy}{S_{IW}}, \tag{5.13}$$

[1]Or slighlty above, since the method can sometimes overshoot.

where S_{IW} is the area of the interrogation window. This can be proven to be equal to the $sinc^2$ function.

- *Linear interpolation*. It is a method to estimate the values between two known points in a straight-line fashion. When dealing with 3D interpolation of sparse data, this concept extends to three dimensions. Trilinear interpolation, for example, is used to estimate values within a 3D space with sparse data by considering the nearest data points. It is a simple but reliable technique that is often used in fields such as computer graphics and fluid dynamics.

An example of the amplitude modulation plot is given in Figure 5.7. It is obtained by comparing the reconstruction of the peaks with the analytical value. The grid spacing is chosen so that there will always be a grid point where the amplitude of the sine wave lattice is maximum, equal to 1, as shown by Figure 5.8; in this way there is no need to interpolate, and the value of the reconstructed field at that point can be probed from the grid. This operation is performed for increasing values of r^*, up to the point where the interparticle distance is almost half the wavelength.

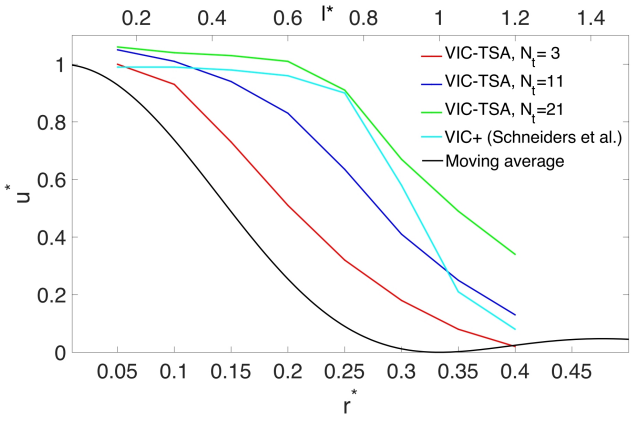

Figure 5.7: Example of $u^* - r^*$ plot.

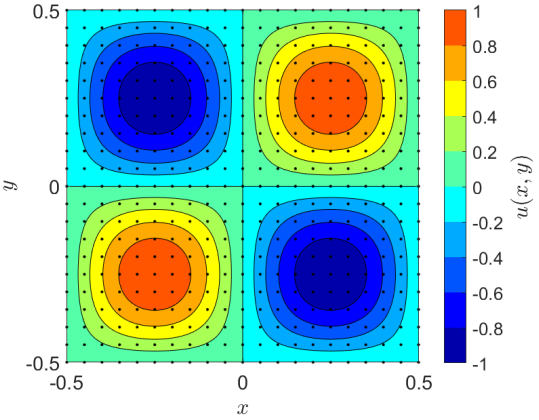

Figure 5.8: Ground thruth flow, with a grid point covering each peak.

The moving average filter is plotted as a baseline. It is a good representation of what could be obtained with the classic PIV approach based on the interrogation window and the cross-correlation. In this case, the measurement domain is divided into interrogation windows (or volumes in 3D PIV), where every volume contains a few numbers of particles. Then, the cross-correlation analysis is applied to each interrogation window to find the average movement of the particles. In this way, the velocity field can be obtained easily, but the small-scale dynamics of the single particles will be lost. The moving average

effectively acts as a low-pass filter, cutting out the smallest scales of motion to obtain the average movement of the group of particles. In contrast, with 3D PTV every particle is tracked singularly, hence giving more space (and time) resolution. It is expected then that every reconstruction method that starts from time-resolved 3D PTV data, even linear interpolation, should perform better than the moving average. It is not always so obvious, as sometimes in real experiments the seeding concentration needs to be reduced for Shake-The-Box to work properly, but for the sake of this numerical evaluation, this should hold, given that the output of the STB method is simulated with an artificial tracer generator.

Generally speaking, the quality of reconstruction is good for low r^*, which means higher seeding concentration, and eventually worsens for higher interparticle distances. A method that decays in resolution u^* at the latest possible r^* is desired because it means that it is able to spatially reconstruct the velocity field even when the seeding information is lower. The results of the analysis are shown in Chapter 5.2.

5.2 Results

5.2.1 Amplitude modulation

This chapter presents the performances of VIC-TSA (Scarano et al. [2022]), space-super resolution with time-segment assimilation, against VIC+ (Schneiders and Scarano [2016]), space-super resolution with material derivative assimilation. The influence of the radial basis functions is investigated. Subsequently, other metrics for mesh convergence and robustness to noise will be presented.

Figure 5.9 shows the amplitude modulation u^* vs. the interparticle distance r^* for different methods. Each method with a specific setting is referred to by a certain color and line style consistently throughout the plots. The solid line indicates RBF on, and dashed is RBF off.

- Figure 5.9a: Amplitude Modulation (LI, VIC+ rbf on/off)
  This figure compares the amplitude modulation of the Linear Interpolation (LI) method against the VIC+ methods with and without RBF. The solid black curve represents the moving average and serves as a baseline for comparison, representative of the cross-correlation analysis in classic PIV. This should be the worst, because it averages different particles while all the others, also LI, interpolate on the single particles directly. The presence of RBF (cyan solid curve) seems to improve the response to the amplitude modulation, as indicated by the curve being higher than the moving average baseline and VIC+ RBF off, suggesting that RBF enhance the fidelity of the VIC+ method. The dashed cyan curve, representing VIC+ without RBF, shows a less performing response but still superior to LI. We see that the moving average is indeed the worst because it crosses the $u^* = 0.5$ line, (which is

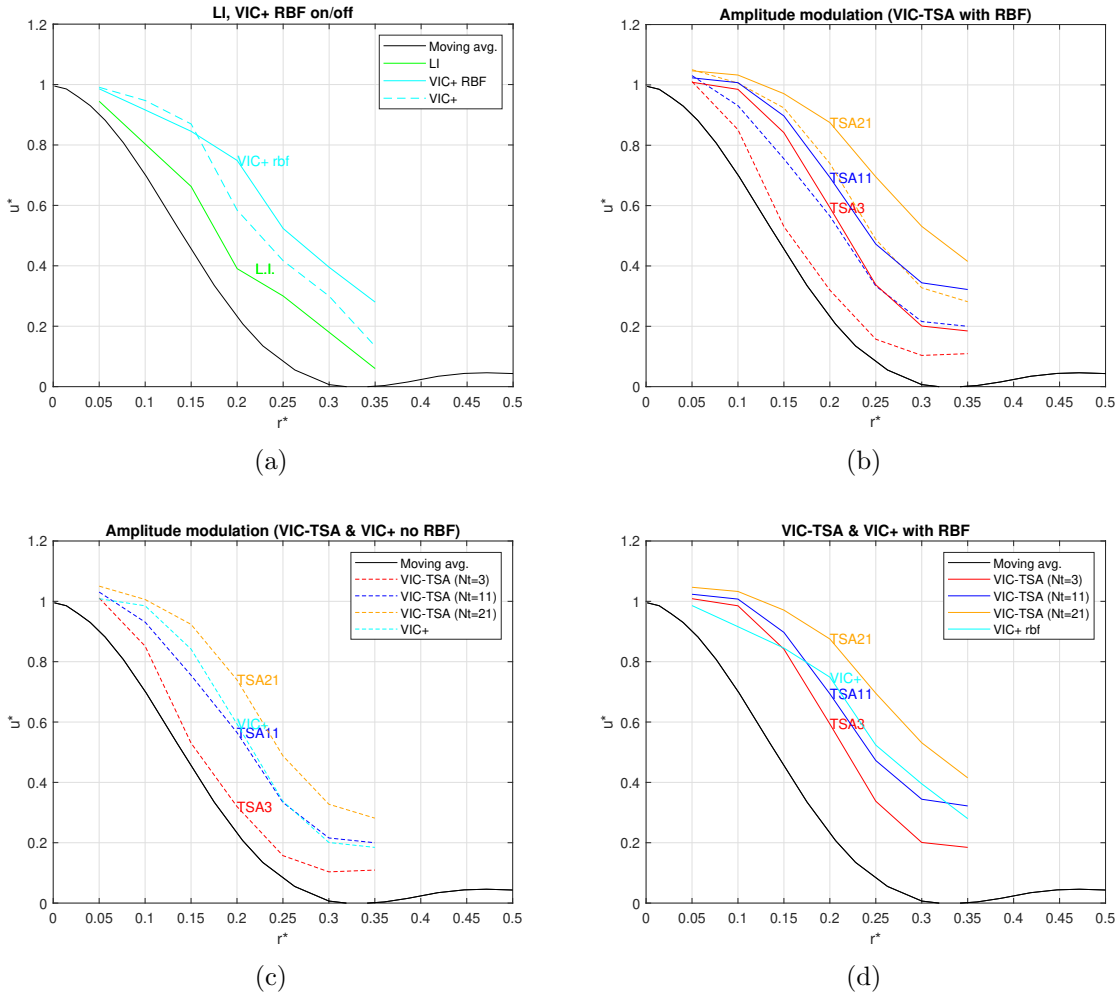

Figure 5.9: Amplitude modulation.

the -3 dB line), at around $r^* = 0.13$. VIC+ without RBF does it at 0.22 and the RBF improves it to 0.27.

- Figure 5.9b: Amplitude Modulation (VIC-TSA with RBF)
  This figure presents the amplitude modulation of VIC-TSA for various time segments with the inclusion of RBF. We see that the RBFs have a similar effect as on VIC+, particularly at NT = 3 and NT = 21.

- Figure 5.9c: Amplitude Modulation (VIC-TSA & VIC+ no RBF)
  Here is it shown the comparison of the VIC-TSA method for different time segments against VIC+ without RBF. The TSA method generally improves the response over the VIC+ method without RBF. The performance gain is more pronounced with

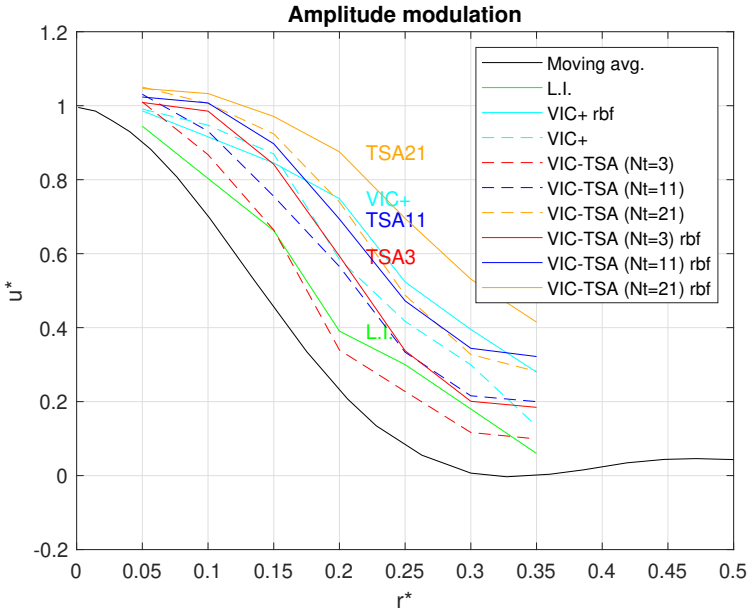

Figure 5.10: Amplitude modulation, global comparison.

longer time segments, and the situation is very similar to Scarano et al. [2022], with $N_t = 11$ being slighlty better than VIC+ and $N_t = 21$ considerably better. The latter would be representative of the stringy regime, which in theory should be beyond the optimum $\tau* = 1$, but it has to be said that for steady test cases, increase in temporal information yields additional spatial information.When considering VIC-TSA with $N_T = 3$, it appears to be inferior to VIC+. This suggests that the material derivative may be a more effective approach compared to using a few assimilated snapshots with TSA in the adjacent tracks regime.

- Figure 5.9d: Amplitude Modulation (VIC-TSA & VIC+ with RBF)
  This is similar to the previous figure, but it includes the use of RBF. The general trend remains consistent, but the inclusion of RBFs has greatly improved the TSA method. For example, in the confidence region where the u^* curve intersects the $u^* = 0.9$ line, TSA21 RBF extends the crossing point to the right up to $r^* = 0.22$. If compared to LI, which crosses at $r^* = 0.1$, this would in theory indicate that an experiment can be conducted with only half of the resolution requirements.

Figure 5.10 summarizes all the different cases. The TSA method demonstrated an improved capacity to capture amplitude modulation, particularly as the time segment length increases, which suggests better spatial resolution or reduced error in flow reconstruction.

5.2.2 On the importance of t^* and track regimes

The performance of the VIC-TSA reconstruction method is visualized in Figure 5.11 for the Taylor-Green vortex lattice using synthetic tracer data. The multiplot arrangement presents r^* increasing from left to right, and the number of assimilated timesteps N_t, extending downward.

The increase in r^* demonstrates a progressive refinement in reconstruction accuracy, as observed by the enhanced clarity and definition in the contour plots from left (lower r^*) to right (higher r^*). Similarly, an upward trend in reconstruction precision is visible as N_t grows, evident from the top (lower N_t) to the bottom (higher N_t) of the figure.

Subsequently, the implementation of Radial Basis Functions (RBFs) within the VIC-TSA algorithm has shown to further improve the details and sharpness of the reconstructed fields (Figure 5.12). Each corresponding plot within the RBF-enhanced reconstruction exhibits augmented fidelity and richer spatial features, affirming the beneficial impact of RBFs on the VIC-TSA method's capability to accurately capture complex flow structures.

One thing that has to be taken into account is the relation between how the nondimensional time t^* relates to the track regimes, which defines the effectiveness of the method, and to the spatial parameters. One thing in particular that should be kept in mind is that $t^*(\mathcal{T}, \overline{r})$ is a function of two variables, that constantly change during the $u^* - r^*$ sweep. The nondimensional time used in this work is compared to the one by Scarano et al. [2022] in Table 5.4. It can be seen that the values of t^* change depending on the interparticle distance r^* and the length of the time segment. Even for the longest time segment, at $N_t = 21$ or 31, the stringy regime ($t^* > 1$) is not always guaranteed at all the $\overline{r}$. At the same time, even $N_t = 3$ can reach values of 1 for a very high seeding concentration (low r^*), even if this is not representative of a real situation experiment. So, one must not confuse the three N_t configurations with the *impulsive, adjacent* and *stringy* track regime, but for sure they guarantee that the governing equations will be satisfied for a longer period of time. This means that the method is still working but not necessarily at its optimum.
In order to be very accurate, one would need to add a third axis to the $u^* - r^*$ plot, with

	$\overline{r} = r^*$		
N_t	0.35	0.2	0.05
3	0.086	0.15	0.6
11	0.31	0.55	2.2
21	0.6	1.05	4.2

Table 5.2: t^* values obtained in this work.

	$\overline{r}$		
N_t	0.4	0.25	0.15
3	0.05	0.08	0.13
11	0.26	0.41	0.67
31	0.77	1.22	2.01

Table 5.3: t^* values by Scarano et al. [2022].

Table 5.4: t^* values.

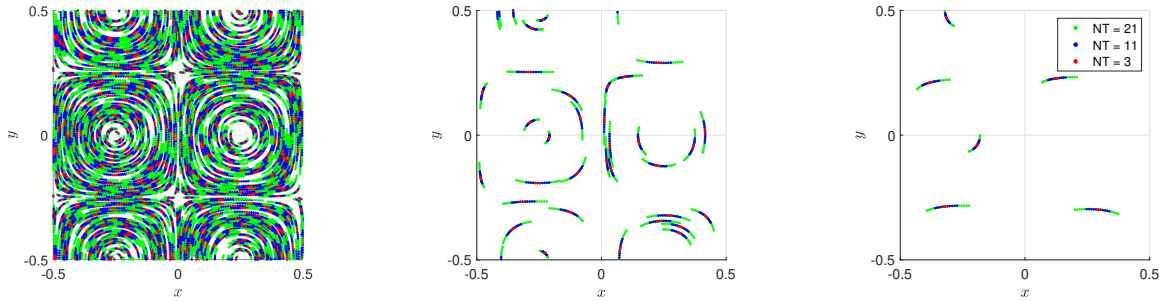

(a) $r^* = 0.05$ (b) $r^* = 0.2$ (c) $r^* = 0.35$

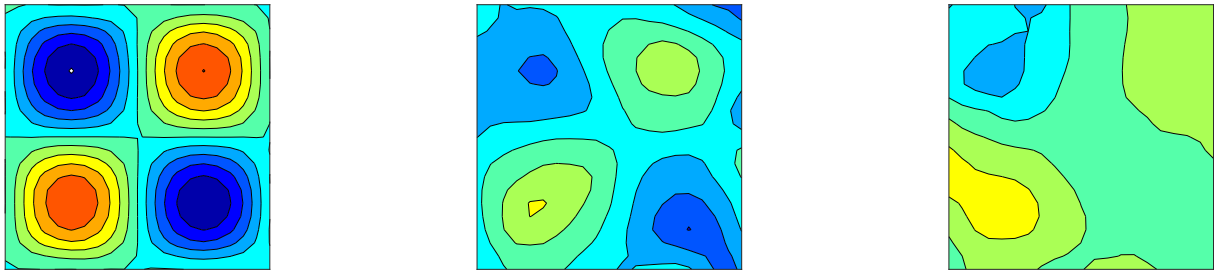

(d) $r^* = 0.05, N_t = 3$ (e) $r^* = 0.2, N_t = 3$ (f) $r^* = 0.35, N_t = 3$

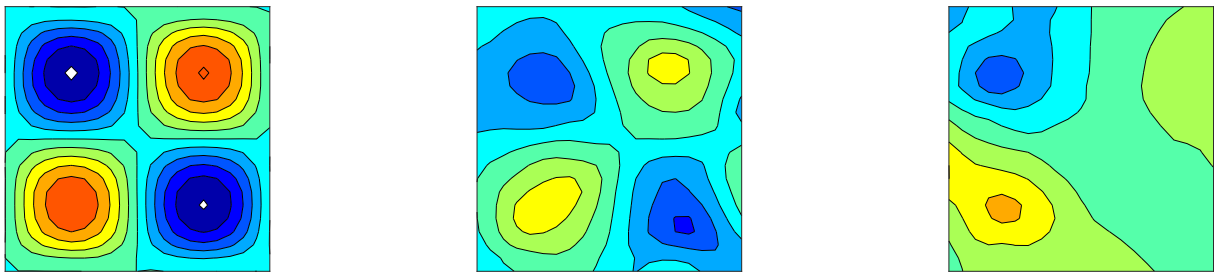

(g) $r^* = 0.05, N_t = 11$ (h) $r^* = 0.2, N_t = 11$ (i) $r^* = 0.35, N_t = 11$

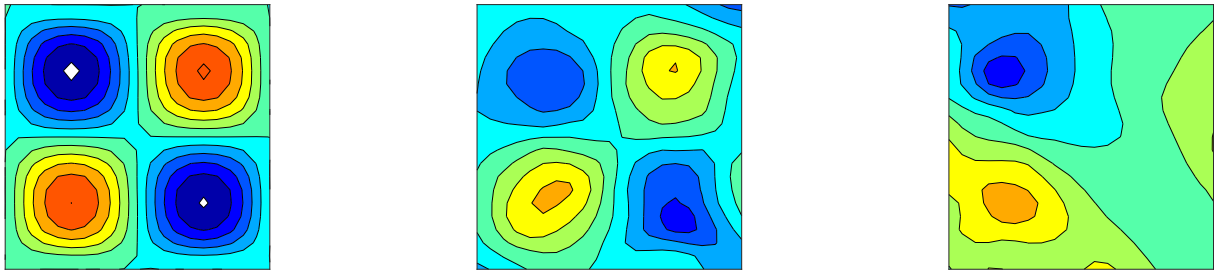

(j) $r^* = 0.05, N_t = 21$ (k) $r^* = 0.2, N_t = 21$ (l) $r^* = 0.35, N_t = 21$

Figure 5.11: $v(x, y)$ velocity component, reconstruction with VIC-TSA without radial basis functions.

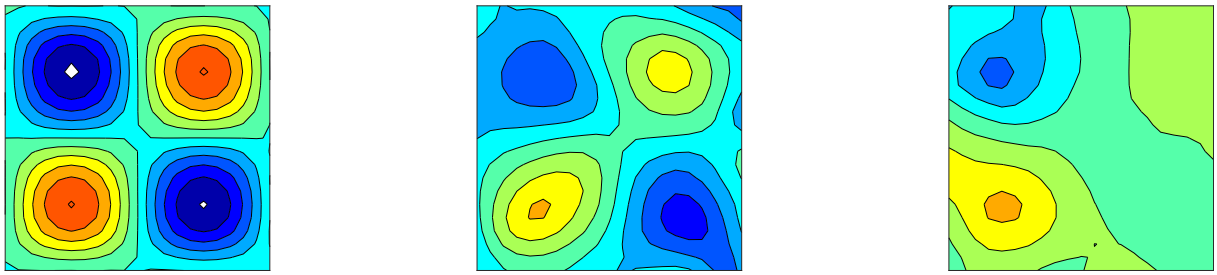

(a) $r^* = 0.05, N_t = 3$ (b) $r^* = 0.2, N_t = 3$ (c) $r^* = 0.35, N_t = 3$

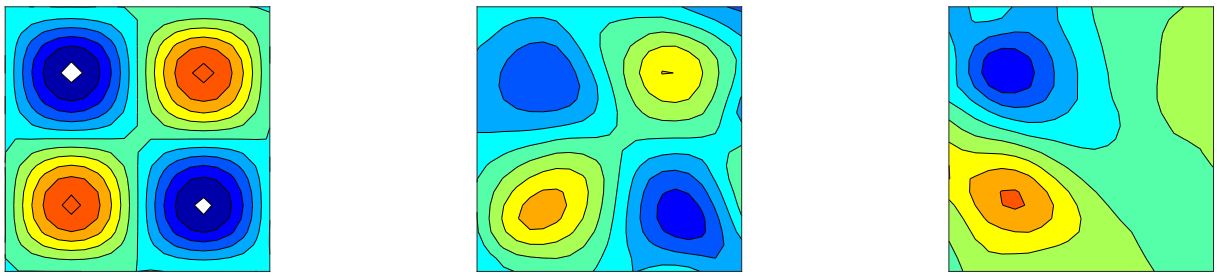

(d) $r^* = 0.05, N_t = 11$ (e) $r^* = 0.2, N_t = 11$ (f) $r^* = 0.35, N_t = 11$

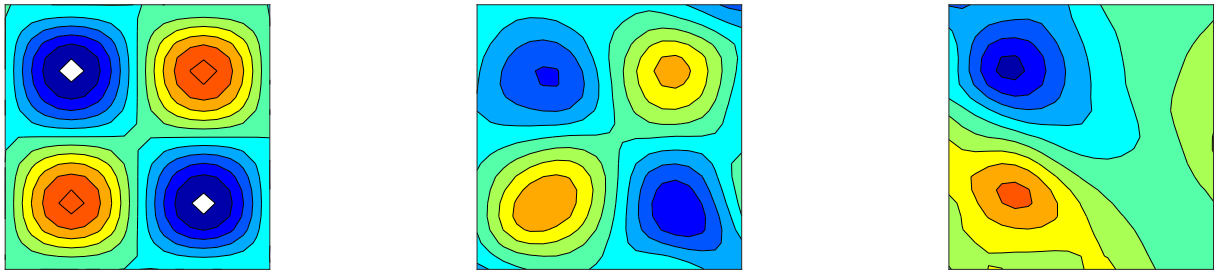

(g) $r^* = 0.05, N_t = 21$ (h) $r^* = 0.2, N_t = 21$ (i) $r^* = 0.35, N_t = 21$

Figure 5.12: $v(x, y)$ velocity component, reconstruction with VIC-TSA with radial basis functions.

the parameter $dt^* = \frac{U \cdot dt}{\bar{r}}$, because this would change the length of the tracks (since we keep the same 3 configurations of N_t). The dependence on λ should not be an issue as long as the parameter r^* is considered. All of this is an overcomplication, considering also that in a real experiment the seeding density is fixed, and the particle tracks can be short and dense, or long and sparse, depending on the local flow velocity. The sampling rate is also fixed. For this reason, a good approach to this numerical evaluation could be to tune dt in a way that produces an optimal adjacent regime around $N_t = 11$ and $r^* = 0.2$. This last value would be a typical and desired situation in PTV[2]; moreover, at high seeding concentration ($r^* \approx 0.05, 0.1$), almost every method performs accurately, while the biggest advantage is

[2]with respect to the flow scales of the specific experiment

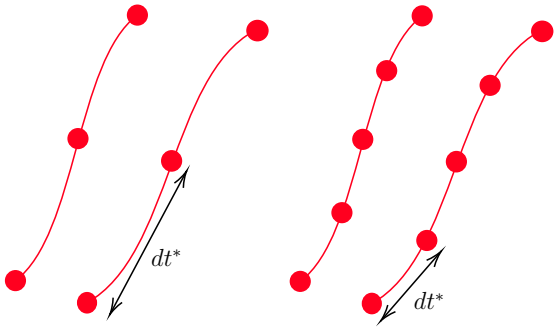

Figure 5.13: Particle tracks characterized by the same t^*, but different dt^*.

around $r^* \approx 0.25$. After this value, the seeding concentration is definitely not enough to perform any quality reconstruction. The three different choices of N_t are introduced to provide a wider range of time variables but also not increased further for computational affordability. However, the parameter t^* is an important indicator of whether the method is working at its optimal condition and an indicator to take into account when balancing accuracy with computational bargain.

5.3 Robustness and convergence

This section presents two additional metrics used to investigate convergence performance and robustness to noise. The analysis compares VIC-TSA with linear interpolation and is articulated as follows.

- **Mesh convergence for interpolations:**
  - *1D interpolation performance:* a comparative analysis of RBF interpolation with other methods using a predefined function $f(r)$.
  - *Taylor-Green interpolation performance:* examination of VIC-TSA against linear interpolation in reconstructing the Taylor-Green flow while varying grid sizes.
- **Robustness analysis:**
  - Investigating the impact of variable Signal-to-Noise Ratio (SNR) on VIC-TSA's performance in reconstructing Taylor-Green flow.

This evaluation is expected to provide a more quantitative understanding of each method's performance and limitations in data interpolation and reconstruction.

5.3.1 Mesh convergence for interpolations

1D interpolation performance. This analysis consists in comparing the interpolation performance of RBf interpolation with linear interpolation and other methods. A function $f(r)$ is chosen as the target for interpolation and is plotted versus r. A certain grid size is chosen, and the function sampled at each data point is interpolated on a more refined grid. The RMSE of the error is computed between the interpolated value and the analytical function $f(r)$:

$$\varepsilon = \frac{\sqrt{\sum_i^{n_{int}} (f_i^{int} - f(r_i))^2}}{n_{int}} \tag{5.14}$$

The RMSE is rooted in the Euclidean distance, or the L2 norm, which measures the straight-line distance between two points in a multidimensional space. In the context of data fitting and interpolation, the L2 norm is a measure of the aggregate distance between the predicted values (interpolated values) and the actual values across all dimensions (data points). The RMSE, as the square root of the average of the squared differences, thus reflects the L2 norm of the error vector.
The study investigates three primary interpolation methods: linear interpolation, spline, and the Radial Basis Functions (RBFs). Each method has distinct attributes: linear interpolation is straightforward and less susceptible to noise; splines create smooth interpolants, and it is commonly used for various applications, including reconstruction methods (FlowFit, Gesemann et al. [2016]). Radial basis functions are highly flexible, and should be versatile and suitable for complex patterns.
The functions investigated are:

1. a sinusoid, which is similar to the Taylor-Green flow;
2. a sawtooth function, to assess the performance in reconstructing sharp gradients;
3. a function that resambles the response to a step function.

Results Figure 5.14 shows the interpolation of different functions with the same number of sample points, with different methods. The comparison of the interpolation error in Figure 5.15 shows that the RBF is generally stable and precise, outperformed by spline for function 3 only, but in this case, the boundary points might play an important role.

Figure 5.16 shows instead the error as a function of the number of sampling points. Generally speaking, RBF seems to be quite good up until it becomes unstable and starts overfittings, which is characterized by a change in slope as can be observed from the Function 1 plot. Nevertheless, this point is way past the level of necessary sample points per wavelength (≈ 100), hence for a realistic number of samples, radial basis functions are a reliable, versatile, and accurate method, especially for sinusoid and oscillating functions like it happens in real flow experiments.

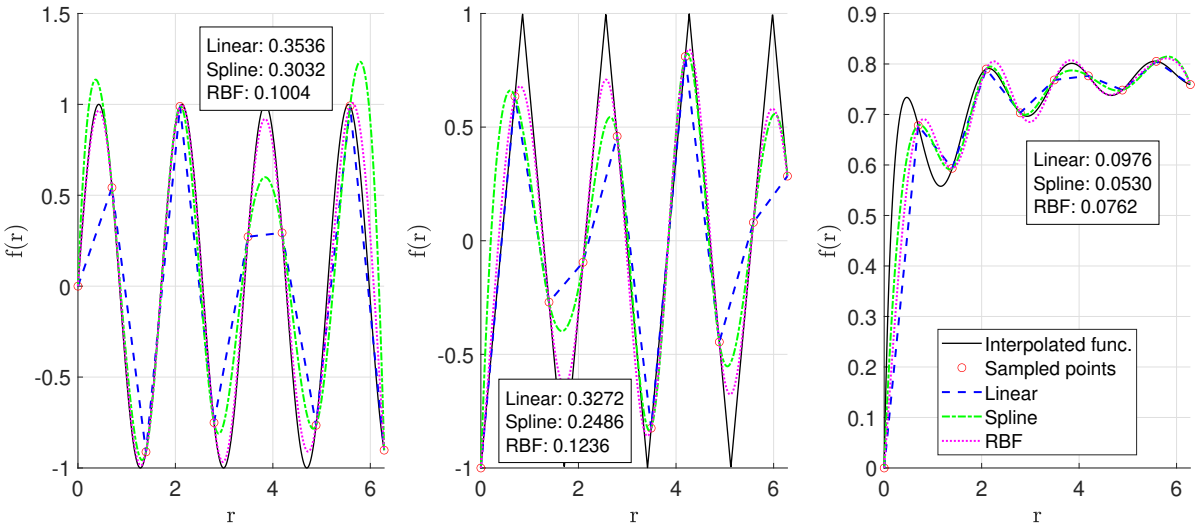

Figure 5.14: Interpolation for different functions with the same number of sample points.

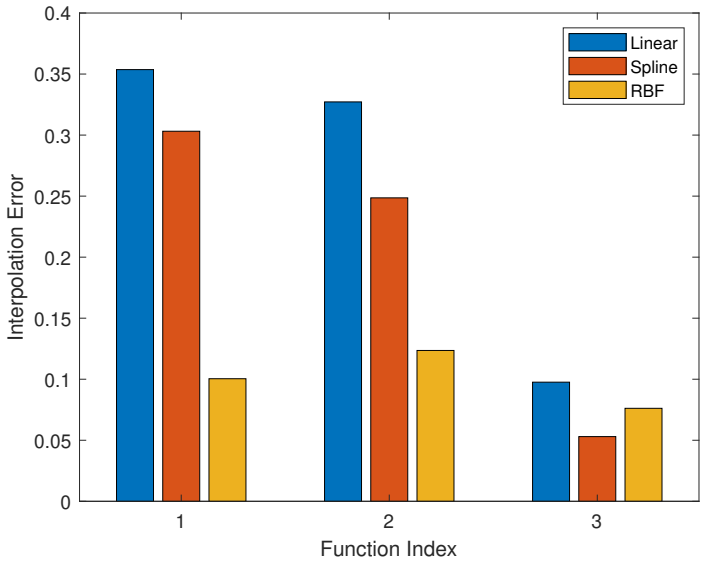

Figure 5.15: Interpolation errors for the different functions.

Taylor-Green interpolation performance This section describes a mesh convergence analysis performed to assess the mesh convergence of the VIC-TSA method on the Taylor-Green test case. It was carried out to verify that the solution is not affected by the grid size and that the error decays when the mesh resolution is increased. It can also be conducted

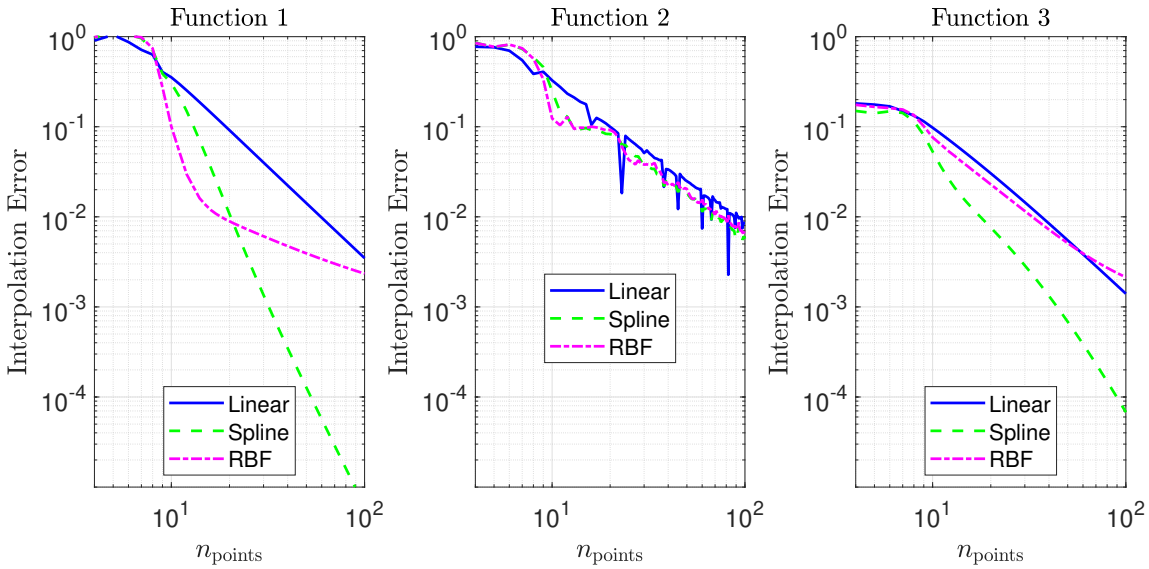

Figure 5.16: Errors for different interpolation methods across the three functions.

to investigate an optimal grid size, to the point that reducing the grid spacing h does not further reduce the error.

To perform the analysis, VIC-TSA was run with the same settings for multiple values of grid spacing. The tracer particles are generated using the method described in 5, and all the parameters of the analysis are provided in Table 5.5. Regarding the choice of optimal h, Schneiders and Scarano [2016] discussed the use of the value $\frac{1}{4}\overline{r}$ for VIC +, which basically allows an increase in space resolution based on tracer concentration. In VIC-TSA, Scarano et al. [2022] shifts the focus to the average distance between particle tracers during a finite time interval, which in theory could still be reduced if $\overline{r} \approx \tilde{r}$, but it is still set to $\frac{1}{4}\overline{r}$ as VIC+. In any case, it might be interesting to note that these values represent an optimal condition in the $u^* - h$ sweep. For this reason, two test cases were set:

- $\overline{r} = 0.05$*:* such a low value of interparticle distance, which means high tracer concentration, is set to eliminate the dependance of the seeding density. For instance, it could happen that if the grid is very fine and the tracer concentration relatively low, the reconstruction in between two particles is so finely discretized that overfitting may occurr;

- $\overline{r} = 0.3$*:* this coarser value of tracer concentration is introduced to observe the effect of reducing the grid size considerably with respect to the tracer concentration. The idea is to induce overfitting to obtain the value of h which does not further reduce the error if it decreases, and to see if the result matches the criterion of Schneiders and Scarano [2016] $\frac{1}{4}\overline{r}$.

$\overline{r}$	N_t	dt	t^*	n.iter.	h
0.05, 0.3	11	0.01	2.2	40	0.02-0.12

Table 5.5: Parameters of the analysis

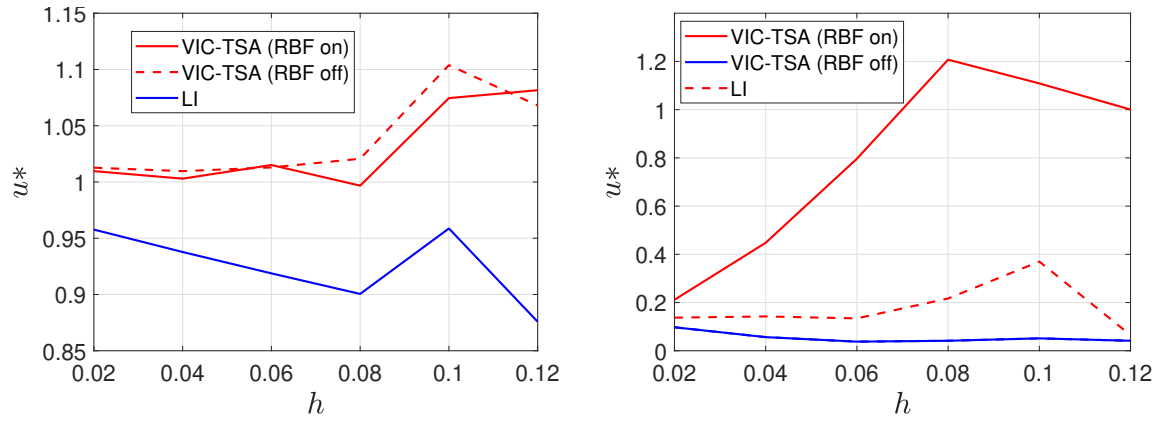

(a) $\overline{r} = 0.05$ (b) $\overline{r} = 0.3$

Figure 5.17: Mesh convergence analysis for VIC-TSA and LI on Taylor-Green flow.

From the results of the analysis (Figure 5.17), it can be seen that:

- $\overline{r} = 0.05$*:* for this dense tracer concentration setting, the amplitude mudulation always converges to 1 if the grid spacing is reduced, as expected. VIC-TSA with RBF on seems to converge slightly faster and modulate less when the grid spacing is coarse, for instance around $h \approx 0.08 - 0.1$. In general, VIC-TSA offers an increase of $0.05 - 0.1$ with respect to LI;

- $\overline{r} = 0.3$*:* this value shows a quite different behavior, since the amplitude modulation does not converge anymore to unity if h is descreased furtherly. This probably happens because if the grid spacing is much smaller than the average interparticle distance, then overfitting might occur. As already explained, Schneiders and Scarano [2016] suggests $\frac{1}{4}\overline{r}$ as an optimal value for the super-resolution factor, and indeed it is also the optimal value in Figure 5.17. If h is further decreased, the method is probably not able to extract enough temporal information to enhance the spatial resolution so much.

5.3.2 Robustness (noise over Taylor-Green)

The particle's velocity in the Taylor-Green flow is subjected to the addition of noise with variable signal-to-noise ratio (SNR), and the reconstruction is carried out using VIC-TSA. This study examines the relationship between the amplitude modulation and the SNR.

An important factor to consider is the comprehension of the power, amplitude, and associated noise properties of the signal. This section provides an explanation of the approach used to compute signal power, introduce noise to the signal, and add it to the data.

Adding noise to the data The signal power is calculated based on the flow field velocity data. Given the oscillatory nature of the velocity components in the flow field, the calculation of signal power involves computing the squared magnitude of the three-dimensional velocity vector for each particle. The velocity components are the Taylor-Green flow (Chapter 5), with $A = 1$ being the amplitude of the oscillatory components, and λ is the wavelength. The squared magnitude of the velocity vector for each particle is calculated as:

$$\texttt{U\_mag\_2} = \texttt{sum}(\texttt{dataSTB(:,4:6)}^2, 2), \tag{5.15}$$

where `dataSTB(:,4:6)` contains the $u(x, y)$, $v(x, y)$, and w - components of the velocity for each particle. The mean of these squared magnitudes gives the signal power:

$$P_{\text{signal}} = \texttt{mean}(\texttt{U\_mag\_2}). \tag{5.16}$$

To assess the robustness of the VIC-TSA algorithm under noisy conditions, artificial noise is added to the velocity data. The noise power is derived from the desired SNR level and the calculated signal power. For a given SNR in decibels, the noise power is:

$$P_{\text{noise}} = \frac{P_{\text{signal}}}{10^{\frac{\text{SNR}}{10}}}. \tag{5.17}$$

The standard deviation of the noise σ_{noise}, representative of its amplitude, is then the square root of the noise power. The noise is generated as a normally distributed random variable with zero mean and standard deviation equal to the square root of the noise power. Then it is added to each velocity component:

$$\texttt{noise} = \sqrt{P_{\text{noise}}} \cdot \texttt{randn}(\texttt{size}(\texttt{dataSTB(:,4:6)})). \tag{5.18}$$

$$\texttt{dataSTB(:,4:6)} = \texttt{dataSTB(:,4:6)} + \text{noise}. \tag{5.19}$$

In this process, the noise amplitude is directly related to the standard deviation of the added noise. This approach allows for a clear understanding of the impact of noise amplitude on the flow field data and the performance of the VIC-TSA algorithm.

Discussion of results The analysis of the VIC-TSA algorithm's performance with added noise, as shown in Figure 5.18, indicates that increasing the number of assimilated time-steps N_t enhances the stability and smoothness of the amplitude modulation, particularly evident at lower SNR levels. This improvement in performance can be attributed to

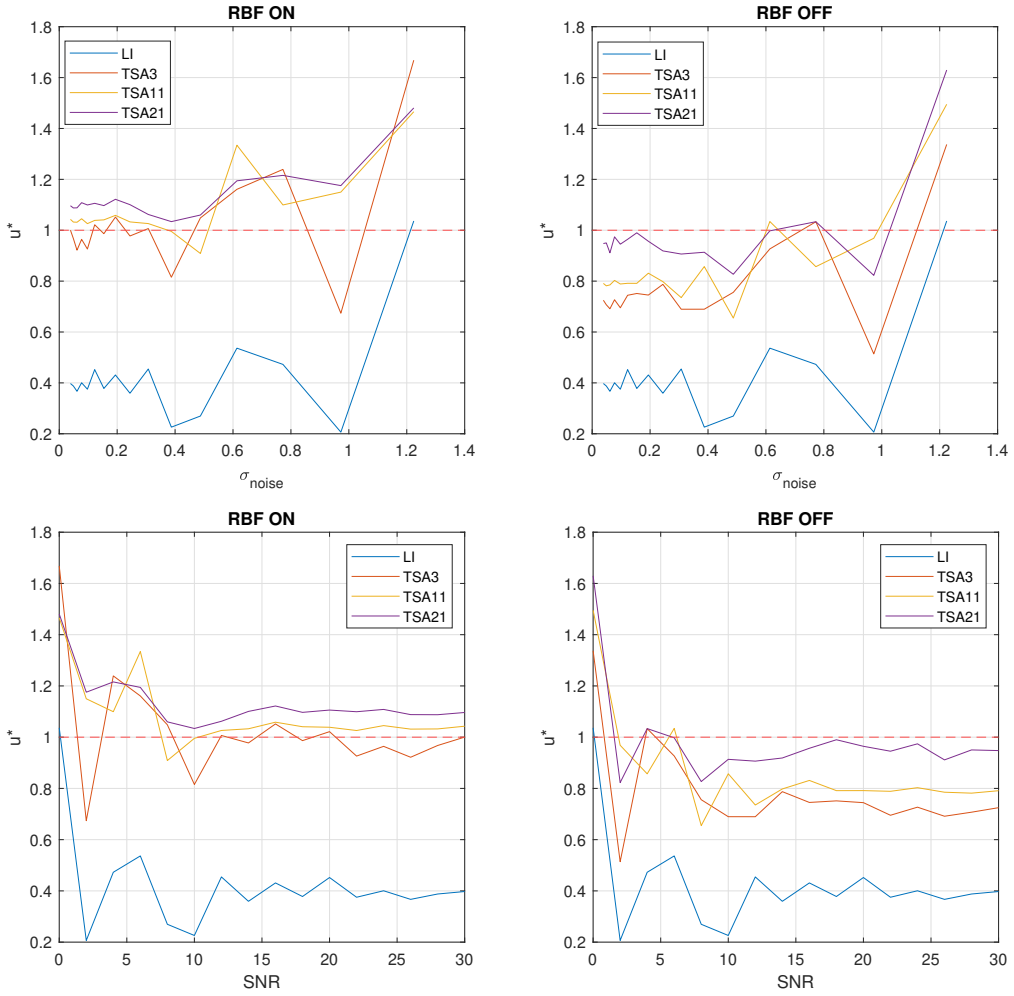

Figure 5.18: Amplitude modulation for flow with added noise reconstructed with VIC-TSA at different N_t and RBF configurations. The results are plotted vs. the SNR and the standard deviation of the noise.

the additional temporal information used in the reconstruction process, which effectively reduces the impact of noise on the estimated flow field. The activation of radial basis functions further refines the reconstruction, consistently yielding amplitude modulation values closer to the expected unity, which corresponds to the true amplitude of the Taylor-Green vortex being reconstructed. Notably, the incorporation of RBFs appears to expedite the convergence of the solution towards the correct amplitude, with a marked stabilization observed even at lower SNR values, which correspond to higher standard deviations of noise. This behavior suggests that RBFs enhance the algorithm's robustness to noise by enforcing a spatial coherence that is resilient to the disruptive effects of random fluctuations inherent to higher noise levels.

Conclusion

This chapter systematically evaluated a reconstruction technique for a synthetic vortex field, specifically the Taylor-Green sine-wave lattice. This model simulates the dynamics of tracer particles in a flow, allowing for the comparison of reconstructed velocities with their theoretical counterparts. The focus is on accurately capturing peak values in the sine waves to gauge the reconstruction's effectiveness.

The chapter begins by addressing the challenges in evaluating reconstruction methods for Particle Image Velocimetry (PIV), given the diversity of approaches and the lack of a standard test case. It underscores the differences between experimental and numerical evaluations and introduces sine-wave reconstructions as a common test scenario. This leads to an in-depth look at the Taylor-Green vortex lattice, which establishes the mathematical basis for simulating the flow and its reconstruction.

The methodology for generating and tracking tracer particles is detailed, including the use of Runge-Kutta methods for time advancement and the derivation of the material derivative. This section emphasizes the mathematical and numerical approaches employed to simulate the movement of particles through the flow field.

Subsequently, the chapter discusses metrics for comparing the reconstruction methods and the process of maintaining consistent tracer density within the domain. It elaborates on the numerical implementation of the flow's governing equations, setting the stage for the reconstruction analysis that follows.

In the evaluation segment, various reconstruction techniques are compared by analizing the modulation of the peak value that they introduce. The discussion incorporates the nondimensional parameters to frame the analysis, comparing moving averages and linear interpolation as baselines. This comparison highlights the strengths and limitations of each method.

The chapter also delves into mesh convergence and robustness analysis. Mesh convergence is explored through the performance of VIC-TSA and linear interpolation in reconstructing the Taylor-Green flow with variable grid sizes, seeking an optimal grid size

that balances accuracy and computational efficiency. The robustness section examines the algorithm's performance under noisy conditions, assessing its stability and accuracy as noise levels vary.

The chapter concludes with a detailed examination of the reconstruction results, focusing on the accuracy of the VIC-TSA method compared to others and the role of radial basis functions in enhancing reconstruction fidelity.

Chapter 6

Experimental assessment

This section describes the experimental assessment for the VIC-TSA method. The purpose of the experiment is to evaluate the performance of the reconstruction method in a real-world scenario, and observe how well it behaves compared to the reconstruction of synthetic data. It consists of the PTV of the flow past a hemisphere with Helium-Filled Soap Bubbles, because:

- it is an easy-to-implement test case;
- it can be used to compare qualitatively how the physics based methods perform versus the PINN (Wang et al. [2022]);
- it contains interesting flow phoenomena to be captured, like hairpin and horshoe vortices and periodic structures.

The effects of radial basis functions and time segment assimilation can be evaluated, as well as the comparison with VIC+ and linear interpolation. A real experiment is considered a good practice because it can reveal strenght and weaknesses of each method. For instance, VIC+ looks very good in simulation, but might struggle in real life since the noise affects more the acceleration data, which is a derived quantity.

The rest of the chapter is organized in this way: first, the experiment is described in detail, including the setup, the parameters, and the data analysis. Then, the limitations of the experiment are discussed. Finally, the results are presented and discussed.

6.1 Experiment description

6.1.1 Objective

In order to evaluate the reconstruction performance of VIC-TSA in a real-world scenario,the flow over a hemisphere was chosen as test case. As already introduced, the choice for this

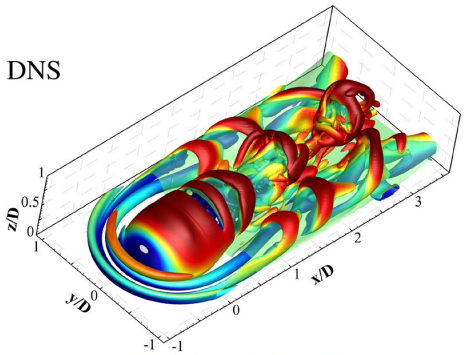

Figure 6.1: DNS data at $Re = 2750$ with iso-surfaces of the Q-criterion colored by the streamwise velocity (Wang et al. [2022]).

test case was made taking into account the experiment carried out by Wang et al. [2022], which was reconstructed with a Physics-Informed Neural Network (PINN). Even though the conditions could not be matched completely due to the difference in the experimental setup, the geometry of the problem still allows for the creation of different flow patterns and vortices, which are interesting and challenging to capture.

An DNS visualization of the flowfield is provided in Figure 6.1, and different features of the flow can be isolated:

- horseshoe vortex near the stagnation point;
- periodic hairpin vortices, created as a result of the sphere obstructing the flow.

6.1.2 Experimental setup for flow over hemisphere

The experimental setup was specifically designed for the Particle Tracking Velocimetry (PTV) of the flow over a hemisphere. This configuration allows for the visualization and analysis of unique flow characteristics around the hemisphere, offering a practical and insightful test case for evaluating the performance of the VIC-TSA reconstruction method.

Wind-tunnel and imaging specifications The experiments were conducted in the W-Tunnel at TU Delft's High-Speed Laboratory, featuring an open-loop, close/open jet configuration with a 40x40cm square exit. The setup facilitates a controlled maximum velocity of 35m/s, with the turbulence intensity kept to a minimum of 0.5%.

Three Photron Fastcam sa1.1 cameras, synchronized with a LaVision High-Speed Controller, were used for image acquisition. These cameras have a resolution of 1024x1024 pixels and a pixel size of 20µm, capable of recording at up to 5400kHz. At the same time, the cameras were arranged to cover the specified field of view: x(-90, 200)mm, y(-220,

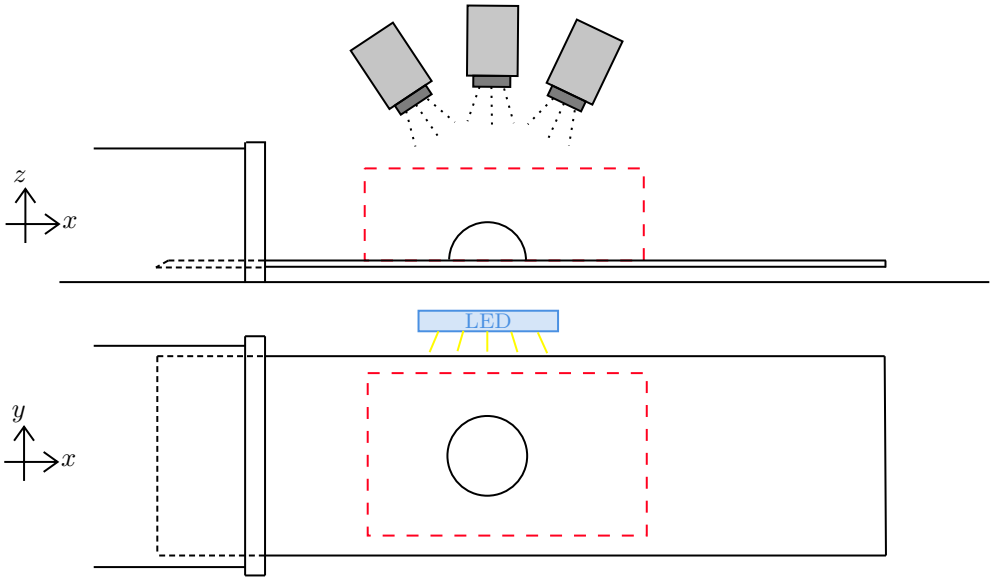

Figure 6.2: Schematic of the experimental setup. Top view (top) and front view (bottom). The measurement volume is in red.

80)mm, z(0, 150)mm. Nikon prime lenses with focal lengths of 60mm and 50mm were used to ensure full coverage of the measurement volume. Two LaVision LED Flashlights were placed on top, which can pulse synchronously with the cameras or continuously. The first option was chosen, since the peak power of the cameras is maximum in pulse mode and provides more illumination.

Hemisphere setup Central to the experiment is a hemisphere with a diameter of 10 cm, mounted on a flat plate and finished in black to minimize reflections. This setup is placed within the wind tunnel, positioned to capture the airflow dynamics around the hemisphere effectively. It is shown in Figure 6.3. Some white markers were drawn on the hemisphere to facilitate the positioning of the sphere in the post-processing phase.

Seeding system and particle tracking The HFSB were generated using a specialized rake system placed in the wind tunnel settling chamber. The pressure levels of the mixture were controlled using a Fluid Supply Unit (FSU), which allowed the production of bubbles with diameters between 300 and 500µm. The expected particle concentration was estimated to be in the range of C = 7.8 to 19.5 particles/cm^3, with the experiment achieving a concentration of approximately C ≈ 3 particles/cm^3.

Calibration and data processing The calibration of the measurement volume was conducted to match the specified field of view. The Shake-The-Box (STB) algorithm was

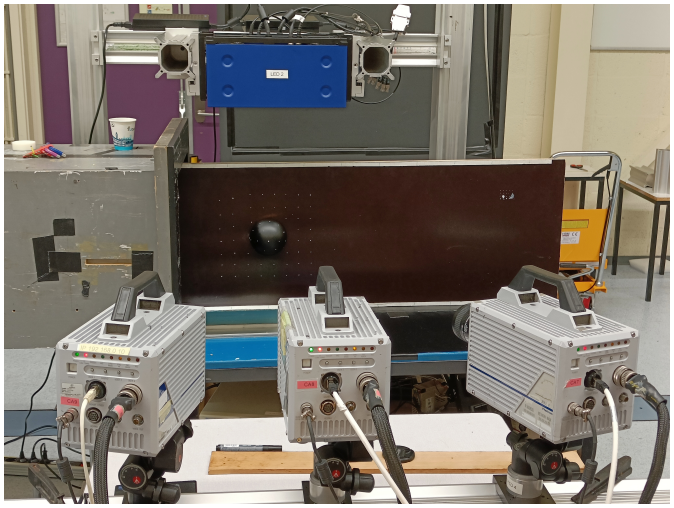

Figure 6.3: Experimental setup. A flat plate with the hemisphere is mounted inside the open section of the wind tunnel.

Object diameter	10 cm
Re	≈ 17000
U_{inf}	2.5 m/s
Domain size (mm)	$(-90, 200)$, $(-220, 80)$, $(0, 150)$
Cameras	3 Photron Fastcam
Sampling frequency	2000 Hz

Table 6.1: Experiment parameters

employed for Lagrangian Particle Tracking, providing accurate tracking of the flow characteristics around the hemisphere and in the wake. This setup facilitated a comprehensive analysis of the flow patterns and vortices generated by the hemisphere, offering valuable insights for the evaluation of VIC-TSA.

Acquisition of the data The acquisition of the measurements were carried out while setting the wind-tunnel at its lowest speed, $U_{fs} = 2.5$ m/s. This corresponds to a Reynolds number of $Re \approx 17000$, which is higher than the one of the experiment conducted by Wang et al. [2022], but it is the minimum reachable with the available setup. This will be further discussed in Section 6.1.4. A total set of 50 images was acquired, with a time interval of 0.5 milliseconds between each image. The total acquisition time was 25 milliseconds, which was enough to capture the vortex structures and their convection.

6.1.3 Data Analysis

Pre-processing and STB DaVis software for PIV was used to preprocess the images. This preprocessing included noise reduction, high-pass filtering of the data, time averaging, and subtracting the average, among other steps.

After the pre-processing, the raw image data of the three camera was processed with Shake-The-Box (STB), which is embedded in DaVis. An important parameter of the processing is the minimum intensity count for detecting a particle. For the current experiment, it was set to 20 counts and 40 counts for the two test cases.

Data sorting and visualization After STB processing, the data are outputted in a text file with Tecplot formatting. In order to match the requirement of the VIC-TSA format described in Table 5.1, Matlab was used to sort the data. Subsequently, the file can be saved as normal experimental data with `.mat` extension, which will be used to obtain the particle data at specific time frames by the VIC+ or VIC-TSA algorithm.

For flow visualization, streamlines are used in conjunction with velocity slices. The isosurfaces of the $\lambda - 2$ criterion, colored by streamwise velocity u, were plotted for the vortex structures. A specific code for calculating the $\lambda - 2$ criterion was developed.

6.1.4 Limitations

Flow regime For sake of comparison, the hemisphere experiment conducted by Wang et al. [2022] to assess the performance of the PINNs (**??**) was at $Re \approx 2750$ (Section 2.4). Such a value indicates that the flow is in the transitional regime, so it will present unsteady structures that are still coherent and recognizable, but not fully laminar. To achieve such low Reynold numbers, the authors conducted the experiment in water. This was of course not feasible in the TU Delft W-Tunnel, and the lowest possible Reynolds number obtainable was ≈ 17000, with the lowest wind-tunnel setting at $U_{WT} = 2.6$ m/s. At this value of Re, turbulence starts playing a role, coherent structures are more difficult to visualize and the horshshoe vortex becomes even smaller.

FOV Moreover, the field of view obtainable with three cameras was not very long, whilst the vortex structures get more stable when they are convected a bit aft from the sphere. Also, for STB to work properly, it is important that each particle is captured by each camera. For this reason, a big open view of the cameras on the flowfield was chosen. Nevertheless, it couldn't be avoided for some of the tracers, especially near the stagnation region, are not perfectly seen by all the three cameras at the same time. This reduces the amount of information that can be used by the reconstruction algorithms slightly.

Nevertheless, considering that the goal of the experiment is not to compare the same exact experiment of the PINN but mainly to provide a simple and effective experimental case to VIC-TSA, it is still acceptable.

Illumination conditions The sphere acts like an obstruction and the particles underneath get a bit shadowed. Also, the reflection in one point causes a bit of ghost particles, but STB is effective at handling these.

6.2 Results

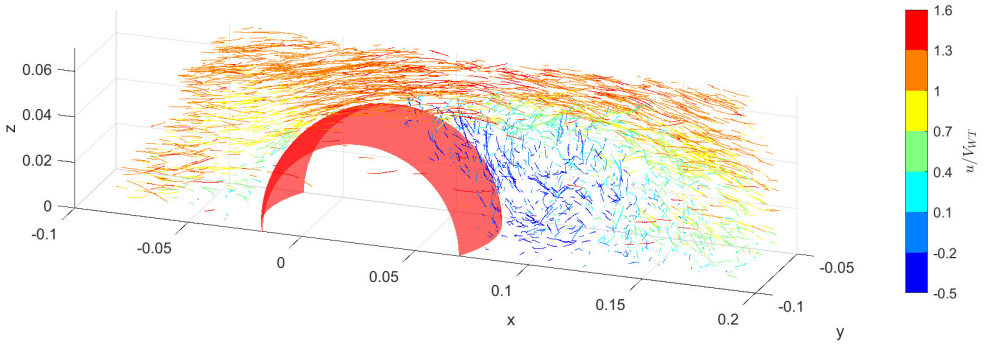

Figure 6.4: Shake-The-Box tracks colored by velocity magnitude.

6.2.1 Streamlines

The visualization provided in Figure 6.6 shows the streamline patterns for the side and top views of a flow field experiment at a height of 23 mm. The comparison between Linear Interpolation (LI), VIC-TSA, and VIC-TSA with RBF provides insight into the effectiveness of each method in capturing the flow dynamics. The visualization involves streamlines of the flow generated from the same random points for all cases and velocity contours.

Linear interpolation appears to present the flow with more angularity, which could be indicative of a less smoothed representation, potentially capturing rapid changes in flow direction or velocity but at the risk of introducing more noise and sparseness into the visualization. The LI method might also not adequately capture the continuous nature of the streamlines, leading to a less coherent understanding of the flow dynamics.

VIC-TSA shows a smoother representation of the flow, which suggests that this method is more effective in filtering out noise and presenting a coherent flow structure. This could be beneficial to identify the overall trends and patterns in the flow, such as recirculation zones, vortex shedding, and regions of high shear.

The introduction of RBF seems to refine the streamline pattern of the recirculating region, for instance by filtering out the smaller vortex at the rear bottom of the sphere in VIC-TSA without RBF, which is likely an error of the method since is is very close to the

ground and the seeding density is very low there. But it seems that VIC-TSA without RBF is able to capture the doublet-like structures in the wake, even though the end of this looks less physical than the RBF on counterpart.

Although the use of RBFs in VIC-TSA is expected to enhance the reconstruction by providing additional support and potentially stabilizing convergence, it may also introduce some degree of smoothing. This smoothing effect can be beneficial in filtering out non-physical fluctuations and noise, which is evident in the visualization of the 3D $\lambda 2$ criterion (Figure 6.5).

6.2.2 Vortex structures

As a general trend, it is possible to observe large vortex structures that break apart from the top of the hemisphere and move downstream, as shown by the $\lambda 2$ vortex detection cryterion in Figure 6.5. These vortices will later arrange in the classical hairpin structure. Other smaller vortices are also visible, especially in the recirculation region behind the sphere. Some hints of the horseshoe vortex are also visible, especially in the LIC plot, but it is not very clear, probably because it is very small. In addition, it is generally difficult to capture and reconstruct details of the flow near the wall. A second test case was attempted by focusing the three cameras on the horseshoe vortex, but the results were also not satisfactory.

The illumination of the sphere came from the top, which in the coordinate system is the positive y-axis, probably causing some noise on the top part of the sphere because of the strong illumination and presence of several particles. However, this did not influence the flow below the sphere significantly, which actually looked very clean and had less noise than the top part, probably due to VIC-TSA acting as a flow solver and still trying to enforce physical constraints in the less illuminated regions.

Among all the reconstruction methods, VIC-TSA with RBF on is the one that provides more clear vortex structures in the 3D visualization; it is also more stable to noise, especially on the region on top of the sphere. It is not entirely clear if some oversmoothing is happening. VIC-TSA RBF off, instead, showed more details, especially in the recirculation region (Figure 6.6), but it is difficult to assess whether they are real or just noise: they for sure look flow-like, but it is the nature of the physics-based methods to enforce some forms of constraints that could make random structures more flow-like, but in the 3D vortex structures is clear that some of them look rather like noise. Generally, it is a good sign that both the physics-based methods are better than linear interpolation and they do not show the typical discontinuities of the latter, which cause problems for derived quantities. This behavior aligns in some sense with the comparison between VIC+ and VIC-TSA discussed in Section 7, where VIC-TSA might be producing a flow that is coherent for the whole time window, and is indeed more stable to noise, but it could also be more diffusive. VIC+, instead, is more sensitive to noise, but it seems pretty accurate for instantaneous flow fields.

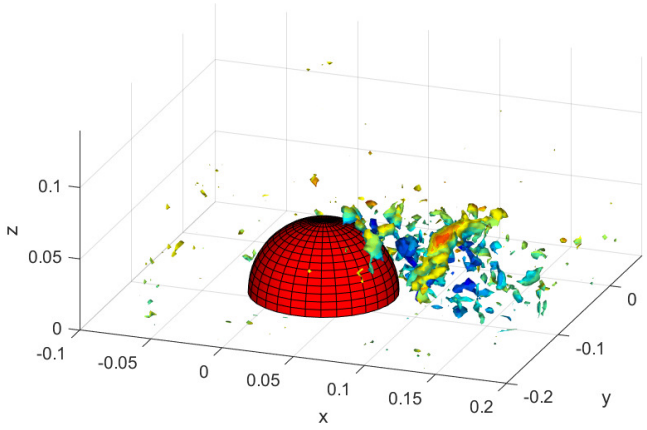

(a) Linear Interpolation

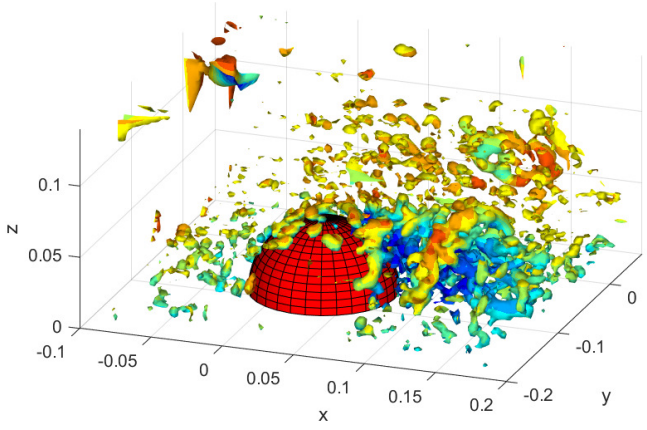

(b) VIC-TSA

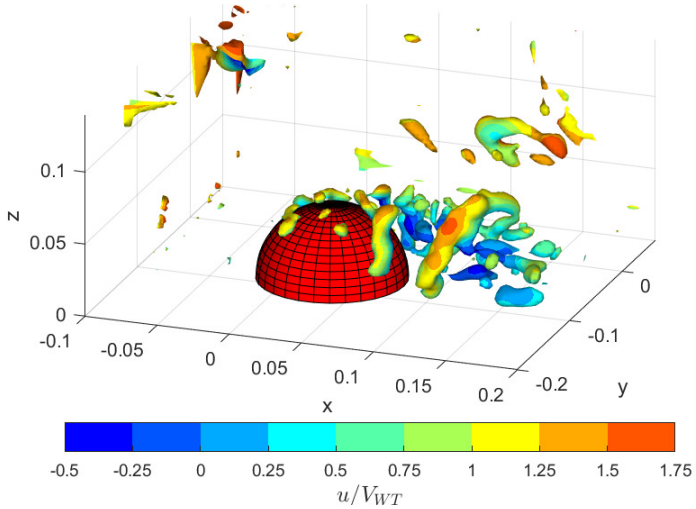

(c) VIC-TSA with RBFs

Figure 6.5: Iso-surfaces of the $\lambda 2$ criterion colored by the streamwise velocity u.

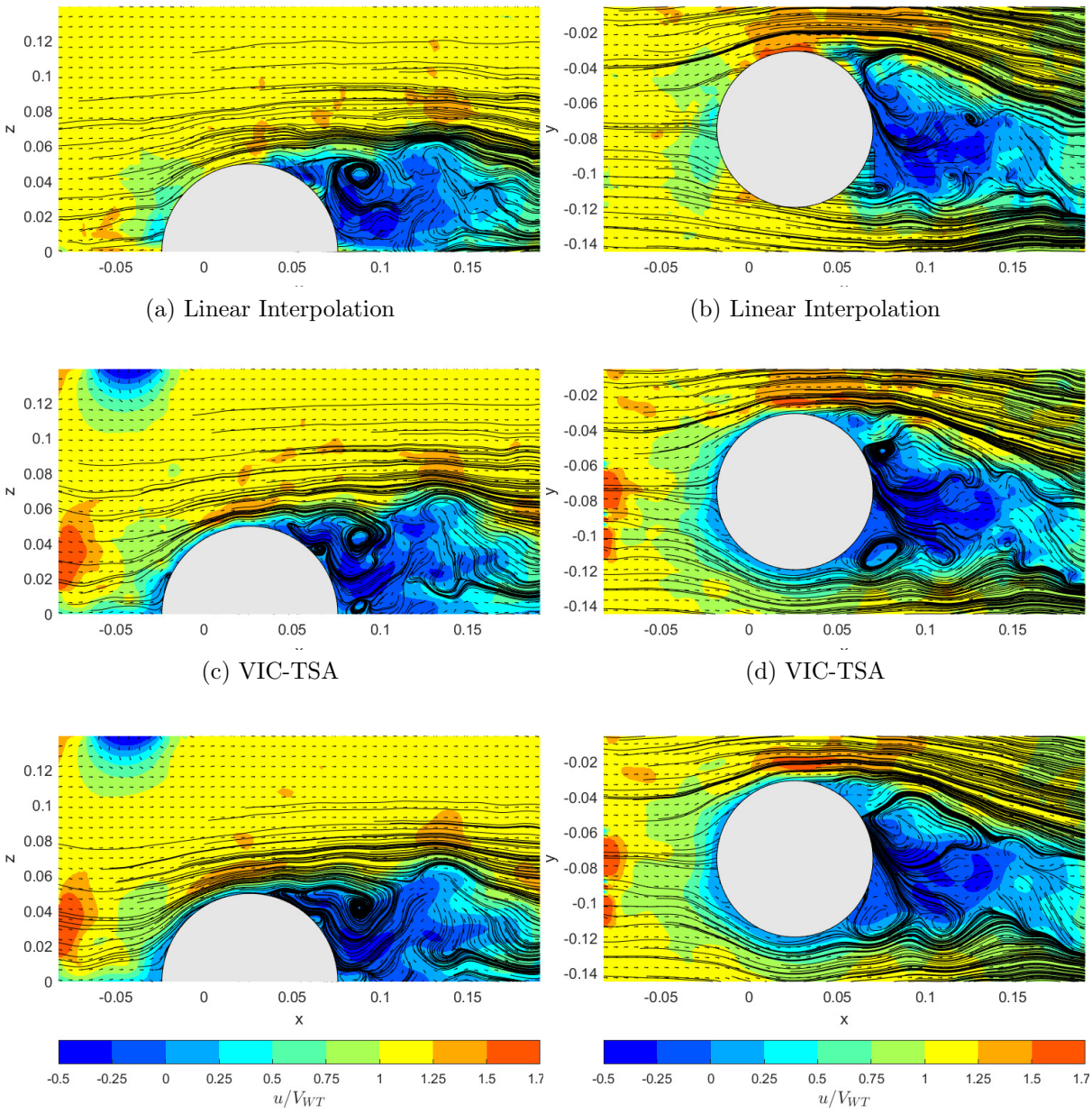

(a) Linear Interpolation

(b) Linear Interpolation

(c) VIC-TSA

(d) VIC-TSA

(e) VIC-TSA with RBFs

(f) VIC-TSA with RBFs

Figure 6.6: Streamlines for side view (left) and top view (right), at a height $z = 23\,\text{mm}$.

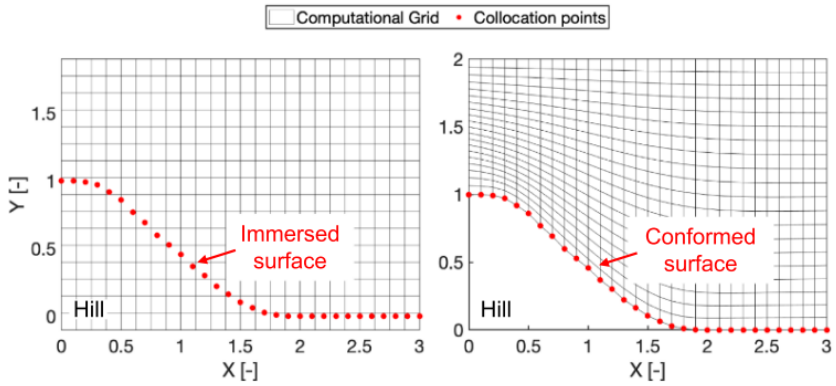

Figure 6.7: Uniform structured mesh with the immersed boundary surface for VIC+ and ImVIC+ (left) and curvilinear boundary fitted mesh on the hill surface for ALE-VIC+ (right), (Cakir et al. [2022]).

6.2.3 Boundary treatment

To deal with the introduction of solid obstructions into the flow, like a hemisphere, artificial particles of zero velocity are added at all time steps to the experimental data in the preprocessing phase. These are generated with a `Matlab` script and positioned to fill the volume of the solid objects, according to their respective positions in the experimental setup. The ground plane is padded 2 cm below the vertical $z-$direction and filled with still particles in this space, to more stabily apply the no-slip condition at a greater distance from the lower numerical boundary.

As described in 2.6, Cakir et al. [2022] investigated the effect of introducing solid objects into the fluid domain, introducing the Arbitrary Lagrangian-Eulerian (ALE) approach for the mesh deformation and the immersed boundary method (ImVIC+). In their numerical assessment, they performed the reconstruction of the flow over a hill with tracer particles sampled from DNS data. A uniform structured mesh (**??**) was used with the immersed boundary surface for VIC+ and ImVIC+ (left) and the mesh fitted to the curvilinear boundary on the hill surface for ALE-VIC+ (right). In a similar scenario like in the present work, the authors had to deal with the fact that the base code for VIC+ is not designed to handle domains with solid walls, so the velocity at the grid points inside the hill was set to zero velocity.

As recently explained, in the present work, particles with zero velocity inside the hemisphere were instead implemented in this work, adding them directly to the experimental data. In its simplicity, the approach has the advantage that the main code remains untouched. Regarding the stability during the optimization with VIC-TSA, while it is true that fixing the values of the grid nodes inside the hemisphere would be more efficient, it is also true that at these grid points the solution will converge rapidly, because of the stable still particles around them.

Figure 6.6 shows the performances of VIC-TSA with and without RBF against the linear interpolator, and it can generally be seen that the still-particle approach for enforcing the hemisphere boundary worked quite smoothly, since there were no evident artifacts near the walls. To some surprise, it was observed how VIC-TSA, regardless of the RBF setting, was able to reconstruct the flow even in zones of the domain without seeding. For instance, by looking at Figure 6.6b, it is visible that linear interpolation is not able to characterize the flow below the hemisphere, and straight parallel streamlines are visible instead, which are clearly unphysical as they also cut throught the sphere. This happens because, as shown in Figure 6.3, the illimunation in the experimental setup came from the top and therefore a cone-shaped shadowed region formed below the hemisphere. Consequently, no particles were captured in this region. Here, VIC-TSA was able to reconstruct the streamlines smoothly, as well as its separation point at $x \approx 0.05$, which was also shadowed. The integration of this area with the remaining flowfield occurs in a seamless manner, as is visible in the coherent streamline pattern in the lower shear layer but also in proximity of the sphere, where the LI showed minor artifacts.

The reconstruction of these regions is possible because VIC-TSA is in essence a Navier-Stokes solver, which will try to fit a field that minimizes the difference with the experimental data and the residuals of the physical equations. This can be thought about as blending PIV and CFD together, in order to get a better representation of the solution in the regions without seeding information. Taking as an example the experiment in Figure 6.6b, one could set the boundary conditions manually in the lower boundary of the domain, in the portion shadowed by the object, to enforce the physical constraint even better. This is because otherwise VIC-TSA will compute such boundary conditions with LI from experimental data, which is missing there. This will also affect the global properties of the flow, since the boundary conditions for the vorticity will influence the computation of the velocity field with the Poisson equation.

Given the interest in the literature in near-wall PIV reconstruction, as well as handing arbitrarily shaped geometries, the approach used in this work with still particles added to the experimental data offers a versatile approach that can work without the need of external tools or user intervention in the code. A more rigorous quantification of the reconstruction accuracy near the wall is out of the scope of this work but could be an object of future work.

Conclusion

In this chapter, an experimental evaluation of the influence of the RBF on the VIC-TSA method was presented, focusing on its application to the flow around a hemisphere. This setup was selected for its straightforward implementation and the opportunity it offers for a qualitative comparison with both traditional methods and the physics-based PINN approach. The experiment aimed to capture a range of flow phenomena, such as hairpin

and horseshoe vortices, which are challenging yet interesting for reconstruction methods.

The setup, parameters, and data analysis of the experiment were described in detail, laying the basis for a comprehensive evaluation of VIC-TSA performance in real-world conditions. Despite facing challenges such as achieving the desired Reynolds number and managing illumination conditions, the experiment served as a valuable test case for examining the method's effectiveness and limitations.

The results section highlighted VIC-TSA's ability to reconstruct coherent vortex structures and its resilience to noise, suggesting a slight trade-off with potential diffusiveness. Compared to linear interpolation, VIC-TSA showed better capability in handling flow structures and reconstructing in areas with scarce data. This performance is attributed to VIC-TSA's foundation on Navier-Stokes equations, enabling it to infer flow dynamics in regions with limited information.

The chapter also delved into the boundary treatment, introducing the approach of using still particles to represent solid objects within the flow. This simple yet effective method allowed for accurate flow reconstruction near solid boundaries without altering the core algorithm. The discussion indicated that while this approach successfully maintains flow integrity near boundaries, it also opens the door for further exploration into accurately quantifying reconstruction accuracy in these areas.

Chapter 7

Conclusion and future work

This thesis has explored the implementation of Radial Basis Functions (RBF) in the Vortex-in-Cell Time-Segment Assimilation (VIC-TSA) framework, aiming to enhance the method's accuracy and performance. The study has provided a comprehensive overview of the VIC-TSA method, its theoretical foundations, and its numerical implementation. It has also detailed the process of integrating RBF into the algorithm, including additional metrics for mesh convergence and robustness to noise. The numerical assessment has evaluated the new implementations, comparing different methods and the effect of RBFs. The experimental assessment has demonstrated the impact of the improvements on a real-case scenario, providing insights into VIC-TSA's performance in reconstructing complex flow phenomena.

Performances and comparative analysis

Regarding the performance of VIC-TSA versus its predecessor VIC+, enhancements due to the inclusion of RBF were clearly visible, resulting in an improved version of VIC-TSA which performs better in terms of amplitude modulation. The level of improvement in VIC-TSA's performance is approximately equivalent to the improvement achieved by activating the RBF in VIC+. However, it is worth noting that at low time assimilation ($N_t = 3$), VIC-TSA does not exhibit significant improvements over VIC+. It might be, following the discussion in Section subsection 5.2.2, that even though the time segment assimilation should in theory be better at assimilating time information (because the equations need to be satisfied over a longer period), VIC+ has the material derivative that in some way improves the minimization problem, similarly to what using the RBF would do, which can be considered a numerical-physical effect; or perhaps for the *instantaneous* flow field reconstruction, the material derivative is more effective than what we think. Perhaps further work could be developed to include the material derivative to create VIC-TSA+, which might give a better view on the problem.

Regarding the discussion about instantaneus versus time segment approach, the follow-

ing can be summarized:

- VIC-TSA assimilates data over a longer time segment, ensuring that the reconstructed flow field at the central snapshot adheres more closely to the governing fluid dynamics equations; this approach might inherently act as a filter, smoothing out short-term fluctuations or noise, leading to a more coherent and less noisy snapshot.
- VIC+ incorporates both velocity and acceleration data of tracer particles, focusing on the immediate state and dynamic changes at a single instant. This method captures transient, short-term dynamics but might include more noise or fluctuations due to less temporal smoothing.

Suggestions for future work

In light of the findings and discussions presented throughout this thesis, some avenues for future research have been identified. These suggestions aim to address some of the limitations observed in the current study and propose potential enhancements for the Vortex-in-Cell Time-Segment Assimilation (VIC-TSA) framework.

1. *Exploration of alternative RBF kernels* The utilization of Gaussian Radial Basis Functions (GRBF) in the VIC-TSA framework has demonstrated certain limitations, particularly in terms of data smoothing. It is proposed that future studies investigate alternative RBF kernels, such as a spikier version of the Gaussian shape that gets steeper towards zero (**??**), which may offer reduced smoothing effects. This exploration could potentially enhance the accuracy of the velocity field reconstructions by preserving more detailed flow features.

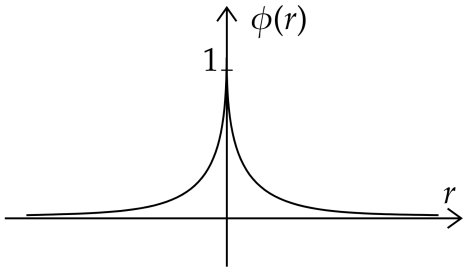

Figure 7.1: Alternative RBF kernel.

2. *Improvement of boundary treatment* The handling of solid boundaries within the flow by the VIC-TSA method requires further refinement. The current approach, utilizing still particles to model solid objects, presents an opportunity for improvement. Future work could explore alternative methods for boundary treatment, assessing their efficacy in accurately capturing the flow dynamics near boundaries and their integration into the VIC-TSA framework as a more effective flow solver.

3. *Adjoint code optimization* The integration of RBFs into the adjoint code, particularly for vorticity calculations, has been identified as an area for optimization. Rewriting the adjoint procedure to more efficiently incorporate RBFs could lead to improvements in computational efficiency and accuracy. This optimization would address the current methodological limitations and align the computational representation more closely with the continuous nature of fluid dynamics.

4. *Inclusion of the material derivative* Despite the theoretical redundancy due to the time segment assimilation approach of VIC-TSA, the incorporation of the material derivative into the framework warrants exploration. This addition could provide a comparative analysis of the dynamics captured by VIC+ versus VIC-TSA, potentially enhancing the ability of VIC-TSA to accurately model transient phenomena.

5. *Methodologies for unsteady flow assessment* Finally, the development of new methodologies or metrics to evaluate the accuracy of the reconstruction of unsteady flows remains a critical need. Such methodologies would facilitate a more robust evaluation of reconstruction methods, particularly in their ability to capture transient flow characteristics, and could significantly contribute to the advancement of flow reconstruction techniques.

These suggestions are proposed as logical extensions of the current work, aimed at further exploring and addressing the complexities of flow reconstruction using the VIC-TSA framework. While the proposed improvements are grounded in the findings of this study, their implementation and impact would require thorough investigation.

Bibliography

Jan F. G. Schneiders and Fulvio Scarano. Dense velocity reconstruction from tomographic ptv with material derivatives. *Experiments in Fluids*, 57(9):139, 2016. ISSN 1432-1114. doi: 10.1007/s00348-016-2225-6. URL https://doi.org/10.1007/s00348-016-2225-6.

Fulvio Scarano, Jan FG Schneiders, Gabriel Gonzalez Saiz, and Andrea Sciacchitano. Dense velocity reconstruction with vic-based time-segment assimilation. *Experiments in Fluids*, 63(6):96, 2022. ISSN 1432-1114. doi: 10.1007/s00348-022-03437-2. URL https://doi.org/10.1007/s00348-022-03437-2.

Hongping Wang, Yi Liu, and Shizhao Wang. Dense velocity reconstruction from particle image velocimetry/particle tracking velocimetry using a physics-informed neural network. *Physics of Fluids*, 34(1), 01 2022. ISSN 1070-6631. doi: 10.1063/5.0078143. URL https://doi.org/10.1063/5.0078143. 017116.

Young Jin Jeon, Markus Müller, and Dirk Michaelis. Fine scale reconstruction (vic#) by implementing additional constraints and coarse-grid approximation into vic+. *Experiments in Fluids*, 63(4):70, 2022. ISSN 1432-1114. doi: 10.1007/s00348-022-03422-9. URL https://doi.org/10.1007/s00348-022-03422-9.

Bora O. Cakir, Gabriel Gonzalez Saiz, Andrea Sciacchitano, and Bas van Oudheusden. Dense interpolations of lpt data in the presence of generic solid objects. *Measurement Science and Technology*, 33(12):124009, 2022. doi: 10.1088/1361-6501/ac8ec7. URL https://doi.org/10.1088/1361-6501/ac8ec7.

Jan F. G. Schneiders, Fulvio Scarano, and Gerrit E. Elsinga. Resolving vorticity and dissipation in a turbulent boundary layer by tomographic ptv and vic+. *Experiments in Fluids*, 58(4):27, 2017. ISSN 1432-1114. doi: 10.1007/s00348-017-2318-x. URL https://doi.org/10.1007/s00348-017-2318-x.

Ralf Giering and Thomas Kaminski. Recipes for adjoint code construction. acm trans. math. software. *ACM Transactions on Mathematical Software*, 24, 08 1999. doi: 10.1145/293686.293695.

Daniel Schanz, Sebastian Gesemann, and Andreas Schröder. Shake-the-box: Lagrangian particle tracking at high particle image densities. *Experiments in Fluids*, 57(5):70, 2016. ISSN 1432-1114. doi: 10.1007/s00348-016-2157-1. URL https://doi.org/10.1007/s00348-016-2157-1.

Jan FG Schneiders, Richard P Dwight, and Fulvio Scarano. Time-supersampling of 3d-piv measurements with vortex-in-cell simulation. *Experiments in Fluids*, 55(3):1692, 2014. ISSN 1432-1114. doi: 10.1007/s00348-014-1692-x. URL https://doi.org/10.1007/s00348-014-1692-x.

Sebastian Gesemann, Florian Huhn, Daniel Schanz, and Andreas Schröder. From noisy particle tracks to velocity, acceleration and pressure fields using b-splines and penalties. 01 2016.

Giuseppe Carlo Alp Caridi. *Development and application of helium-filled soap bubbles: For large-scale PIV experiments in aerodynamics*. PhD dissertation, Delft University of Technology, Delft, 3 2018.

Fulvio Scarano and Peter Moore. An advection-based model to increase the temporal resolution of piv time series. *Experiments in Fluids*, 52(4):919–933, April 2012. ISSN 1432-1114. doi: 10.1007/s00348-011-1158-3. URL https://doi.org/10.1007/s00348-011-1158-3.

Georges-Henri Cottet and Petros D Koumoutsakos. Vortex methods: theory and practice. *Cambridge University Press*, 2000.

I.P Christiansen. Numerical simulation of hydrodynamics by the method of point vortices. *Journal of Computational Physics*, 13(3):363–379, 1973. ISSN 0021-9991. doi: https://doi.org/10.1016/0021-9991(73)90042-9. URL https://www.sciencedirect.com/science/article/pii/0021999173900429.

Gerrit Elsinga, Fulvio Scarano, Bernhard Wieneke, and Bas Oudheusden. Tomographic particle image velocimetry. *Experiments in Fluids*, 41:933–947, 12 2006. doi: 10.1007/s00348-006-0212-z.

BW Van Oudheusden. Piv-based pressure measurement. *Measurement Science and Technology*, 24(3):032001, 2013.

Jan F. G. Schneiders, Stefan Pröbsting, Richard P. Dwight, Bas W. van Oudheusden, and Fulvio Scarano. Pressure estimation from single-snapshot tomographic PIV in a turbulent boundary layer. *Experiments in Fluids*, 57(4):53, 2016. doi: 10.1007/s00348-016-2133-9. URL https://doi.org/10.1007/s00348-016-2133-9.

M. Lombardi, N. Parolini, and A. Quarteroni. Radial basis functions for inter-grid interpolation and mesh motion in fsi problems. *Computer Methods in Applied Mechanics and Engineering*, 256:117–131, 2013. doi: 10.1016/J.CMA.2012.12.019. URL https://consensus.app/papers/basis-functions-interpolation-motion-problems-lombardi/86f556c64a25557ca75d9356ad058ae3/?utm_source=chatgpt.

T. Rendall and C. Allen. Unified fluid–structure interpolation and mesh motion using radial basis functions. *International Journal for Numerical Methods in Engineering*, 2008. doi: 10.1002/NME.2219. URL https://consensus.app/papers/unified-fluidstructure-interpolation-motion-using-rendall/14f8680868b25106988be0c42d2263da/?utm_source=chatgpt.

Shifa Xia, Xiulin Li, F. Xu, Lufei Chen, and Yong Zhang. Visualization method for arbitrary cutting of finite element data based on radial-basis functions. *Inf.*, 10:229, 2019. doi: 10.3390/INFO10070229. URL https://consensus.app/papers/visualization-method-arbitrary-cutting-finite-element-xia/0777d1900ca956718fced519499f5e77/?utm_source=chatgpt.

L. Vrankar, F. Runovc, and G. Turk. The use of the mesh free methods (radial basis functions) in the modeling of radionuclide migration and moving boundary value problems. *Acta Geotechnica Slovenica*, 4:42–53, 2007. URL https://consensus.app/papers/methods-basis-functions-modeling-migration-moving-value-vrankar/51c6a1b07ee158bc8b98cfbbbdab91dd/?utm_source=chatgpt.

C. F. Loeffler, Abraão Lemos Caldas Frossard, and L. Lara. Testing complete and compact radial basis functions for solution of eigenvalue problems using the boundary element method with direct integration. *International Journal for Computational Methods in Engineering Science and Mechanics*, 19:117 – 128, 2018. doi: 10.1080/15502287.2018.1430078. URL https://consensus.app/papers/testing-basis-functions-solution-eigenvalue-problems-loeffler/64d28839d8da5e2e924e111444759623/?utm_source=chatgpt.

Yoshinori Abe and Youji Iiguni. Fast computation of rbf coefficients using fft. *Signal Processing*, 86:3264–3274, 11 2006. doi: 10.1016/j.sigpro.2006.01.012.

Geoffrey Ingram Taylor and Albert Edward Green. Mechanism of the production of small eddies from large ones. *Proceedings of the Royal Society of London. Series A, Mathematical and Physical Sciences*, 158:499–521, 1937. doi: 10.1098/rspa.1937.0036.

C. E. Willert and M. Gharib. Digital particle image velocimetry. *Experiments in Fluids*, 10(4):181–193, 1991. ISSN 1432-1114. doi: 10.1007/BF00190388. URL https://doi.org/10.1007/BF00190388.

F. Scarano and M. L. Riethmuller. Advances in iterative multigrid piv image processing. *Experiments in Fluids*, 29(1):S051–S060, 12 2000. doi: 10.1007/s003480070007. URL https://doi.org/10.1007/s003480070007.

Christian Kähler, Tommaso Astarita, Pavlos Vlachos, Jun Sakakibara, Rainer Hain, Stefano Discetti, Roderick Foy, and Christian Cierpka. Main results of the 4th international piv challenge. *Experiments in Fluids*, 57, 05 2016. doi: 10.1007/s00348-016-2173-1.

Appendix A

Radial Basis Functions use in the code

1. `VICplusplus_main.`

```
% Calculate TFFT
if vic.rbf.userbf == 1
    [vic.rbf.A, vic.rbf.dA_dx, vic.rbf.dA_dy, vic.rbf.dA_dz] =
        RBF_matrices(vic.grids.X{1}, vic.grids.X{2}, vic.grids.X{3}, vic);
    vic.rbf.TFFT = calcTFFT_TSA(vic.rbf.rbfsig, vic.grids.X{1},
                                vic.grids.X{2}, vic.grids.X{3});
end

% Define initial condition
if ~isfield(vic, 'DoF_init')
    if vic.rbf.userbf == 1
        vic.omega_init = xicalc3d(vic.grids.hx,vic.grids.hx,vic.grids.hx,
                                  vic.u_init,20);
        vic.omega_init = reshape(vic.omega_init, [numel(vic.u_init)/3, 3]);
        if vic.rbf.userbfdiff == 1
            vic.DoF_init = vic.rbf.A * vic.omega_init;
        else
            vic.DoF_init = calcRBFcoeff_TSA(vic.rbf.TFFT, vic.omega_init);
        end
    else
        vic.DoF_init = xicalc3d(vic.grids.hx,vic.grids.hx,vic.grids.hx,
                                vic.u_init,20);
    end
end
```

2. `VICplusplusOptFunc(costFunc, DoFs_0).`

```
% MARTINO: from DoF (omegas) to RBFs
if opts.rbf.userbf == 1
    xi_init = calcUfromRBF_TSA(opts.rbf.TFFT, DoF);
    xi_init = reshape(xi_init, size(DoF));
else
    xi_init = DoF;
end
```

3. `VICCICforward(DoFs).`

```
u = velocityCalc(grids.hx, grids.hy, grids.hz, xi, bc, opts);
```

4. `velocityCalc.` (Poisson eq)

```
if opts.rbf.userfbdiff == 1
    dwx_dx = opts.rbf.dA_dx * wx;
    dwy_dx = opts.rbf.dA_dx * wy;
    dwz_dx = opts.rbf.dA_dx * wz;
    ...
    dwz_dz = opts.rbf.dA_dz * wz;
end

% Source term calculation
if nargin == 6
    fu{1} = - (ddy(hy, vort(:,:,:,3)) - ddz(hz, vort(:,:,:,2)));
    ...
    fu{3} = - (ddx(hx, vort(:,:,:,2)) - ddy(hy, vort(:,:,:,1)));
```

Acknowledgments

I would like to express my sincere gratitude to my supervisors, Fulvio and Tercio, for their constant support during all phases of the thesis and for our long inspiring conversations about pouring space into time and time into space.

Then, I would like to thank my friends here at TU Delft for this thesis journey together. You have been sources of inspiration and reflection, like our home-made 'Master Thesis Presentation event' and our jam sessions. Special mention to Andrea for helping me in processing the Shake-the-box tracks and letting me drive the car of his experiment. Honorable mention goes to Maurizio and Jenny.

Finally, I would like to express my gratitude to my family for their warm support and constant faith in me.